

**ICE NUCLEATING PARTICLES IN THE ATMOSPHERE: LABORATORY AND
FILED STUDIES**

by
Jingwei Yun

B.Sc., University of Science and Technology of China, 2016

A THESIS SUBMITTED IN PARTIAL FULFILLMENT OF
THE REQUIREMENTS FOR THE DEGREE OF

DOCTOR OF PHILOSOPHY

in

THE FACULTY OF GRADUATE AND POSTDOCTORAL STUDIES

(Chemistry)

THE UNIVERSITY OF BRITISH COLUMBIA

(Vancouver)

August 2021

© Jingwei Yun, 2021

The following individuals certify that they have read, and recommend to the Faculty of Graduate and Postdoctoral Studies for acceptance, the dissertation entitled:

Ice Nucleating Particles in the Atmosphere: Laboratory and Field Studies

submitted in partial fulfillment of the requirements
by Jingwei Yun for
the degree
of Doctor of Philosophy
in Chemistry

Examining Committee:

Allan Bertram, Chemistry, UBC
Supervisor

Gren Patey, Chemistry, UBC
Supervisory Committee Member

Ed Grant, Chemistry, UBC
University Examiner

Roland Stull, Atmospheric Science, UBC
University Examiner

Additional Supervisory Committee Members:

Keng C. Chou, Chemistry, UBC
Supervisory Committee Member

Pierre Kennepohl, Chemistry, U of Calgary
Supervisory Committee Member

Abstract

Aerosol particles can indirectly affect climate by acting as ice nucleating particles (INPs). Although INPs are only a small subset of atmospheric particles, they can have a significant impact on the hydrological cycle and climate by initiating ice formation in clouds and by modifying the lifetime and optical properties of clouds. Nevertheless, the properties of atmospheric INPs are not yet fully understood.

Two important types of atmospheric INPs are mineral dust and biological particles. This dissertation focuses on these two types of INPs. During atmospheric transport, mineral dust particles can acquire water-soluble coatings, such as coatings containing alkali metal nitrates, inorganic acids, and organic solutes. As a result, the effects of alkali metal nitrates, inorganic acids, polyols, and carboxylic acids on the ice nucleation properties of potassium-rich feldspar (K-feldspar), a type of mineral dust INP in the atmosphere, were examined. In addition, daily INP concentrations at Alert, Nunavut, a ground site in the Canadian High Arctic, were determined for October and November of 2018, and the contribution of mineral dust and biological particles to the total INP population was evaluated for this location and time period.

The results in this dissertation improve our understanding of the properties of mineral dust INPs under atmospheric conditions, as well as the concentration, composition, and source of INPs in the Arctic. This information should be useful for global and regional climate models.

Lay Summary

Ice nucleating particles (INPs) are aerosol particles that initiate ice formation in clouds. Although INPs are a small group of atmospheric particles, they can greatly affect the optical properties and lifetime of clouds by changing the amounts of ice in clouds, thus impacting the radiative budget of the Earth and hydrological cycle. The two most important types of atmospheric INPs are mineral dust and biological particles. In this dissertation, we investigated the ice nucleation properties of potassium-rich feldspar, a type of mineral dust, under atmospherically relevant conditions. In addition, we studied the concentrations, composition, and sources of INPs at Alert, Nunavut, in the Arctic. These results should lead to improved predictions of atmospheric INP concentrations and climate.

Preface

Chapter 2 is a co-authored peer-reviewed journal article. Chapter 3 is an accepted co-authored peer-reviewed journal article. Results from Chapter 4 are prepared for submission to a peer-reviewed journal. My contributions to each chapter are provided below in detail.

Chapter 2 (first author on a published journal article): Jingwei Yun, Nicole Link, Anand Kumar, Andrey Shchukarev, Jon Davidson, Anita Lam, Christopher Walters, Yu Xi, Jean-François Boily, Allan K. Bertram: Surface Composition Dependence on the Ice Nucleating Ability of Potassium-Rich Feldspar, *ACS Earth Space Chem.*, 2020, 4, 6, 873-881, doi:10.1021/acsearthspacechem.0c00077.

For Chapter 2, I formulated research questions and designed research project with my supervisor, prepared the potassium-rich feldspar powder studied, performed most of the ice nucleation experiments and data analysis, prepared the main text for publication with guidance from my supervisor, and prepared all of the figures for publication.

Additional contributions from co-authors are the following: Nicole Link and Jon Davidson performed some of the ice nucleation experiments and data analysis; Dr. Anand Kumar and Dr. Jean-Francois Boily helped improve the manuscript; Anita Lam analyzed mineral composition of the potassium-rich feldspar using X-ray diffraction analysis; Christopher Walters determined the surface area of potassium-rich feldspar powder; Dr. Andrey Shchukarev performed cryogenic X-ray photoelectron spectroscopy.

Chapter 3 (first author on an accepted journal article): Jingwei Yun, Anand Kumar, Nicole Removski, Andrey Shchukarev, Nicole Link, Jean-François Boily, Allan K. Bertram: Effects of

Inorganic Acids and Organic Solutes on the Ice Nucleating Ability and Surface Properties of Potassium-Rich Feldspar, accepted by *ACS Earth Space Chem.*, 2021, doi: 10.1021/acsearthspacechem.1c00034.

For Chapter 3, I formulated research questions and designed research project with my supervisor, performed most of the ice nucleation experiments and data analysis, and prepared the main text for publication with guidance from my supervisor, and prepared all of the figures for publication.

Additional contributions from co-authors: Nicole Removski and Nicole Link performed some of the ice nucleation experiments and data analysis; Dr. Anand Kumar and Dr. Jean-Francois Boily helped improve the manuscript; Dr. Andrey Shchukarev performed cryogenic X-ray photoelectron spectroscopy.

Chapter 4 (first author on an article submitted to a peer-reviewed journal): Jingwei Yun, Erin Evoy, Soleil Worthy, Melody Fraser, Daniel Veber, Andrew Platt, Kevin Rawlings, Sangeeta Sharma, Richard Leitch, Allan K. Bertram: Mineral dust and biological ice nucleating particles in the Canadian High Arctic during the fall of 2018 based on ammonium sulfate and heat assays.

For Chapter 4, I formulated research questions and designed research project with my supervisor, prepared all the equipment needed in the field campaign, performed most of the ice nucleation experiments and data analysis, prepared the main text for publication with guidance from my supervisor, and prepared all of the figures for publication.

Additional contributions from co-authors: Erin Evoy collected aerosol samples at Alert, Nunavut with the help from Melody Fraser, Kevin Rawlings, and Daniel Veber; Soleil Worthy

performed some of the ice nucleation experiments and data analysis; Andrew Platt, Dr. Sangeeta Sharma, and Dr. Richard Leitch facilitated the successful implement of the field campaign.

Table of Contents

Abstract.....	iii
Lay Summary.....	iv
Preface.....	v
Table of Contents	viii
List of Tables	xiii
List of Figures.....	xiv
List of Symbols	xxvi
List of Abbreviations	xxx
Acknowledgements	xxxii
Dedication	xxxiv
Chapter 1. Introduction	1
1.1. Aerosols in the atmosphere	1
1.2. Ice nucleation in the atmosphere.....	3
1.2.1. Mechanism of ice formation in clouds	3
1.2.2. The effect of INPs on earth's climate.....	4
1.2.3 Types of INPs in the atmosphere.....	6
1.3 Description of data from freezing experiments.....	9
1.3.1 Stochastic description.....	9

1.3.2 Singular description	10
1.4. Effects of solutes on the freezing of cloud droplets	11
1.5. Motivation for laboratory and field studies of INPs	13
1.6. Overview of Dissertation	14
Chapter 2: Surface composition dependence on the ice nucleating ability of potassium-rich feldspar.....	16
2.1 Introduction	16
2.2 Experimental	18
2.2.1 Chemicals	18
2.2.2 Droplet freezing technique	19
2.2.3 Freezing point depression correction.....	21
2.2.4 Cryogenic X-ray photoelectron spectroscopy (cryo-XPS).....	21
2.3 Results and Discussion.....	22
2.3.1 Ice nucleating ability of K-rich feldspar in pure water.....	22
2.3.2 Ice nucleating ability of K-rich feldspar in alkali metal nitrate solutions	25
2.3.3 Comparison with previous studies that investigated the effects of K ⁺ and Na ⁺ on the ice nucleating ability of K-rich feldspar.	26
2.3.4 The relative abundance of atoms at K-rich feldspar surfaces before and after the exposure to alkali nitrate solutions	33
2.3.5 The effect of K ⁺ on the ice nucleating ability of K-rich feldspar.....	36

2.3.6 Relation between ΔT_{50} and the atomic ratio K/Al.....	37
2.3.7 Relation between ΔT_{50} and cation charge density.....	39
2.4 Conclusions and outlook.....	41
Chapter 3: Effects of inorganic acids and organic solutes on the ice nucleating ability and surface properties of potassium-rich feldspar.....	43
3.1 Introduction.....	43
3.2 Experimental.....	48
3.2.1 Chemicals.....	48
3.2.2 Droplet freezing technique.....	49
3.2.3 Cryo-XPS measurements of K-rich feldspar surfaces exposed to HCl solutions.....	51
3.3 Results and Discussion.....	51
3.3.1 The effects of inorganic acids at low concentrations on the immersion freezing of K-rich feldspar.....	51
3.3.2 Surface composition of K-rich feldspar before and after exposure to HCl and its relationship to ΔT_{50}	59
3.3.3 The effects of organic solutes on the immersion freezing by K-rich feldspar at low concentrations.....	63
3.4 Summary and conclusion.....	72
Chapter 4: Mineral dust and biological ice nucleating particles in the Canadian High Arctic during the fall of 2018 based on ammonium sulfate and heat assays.....	74
4.1 Introduction.....	74

4.2 Experimental Method.....	76
4.2.1 Sampling site and aerosol sampling	76
4.2.2 INP measurements for samples without any treatment	78
4.2.3 Ammonium sulfate assay.....	79
4.2.4 Heat assay	82
4.2.5 Negative controls for the freezing experiments.....	83
4.2.6 Measurements of the concentrations of Al, Na ⁺ , and Cl ⁻	84
4.2.7 Particle dispersion modelling	85
4.3 Results and Discussion.....	86
4.3.1 The concentrations of INPs measured at Alert.....	86
4.3.2 Results from the ammonium sulfate assay	92
4.3.3 Results from the heat assay	94
4.3.4 Correlations between the concentrations of INPs and Al, Na ⁺ , and Cl ⁻	96
4.3.5 Results from particle dispersion modelling.....	98
4.4 Summary and Conclusions.....	101
Chapter 5 Conclusions and Future Work	104
5.1 The effect of solutes on the immersion freezing of mineral dust.....	104
5.2 Investigation on atmospheric INPs in the Arctic	105
5.3 Outlook.....	106
References	109

Appendices.....	139
Appendix A Classical nucleation theory for ice nucleation.....	139
A1 Homogeneous freezing.....	139
A2 Heterogeneous freezing.....	140
Appendix B.....	142
B1 Mixing time of solutes in water droplets.....	142
B2 Calculations of the depth of ion exchange between H_3O^+ and parent K^+ of K-rich feldspar immersed in water using literature data.....	144
Appendix C.....	146
C1 The mixing time of solutes in water droplets.....	147
Appendix D.....	156

List of Tables

Table 3.1: Organic molecules studied and their relevant properties.....	47
Table 4.1: The correlation coefficients and p-values between the concentration of INPs at -16 °C and -22 °C and concentrations of Al, Na ⁺ , and Cl ⁻ . Correlations that are statistically significant (p<0.05) are bolded in red.....	97
Table 4.2: The correlation coefficients and p-values between the concentration of INPs at -16 °C and -22 °C and the residence time of the airmass over different surface types within 0 – 100 m above the surface in the previous 7 days prior to sampling. Correlations that are statistically significant (p<0.05) are bolded in red.....	101
Table B.1: Calculated mixing time (τ_{mix}) of alkali metal cations.	143
Table B.2: Information on the crystal structure of microcline and albite. The information for microcline is obtained from Bailey (1969) and the information for albite is obtained from Prewitt et al. (1976).	143
Table B.3: Calculations of the depth of full exchange of K ⁺ in K-rich feldspar.	144
Table C.1: Structures of the polyols used in the experiments.....	146
Table C.2: Structures of the carboxylic acids used in the experiments.	146
Table C.3: The calculated mixing times (τ_{mix}) of organics and inorganic acids.....	148
Table D.1: Relevant information on the previous measurements of INP concentrations in the Arctic from ground-based or ship-based platforms shown in Fig. 4.4.	156
Table D.2: The residence time that each airmass spent in the 7 days prior to sampling in the footprint layer over a specific surface type (land, sea ice, sea, and snow) for each sample.	157

List of Figures

Figure 1.1: Schematic for direct effect and indirect effect of aerosols on the climate.	2
Figure 1.2: Schematic for different modes of ice nucleation in the atmosphere.	4
Figure 1.3: Schematic for the climatic effect of INPs on mixed-phase clouds and ice clouds. Adapted from DeMott et al. (2010).	6
Figure 1.4: Schematic for the freezing point depression of solutes due to lowering the chemical potential of solutions. The blue line represents the chemical potential of a solid phase (ice in this case) as a function of temperature. The black line represents the chemical potential of a pure liquid phase (pure liquid water in this case) as a function of temperature. The magenta line represents the chemical potential of a solution phase (aqueous solution in this case) as a function of temperature. T_f represents the freezing point of pure water and T'_f represents the freezing point of the aqueous solution.....	12
Figure 2.1: Schematic of the setup for the freezing experiments.	20
Figure 2.2: Freezing data for pure water droplets only containing K-rich feldspar (0.05 wt%), as well as blanks (pure water droplets): (a) fraction frozen of droplets from multiple trials as a function of temperature and (b) ice nucleating active site density (n_s) as a function of temperature. Different symbols but with the same color represent different trials. For panel (b), the black solid line corresponds to the parameterization of n_s values for K-rich feldspar from Atkinson et al. (2013).	24
Figure 2.3 : ΔT_{50} of aqueous droplets containing K-rich feldspar as a function of nitrate concentration. ΔT_{50} represents the difference of T_{50} (temperature where 50% droplets froze) between droplets containing K-rich feldspar and nitrates and droplets containing K-rich feldspar	

with no solutes. The type of nitrate is indicated on the right of the figure. Error bars represent the uncertainty of the temperature measurements (i.e., 0.25 °C) and 95 % confidence intervals based on the Student's t-distribution. The olive dashed line indicates the position where ΔT_{50} is 0. 26

Figure 2.4: ΔT_{50} as a function of concentration of K^+ (panel (a)) and Na^+ (panel (b)) from the current study and a comparison with results reported in the literature. Neither Kumar et al. (2018) nor Perkins et al. (2020) reported median freezing temperatures or ΔT_{50} . The data from Kumar et al. (2018) represents the change in the onset freezing temperatures as a function of concentration of K^+ and Na^+ , since these authors only reported the changes in onset heterogeneous freezing temperatures. The data from Perkins et al. (2020) represents the change in freezing temperatures at an INP concentration of 10^4 per gram of their K-rich feldspar sample. We chose to evaluate the change in freezing temperatures at an INP concentration of 10^4 per gram of their K-rich feldspar sample because their freezing temperatures at this INP concentration for K-rich feldspar suspensions without solutes were similar to our results. The error bars represent the uncertainty of temperature measurements (i.e., 0.25 °C) and 95 % confidence intervals based on the Student's t-distribution. The olive dashed line indicates the position where ΔT_{50} is 0. 28

Figure 2.5: Fraction frozen of droplets containing K-feldspar (0.05 wt %) without solutes and droplets containing K-feldspar (0.05 wt %) with potassium salts. The potassium salts used were KNO_3 (5×10^{-3} M), KCl (5×10^{-3} M), KBr (5×10^{-3} M), and K_2SO_4 (2.5×10^{-3} M). 29

Figure 2.6: Temperature-dependant freezing spectrum of droplets containing K-rich feldspar with and without KNO_3 (5×10^{-3} M). The freezing data for K-rich feldspar in pure water and KNO_3 solutions were obtained by combining the freezing data from six trials (i.e. each freezing spectrum corresponds to 120 droplets). Ice nucleating active site density (n_s) values as a function of

temperature were calculated using Eq. 2.2 from the main text. The error bars correspond to 95 % confidence intervals based on the nucleation statistics from Koop et al. (1997)..... 31

Figure 2.7: Comparison of the freezing spectrum for droplets containing only K-rich feldspar (0.05 wt %) without solutes and droplets containing K-rich feldspar (0.05 wt %) and KNO_3 (5×10^{-2} M). The freezing temperature of the droplets containing K-rich feldspar and KNO_3 has been corrected for freezing point depression using Eq. 2.1 from the main text..... 32

Figure 2.8: Results obtained from cryo-XPS measurements: the atomic ratio Li/Al, Na/Al, K/Al, Rb/Al, Cs/Al and (Li+Na+K+Rb+Cs)/Al for dry powder of K-rich feldspar and K-rich feldspar particles exposed to pure water and alkali nitrate solutions (5×10^{-3} M). The error bars of the atomic ratio are the uncertainty of cryo-XPS measurements (5%) which is obtained from repeating 3 trials for the same experimental conditions. 36

Figure 2.9: ΔT_{50} for alkali cations at the concentration of 5×10^{-3} M as a function of the atomic ratio K/Al at the surfaces of K-rich feldspar particles exposed to alkali nitrate solutions. Two correlations correspond to cases: 1) all the cations included (red dashed line); 2) cations excluding Cs^+ (black solid line). The correlation coefficient R and the p-value for each correlation are indicated in the plot. The error bars for ΔT_{50} represent the uncertainty of temperature measurements (i.e., 0.25 °C) and 95 % confidence intervals based on the Student's t-distribution. The error bars of the atomic ratio are the uncertainty of cryo-XPS measurements (5%) which is obtained from repeating 3 trials for the same condition. 39

Figure 2.10: ΔT_{50} for alkali cations as a function of their cation charge density (i.e., charge density over the surface area of a single cation) at three concentrations studied: (a) 5×10^{-3} M; (b) 5×10^{-4} M; (c) 5×10^{-5} M. The error bars represent the uncertainty of temperature measurements (i.e.,

0.25 °C) and 95 % confidence intervals based on the Student's t-distribution. The correlation coefficient R and p-values are indicated in each panel..... 41

Figure 3.1: Freezing data for the effect of HNO₃ on the ice nucleating ability of K-rich feldspar.

(a) The fraction of frozen droplets containing K-rich feldspar as a function of HNO₃ concentration (0 M, olive; 1×10⁻⁵ M, red; 5×10⁻⁵ M, violet; 5×10⁻⁴ M, magenta; 5×10⁻³ M, orange; 5×10⁻² M, blue). Also included are the fraction frozen of pure water droplets (i.e., blanks) from multiple trials. Different symbols with the same color correspond to different trials. (b) ice nucleating active site density (n_s) as a function of temperature calculated with the freezing data from panel (a). The error bars for n_s correspond to the 95 % confidence intervals calculated with the nucleation statistics from Koop et al. (1997). 53

Figure 3.2: Freezing data for the effect of HCl on the ice nucleating ability of K-rich feldspar. (a)

The fraction of frozen droplets containing K-rich feldspar as a function of HCl concentration (0 M, olive; 1.5×10⁻⁵ M, red; 4.5×10⁻⁵ M, violet; 1.5×10⁻⁴ M, magenta; 1.5×10⁻³ M, orange; 5×10⁻² M, blue). Also included are the fraction frozen of pure water droplets (i.e., blanks) from multiple trials. Different symbols with the same color correspond to different trials. (b) ice nucleating active site density (n_s) as a function of temperature calculated with the freezing data from panel (a). The error bars for n_s correspond to the 95% confidence intervals calculated with the nucleation statistics from Koop et al. (1997). 54

Figure 3.3: ΔT_{50} values as a function of concentration for HNO₃ and HCl solutions, where ΔT_{50}

is the difference of median freezing temperature between the droplets containing K-rich feldspar with and without the inorganic acids. The error bars are the propagation of temperature measurement uncertainty (0.25 °C) and 95 % confidence intervals from 3 trials based on Student's t-distribution. The olive dashed line indicates the position where ΔT_{50} is 0 °C..... 56

Figure 3.4: ΔT_{50} values as a function of pH for HNO₃ and HCl containing droplets, where ΔT_{50} is the difference of median freezing temperature between the droplets containing K-rich feldspar with and without the inorganic acids. The error bars for ΔT_{50} are the propagation of temperature measurement uncertainty (0.25 °C) and 95 % confidence intervals from 3 trials based on Student's t-distribution. The error bars for pH take into account the pH meter uncertainty (0.01 unit) and 95 % confidence intervals from 3 pH measurements based on Student's t-distribution. The black solid line is a fit to the ΔT_{50} values for both HNO₃ and HCl using a Boltzmann sigmoid function. The shaded region is the 95 % prediction band of the fitted line. Also included in the figure are the data from Kumar et al. (2018) where they exposed K-rich feldspar to a NH₄HSO₄ solution (pH = 1.12), and Burkert-Kohn et al. (2017) where they exposed K-rich feldspar to sulfuric acid (pH = -0.1,) and nitric acid (pH = 0), with pH values estimated with the Extended Aerosol Inorganic Model (Clegg et al., 2001). The results from Burkert-Kohn et al. (2017) are upper limits for the ΔT_{50} values since they mainly observed homogeneous nucleation after exposing K-rich feldspar to the strong acids. 58

Figure 3.5: Atomic ratios K/Si, Na/Si, and Al/Si (panel (a)) for K-rich feldspar exposed to pure water or HCl solutions and ΔT_{50} (panel (b)) for K-rich feldspar exposed to HCl and HNO₃ solutions. The pure water case is indicated in the figure. Also included in panel (a) are atomic ratios for a dry powder of K-rich feldspar. The error bars for the atomic ratios are the uncertainty of the cryo-XPS measurements (5%) which corresponds to two standard deviations determined from repeating 3 trials under the same condition..... 61

Figure 3.6: Freezing data for the effect of levoglucosan on the ice nucleating ability of K-rich feldspar. (a) The fraction frozen of droplets containing K-rich feldspar as a function of levoglucosan concentration (0 M, olive; 5.2×10^{-5} M, violet; 1.04×10^{-4} M, magenta; 2.6×10^{-4} M,

orange; 2.6×10^{-3} M, blue). Also included are the fraction frozen of pure water droplets (i.e., blanks) from multiple trials. Different symbols with the same color correspond to different trials. (b) Ice nucleating active site density (n_s) as a function of temperature calculated with the freezing data from panel (a). The error bars for n_s correspond to the 95% confidence intervals calculated with the nucleation statistics from Koop et al. (1997). 64

Figure 3.7: Freezing data for the effect of citric acid on the ice nucleating ability of K-rich feldspar.

(a) The fraction frozen of droplets containing K-rich feldspar as a function of citric acid concentration (0 M, olive; 5.2×10^{-5} M, violet; 1.04×10^{-4} M, magenta; 2.6×10^{-4} M, orange; 2.6×10^{-3} M, blue). Also included are the fraction frozen of pure water droplets (i.e., blanks) from multiple trials. Different symbols with the same color correspond to different trials. (b) Ice nucleating active site density n_s) as a function of temperature calculated with the freezing data from panel (a). The error bars for n_s correspond to the 95% confidence intervals calculated with the nucleation statistics from Koop et al. (1997). 65

Figure 3.8: ΔT_{50} values as a function of concentration for the organic molecules studied, where ΔT_{50} is the difference of median freezing temperature of droplets containing K-rich feldspar with and without the organic molecules. The error bars are the propagation of temperature measurement uncertainty (0.25 °C) and 95 % confidence intervals from 3 trials based on Student's t-distribution. The olive dashed line indicates the position where ΔT_{50} is 0 °C. 67

Figure 3.9: The ΔT_{50} values for carboxylic acids at concentrations of 2.6×10^3 M (panel (a)), 2.6×10^4 M (panel (b)), 1.04×10^4 M (panel (c)), and 5.2×10^5 M (panel (d)). The error bars for ΔT_{50} are the propagation of temperature measurement uncertainty (0.25 °C) and 95 % confidence intervals from 3 trials based on Student's t-distribution. The numbers within the brackets in the x-axis label indicate the number of carboxyl groups in the carboxylic acids. 69

Figure 3.10: ΔT_{50} values as a function of pH for the carboxylic acids. The color indicates the type of carboxylic acid and the symbol type indicates the concentration (see legends). The error bars for ΔT_{50} are the propagation of temperature measurement uncertainty (0.25 °C) and 95 % confidence intervals from 3 trials based on Student's t-distribution. The error bars for pH are the propagation of pH meter uncertainty (0.01 unit) and 95 % confidence intervals from 3 pH measurements based on Student's t-distribution. The black solid line is a fit to the ΔT_{50} values for both HNO₃ and HCl using a Boltzmann sigmoid function. The shaded region is the 95 % prediction band of the fitted line. 71

Figure 4.1: The time series of meteorology data at Alert during the campaign: precipitation (panel (a)), ambient temperature (panel (b)), relative humidity (panel (c)), wind speed (panel (d)), and wind direction (panel e)). The meteorology data were retrieved from the Environment Canada website, <http://climate.weather.gc.ca/>..... 77

Figure 4.2: The effect of ammonium sulfate treatment on the ice nucleating ability of mineral dust. Panel (a): the number of INPs per gram as a function of temperature for ATD without any treatment and with ammonium sulfate treatment. Panel (b): same as panel (a) but for K-rich feldspar. Panel (c): same as panel (a) but for kaolinite. Panel (d): same as panel (a) but for montmorillonite. The data are from Worthy et al. (2021). For each type of mineral dust, different symbols with the same color represent different trials. 81

Figure 4.3: The fraction of frozen droplets as a function of temperature for the blanks (8 trials). Red symbols (5 trials) correspond to extracted solutions from the clean filters using Milli-Q water and blue symbols (3 trials) correspond to 0.05 M (NH₄)₂SO₄ solutions prepared with Milli-Q water. The freezing data for the 0.05 M (NH₄)₂SO₄ trials was corrected for freezing point depression. The

black solid line is the average of the 8 trials and the shading region corresponds to two times the standard deviations of the blanks from the 8 trials. 84

Figure 4.4: The fraction of frozen droplets for the 30 samples collected in the Arctic during October and November. Also included is the average of the blanks and two times the standard deviations of the blanks from the 8 trials. The black solid line is the average of the 8 trials and the shading region corresponds to two times the standard deviations of the blanks from the 8 trials. 87

Figure 4.5: INP concentrations during October and November. Panel (a): The INP concentrations measured as a function of temperature for the daily samples collected in October and November. Panel (b): The monthly average INP concentrations as a function of temperature for the samples collected in October and November. The shading regions in panel (b) represent the 83% confidence bands of the monthly average INP concentrations. Two data sets with normal distributions are statistically different at a confidence interval of 95 % if their 83 % confidence bands of the means do not overlap (Goldstein and Healy, 2009). 89

Figure 4.6: The average INP concentrations as a function of temperature in the Arctic measured in the current study and in previous ground-based or ship-based studies. The sampling platform, location, and time of each study is indicated in Table. D.1 (Appendix D). The error bars for the current study correspond to the 95% confidence intervals of the means. The region shaded in grey shows the literature data from Petters and Wright (2015) for precipitation and cloud water samples. 91

Figure 4.7: The effect of ammonium sulfate treatment on the INP concentrations. Panel (a): The daily INP concentrations measured in October without any treatment and with ammonium sulfate treatment. Panel (b): the monthly average INP concentrations for October without any treatment and with ammonium sulfate treatment. Panel (c): The daily INP concentrations in November

without any treatment and with ammonium sulfate treatment. Panel (d): the monthly average INP concentrations for November without any treatment and with ammonium sulfate treatment. The shading regions in panel (b) and panel (d) indicate 83 % confidence bands. Two data sets with normal distributions are statistically different at a confidence interval of 95 % if their 83 % confidence bands of the means do not overlap (Goldstein and Healy, 2009)..... 93

Figure 4.8: The effect of heat treatment on the INP concentrations. Panel (a): The daily INP concentrations measured in October without any treatment and with heat treatment. Panel (b): the monthly average INP concentrations for October without any treatment and with heat treatment. Panel (c): The daily INP concentrations in November without any treatment and with heat treatment. Panel (d): the monthly average INP concentrations for November without any treatment and with heat treatment. The shading regions in panel (b) and panel (d) indicate 83 % confidence bands. Two data sets with normal distributions are statistically different at a confidence interval of 95 % if their 83 % confidence bands of the means do not overlap (Goldstein and Healy, 2009).95

Figure 4.9: Panel (a): The average footprint PES plots for all the 30 samples collected in October and November. Panel (b): The average footprint PES plots for the samples collected in October. Panel (c): The average footprint PES plots for the samples collected in November. Panel (d): The map showing the surface coverage types on the first day of sampling (Oct-19). Panel (e): The map showing the surface coverage types at the midway point of sampling (Nov-03). Panel (f): The map showing the surface coverage types on the last day of sampling (Nov-17). In each panel, the sampling site is indicated by a red star. The surface coverage data was obtained from National Snow and Ice Data Center..... 99

Figure A.1: Change of free energy during homogeneous freezing a function of the cluster radius, r 140

Figure A.2: Free energy change during homogeneous freezing and heterogeneous freezing as a function of cluster radius, r 141

Figure B.1: Fraction of droplets containing K-feldspar (0.05 wt %) frozen as a function of temperature for 9 different experiments from the same K-feldspar suspension. Each experiment corresponds to the freezing of 20 droplets..... 145

Figure C.1: Freezing data for the effect of glycerol on the ice nucleating ability of K-rich feldspar. (a) The fraction frozen of droplets containing K-rich feldspar as a function of glycerol concentration (0 M, olive; 5.2×10^{-5} M, violet; 1.04×10^{-4} M, magenta; 2.6×10^{-4} M, orange; 2.6×10^{-3} M, blue). Also included are the fraction frozen of pure water droplets (i.e., blanks) from multiple trials. Different symbols with the same color correspond to different trials. (b) Ice nucleating active site density (n_s) as a function of temperature calculated with the freezing data from panel (a). The error bars for n_s correspond to the 95% confidence intervals calculated with the nucleation statistics from Koop et al. (1997)..... 149

Figure C.2: Freezing data for the effect of glucuronic acid on the ice nucleating ability of K-rich feldspar. (a) The fraction frozen of droplets containing K-rich feldspar as a function of glucuronic acid concentration (0 M, olive; 5.2×10^{-5} M, violet; 1.04×10^{-4} M, magenta; 2.6×10^{-4} M, orange; 2.6×10^{-3} M, blue). Also included are the fraction frozen of pure water droplets (i.e., blanks) from multiple trials. Different symbols with the same color correspond to different trials. (b) Ice nucleating active site density (n_s) as a function of temperature calculated with the freezing data from panel (a). The error bars for n_s correspond to the 95% confidence intervals calculated with the nucleation statistics from Koop et al. (1997). 150

Figure C.3: Freezing data for the effect of oxalic acid on the ice nucleating ability of K-rich feldspar. (a) The fraction frozen of droplets containing K-rich feldspar as a function of oxalic acid

concentration (0 M, olive; 5.2×10^{-5} M, violet; 1.04×10^{-4} M, magenta; 2.6×10^{-4} M, orange; 2.6×10^{-3} M, blue). Also included are the fraction frozen of pure water droplets (i.e., blanks) from multiple trials. Different symbols with the same color correspond to different trials. (b) Ice nucleating active site density (n_s) as a function of temperature calculated with the freezing data from panel (a). The error bars for n_s correspond to the 95% confidence intervals calculated with the nucleation statistics from Koop et al. (1997)..... 151

Figure C.4: Freezing data for the effect of azelaic acid on the ice nucleating ability of K-rich feldspar. (a) The fraction frozen of droplets containing K-rich feldspar as a function of azelaic acid concentration (0 M, olive; 5.2×10^{-5} M, violet; 1.04×10^{-4} M, magenta; 2.6×10^{-4} M, orange; 2.6×10^{-3} M, blue). Also included are the fraction frozen of pure water droplets (i.e., blanks) from multiple trials. Different symbols with the same color correspond to different trials. (b) Ice nucleating active site density (n_s) as a function of temperature calculated with the freezing data from panel (a). The error bars for n_s correspond to the 95% confidence intervals calculated with the nucleation statistics from Koop et al. (1997)..... 152

Figure C.5: Freezing data for the effect of phthalic acid on the ice nucleating ability of K-rich feldspar. (a) The fraction frozen of droplets containing K-rich feldspar as a function of phthalic acid concentration (0 M, olive; 5.2×10^{-5} M, violet; 1.04×10^{-4} M, magenta; 2.6×10^{-4} M, orange; 2.6×10^{-3} M, blue). Also included are the fraction frozen of pure water droplets (i.e., blanks) from multiple trials. Different symbols with the same color correspond to different trials. (b) Ice nucleating active site density (n_s) as a function of temperature calculated with the freezing data from panel (a). The error bars for n_s correspond to the 95% confidence intervals calculated with the nucleation statistics from Koop et al. (1997). 153

Figure C.6: Freezing data for the effect of acetic acid on the ice nucleating ability of K-rich feldspar.

(a) The fraction frozen of droplets containing K-rich feldspar as a function of acetic acid concentration (0 M, olive; 5.2×10^{-5} M, violet; 1.04×10^{-4} M, magenta; 2.6×10^{-4} M, orange; 2.6×10^{-3} M, blue). Also included are the fraction frozen of pure water droplets (i.e., blanks) from multiple trials. Different symbols with the same color correspond to different trials. (b) Ice nucleating active site density (n_s) as a function of temperature calculated with the freezing data from panel (a). The error bars for n_s correspond to the 95% confidence intervals calculated with the nucleation statistics from Koop et al. (1997). 154

Figure C.7: Freezing data for the effect of M5 on the ice nucleating ability of K-rich feldspar. (a)

The fraction frozen of droplets containing K-rich feldspar as a function of M5 concentration (0 M, olive; 5.2×10^{-5} M, violet; 1.04×10^{-4} M, magenta; 2.6×10^{-4} M, orange; 2.6×10^{-3} M, blue). Also included are the fraction frozen of pure water droplets (i.e., blanks) from multiple trials. Different symbols with the same color correspond to different trials. (b) Ice nucleating active site density (n_s) as a function of temperature calculated with the freezing data from panel (a). The error bars for n_s correspond to the 95% confidence intervals calculated with the nucleation statistics from Koop et al. (1997). 155

List of Symbols

A_{hom}	Arrhenius pre-exponential factor for homogeneous nucleation
A_{het}	Arrhenius pre-exponential factor for heterogeneous freezing
d	diameter
D	diffusion coefficient
i	van't Hoff factor for solutes
$INP(T)$	INP concentration at temperature T
J_{hom}	rate coefficient of homogeneous ice nucleation
J_{het}	rate coefficient of heterogeneous freezing
k	Boltzmann constant
km/h	kilometer per hour
K_f	freezing point depression constant
L	Liter
m	molality
m^2	square meter
M	mole per liter
mm	millimeter

min	minutes
nm	nanometer
n_m	number of ice nucleating active sites per gram of INPs
n_s	number of ice nucleating active sites per surface area of INPs
N	number of total droplets
N_u	number of unfrozen droplets
p	probability value
R	correlation coefficient
rpm	round per minute
R_H	hydrodynamic radius of a solute
s	second
S	surface area
T	temperature
Tg	teragram
$T_{50,solute}$	median freezing temperature of water droplets containing K-rich feldspar and solutes
T_{50,H_2O}	median freezing temperature of pure water droplets containing K-rich feldspar
V	volume

$V_{suspension}$	volume of water used to create suspension containing INPs
$V_{droplet}$	volume of droplets
V_{air}	volume of air sampled
$^{\circ}\text{C}$	Celsius degree
σ	interfacial tension between the new phase and the old phase
r	radius of the ice embryo
r^*	critical radius of the ice embryo
θ	contact angle between the ice embryo and the surface of an INP
μL	microliter
τ_{mix}	mixing time of a solute in water droplets
η	dynamic viscosity
ρ	density
Δt	a time interval
Δn_{ice}	number of droplets that freezing in the time interval Δt
ΔG	change of Gibbs free energy
Δg	difference of free energy per unit volume of the new phase and old phase
ΔG_{hom}^*	critical value of change in Gibbs free energy for homogenous ice nucleation

ΔG_{het}^*	critical value of change in Gibbs free energy for heterogeneous freezing
ΔT_f	freezing point depression caused by solutes
ΔT_{50}	change in the median freezing temperature due to the presence of solutes

List of Abbreviations

ATD	Arizona Test Dust
BET	Brunauer-Emmett-Teller
CCN	Cloud Condensation Nuclei
CNT	Classical Nucleation Theory
Cryo-XPS	Cryogenic X-ray Photoelectron Spectroscopy
EDX	Energy-Dispersive X-ray Spectroscopy
FLEXPART	Flexible Particle Dispersion Model
HYSPLIT	Hybrid Single Particle Lagrangian Integrated Trajectory
IC	Ion Chromatography
ICP-AES	Inductively Coupled Plasma Atomic Emission
INP	Ice Nucleating Particle
K-rich	Potassium-Rich
M5	Mixture of Malic Acid, Malonic Acid, Maleic Acid, Glutaric Acid, Methylsuccinic Acid
NCEP	National Centers for Environmental Prediction
PES	Potential Emission Sensitivity
SOA	Secondary Organic Aerosol

XRD

X-ray Diffraction

Acknowledgements

The successful completion of my PhD is impossible without support from many people. The foremost thank goes to my supervisor, Allan Bertram. I'm lucky to have you as my supervisor, Allan. The guidance and mentorship from you has made me grow as a scientist. And your continuous support and caring have made my PhD life more enjoyable.

During the past 5 years, I have enjoyed the atmosphere of the Bertram group. I want to thank for the accompany of former and current group members: Cedric, Christina, Michiael, Dagny, Vickie, Meng, Erin, Adrian, Yu, Yi, Kris, Jon, Jesse, Yuanzhou, Shaun, Soleil, both Nicoles, Anand, Fabian, and Julia. Cedric and Meng, thank you for passing on the knowledge and skills when I first join the group and start ice nucleation experiments. Fabian, Anand, Yuanzhou, and Shaun, I was having a lot of fun in those beer nights and board game nights.

I would also like to thank all the staff in the Chemistry Department for their assistance, especially members of the Mechanical Engineering shops and Chemistry Stores. My research would not have gone well without their help.

This dissertation includes two published journal articles and one article prepared for submission. I'm grateful to people below who have made contributions to these articles: Christopher Walters, Anita Lam, Dr. Mark Maclachlan, Dr. Andrey Shchukarev, Dr. Jean-Francois, and staff from Environment Canada. Especially I want to thank Dr. Jean-Francois for offering to do cryo-XPS analysis which greatly improved our papers.

I want to thank all friends who have supported me through my PhD. Chunxue, Qiyuan, Yuxiang, and Fan, I will always remember our Friday gaming nights, hikes, travels together.

Chunxue, thanks for your love and accompany in the last year of my PhD and I will always remember our fun dating nights.

Finally, I want to thank my parents for their unconditional love and support to me. Thank you for setting me a good example and inspiring me to pursue knowledge and now a PhD.

To my parents, Zhancai Yun and Xianzhen Zhang

Chapter 1. Introduction

1.1. Aerosols in the atmosphere

Aerosol is defined as a system of suspended liquid or solid particles in the atmosphere (Seinfeld and Pandis, 2006). Aerosol particles range from several nanometers to several hundred micrometers in diameter. These particles can be divided into the following modes based on size: the nucleation mode ($< 0.01 \mu\text{m}$), the Aitken mode ($0.01 \mu\text{m} - 0.1 \mu\text{m}$), the accumulation mode ($0.1 \mu\text{m} - 2.5 \mu\text{m}$), and the coarse mode ($> 2.5 \mu\text{m}$). Based on their mechanism of formation, aerosols can be classified into primary and secondary aerosols. Primary aerosol particles are directly emitted into the atmosphere, while secondary aerosols are formed through gas to particle conversion processes. Based on source type, aerosols can also be divided into natural aerosols and anthropogenic aerosols. Natural aerosols mainly include mineral dust from deserts, sea spray aerosols, volcanic ash, and primary biological particles. Anthropogenic aerosols mainly include industrial dust, organic aerosols from combustion of fossil fuel and biomass, and secondary aerosols, such as sulfates and nitrates. Aerosols are widely distributed in the atmosphere with varying number concentrations ($10^2 \text{ cm}^{-3} - 10^8 \text{ cm}^{-3}$) and composition (Seinfeld and Pandis, 2006). They can have a large impact on human health and the climate of the Earth (including the hydrological cycle and the radiative budget).

Aerosols can affect climate directly by scattering and absorbing incoming solar radiation and outgoing terrestrial radiation (Fig. 1.1). For example, sulfate particles can reflect incoming solar radiation back to space resulting in a cooling effect (Finlayson-Pitts and Pitts, 1999; IPCC, 2013), while black carbon particles can absorb incoming solar radiation resulting in a warming effect (Finlayson-Pitts and Pitts, 1999; Bond et al., 2013; IPCC, 2013). Alternatively, aerosols can

affect the climate indirectly (Fig. 1.1) by acting as cloud condensation nuclei (CCN) and ice nucleating particles (INPs) (Lohmann and Feichter, 2005). CCNs are responsible for the formation of liquid droplets in clouds. They can affect the optical properties of clouds by altering the number concentration and size of liquid droplets in clouds. INPs are aerosol particles that can initiate the formation of ice in clouds. The presence of ice crystals can affect the lifetime and optical properties of clouds, and hence, the radiative budget and hydrological cycle of the Earth (Lohmann and Feichter, 2005; DeMott et al., 2010; Lohmann et al., 2016; Storelvmo, 2017; Kudzotsa et al., 2018; Takeishi and Storelvmo, 2018). The focus of this thesis is on INPs in the atmosphere.

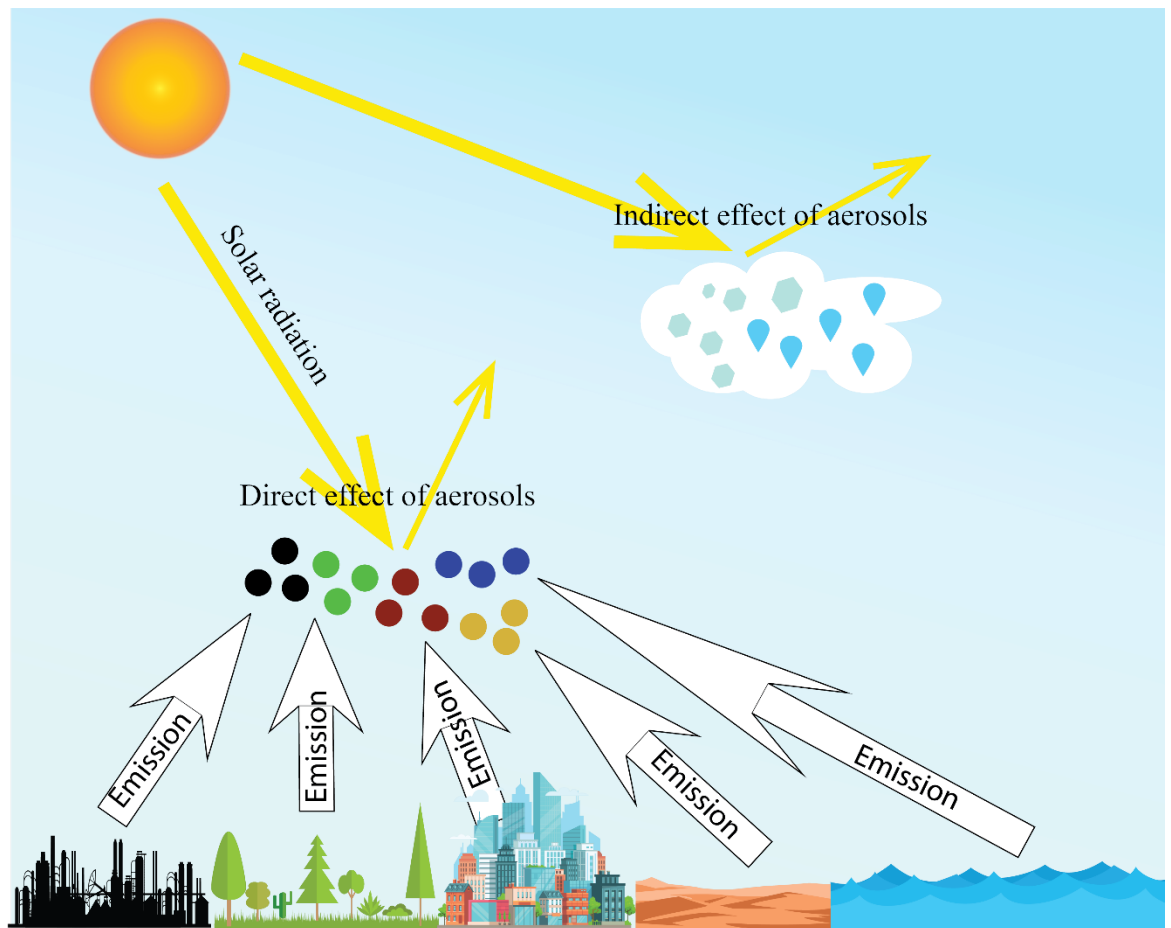


Figure 1.1: Schematic for direct effect and indirect effect of aerosols on the climate.

1.2. Ice nucleation in the atmosphere

1.2.1. Mechanism of ice formation in clouds

Formation of ice crystals in clouds can be initiated by two mechanisms: homogeneous freezing and heterogeneous ice nucleation (Pruppacher and Klett, 1997). Both mechanisms can be explained by classical nucleation theory (CNT) (see Appendix A for details). Homogeneous freezing refers to the freezing of a cloud droplet without the aid of a foreign nucleus and usually happens at approximately $-35\text{ }^{\circ}\text{C}$ to $-38\text{ }^{\circ}\text{C}$ in the atmosphere (Murray et al., 2010). Heterogeneous ice nucleation is induced by INPs, which lowers the energy barrier of ice nucleation. Heterogeneous ice nucleation can occur by different modes (Vali et al., 2015) (Fig. 1.2): 1) deposition ice nucleation, which refers to ice formation on the surfaces of INPs directly from water vapor under liquid water sub-saturated conditions; 2) condensation/immersion freezing, which refers to the freezing of water droplets triggered by INPs immersed in the droplets; 3) contact freezing, which refers to the freezing of water droplets initiated by collision with INPs; 4) pore condensation freezing, which refers to water vapor first condensing in nanometer-sized pores of an INP followed by freezing of the condensed water and growth of the ice embryo (Marcolli, 2014; David et al., 2019). This dissertation focuses on INPs in the immersion freezing mode, which is the dominant pathway for ice formation in mixed-phase clouds.

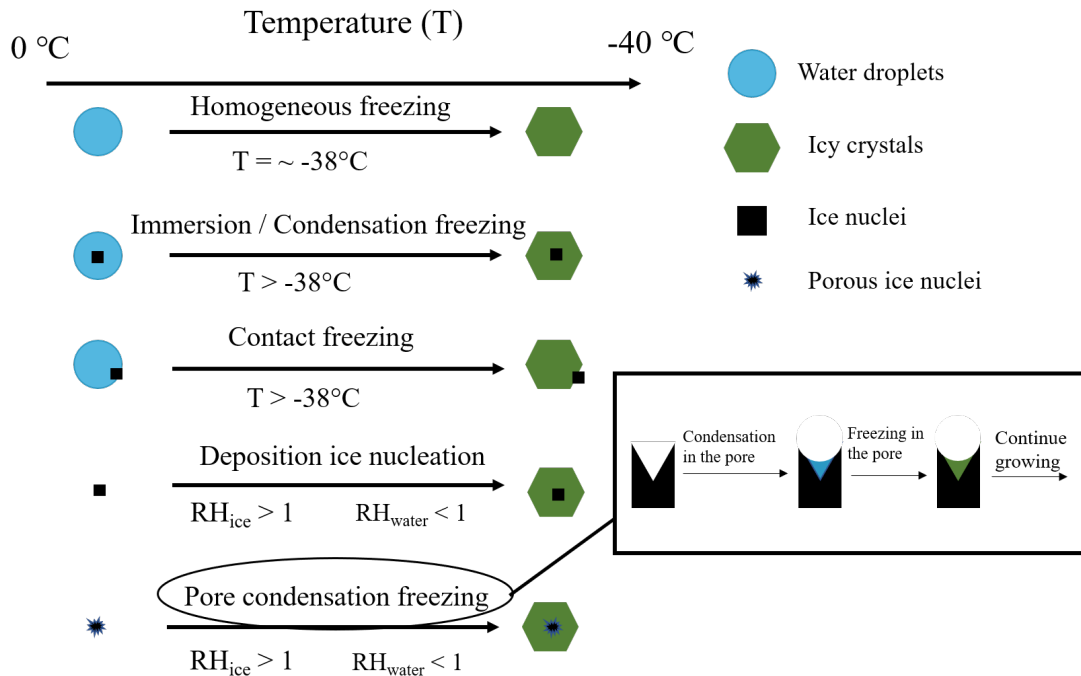


Figure 1.2: Schematic for different modes of ice nucleation in the atmosphere.

1.2.2. The effect of INPs on earth's climate

Clouds can be divided into liquid clouds, mixed-phase clouds, and ice clouds based on their phases (Lohmann et al., 2016). Mixed-phase clouds are composed of both liquid droplets and ice crystals and form at an altitude of 2 – 7 km. The solar radiation reflected by mixed-phase clouds is more than the infrared radiation absorbed resulting a net cooling effect on the Earth for mixed-phase clouds (Hartmann et al., 1992; Chen et al., 2000). Ice crystals in mixed-phase clouds form by heterogeneous freezing as the temperatures in mixed-phase clouds are too warm for homogeneous freezing. In mixed-phase clouds, more INPs lead to more freezing of cloud droplets into ice crystals. Due to a lower saturation vapor pressure of ice compared to liquid water, ice crystals will grow at the expense of liquid water in mixed-phase clouds. This process is also known as the Wegener-Bergeron-Findeisen process, which can further reduce the amount of liquid water and increase the amount of ice (Pruppacher and Klett, 1997). More ice and less liquid water will

lead to more precipitation, a shorter lifetime of mixed-phase clouds, and less reflection of solar radiation. Therefore, more INPs will offset the net cooling effect of mixed-phase clouds (Lohmann, 2002; Lohmann and Feichter, 2005; DeMott et al., 2010). The work presented in this thesis is most relevant for mixed-phase clouds.

Ice clouds are composed of only ice crystals and form at an altitude of 7 – 18 km (Lynch et al., 2002). Ice clouds absorb more infrared radiation compared to the solar radiation they reflect. Therefore, they have a net warming effect on the Earth's climate (Hartmann et al., 1992; Chen et al., 2000; Seinfeld and Pandis, 2006). In ice clouds, ice can form both homogeneously and heterogeneously (Kärcher and Lohmann, 2002; DeMott et al., 2003; Cziczo et al., 2004, 2013). Although the effect of INPs on ice clouds is not yet fully understood, more INPs are believed to result in fewer but larger ice crystals in ice clouds since the increase of heterogeneous freezing at an earlier onset can deplete water droplets, thereby suppressing homogeneous freezing (Kärcher and Lohmann, 2003). As a result, more INPs can accelerate sedimentation, reduce the optical depth of the clouds, and overall reduce the net warming effect of ice clouds (DeMott et al., 2010; Hendricks et al., 2011).

Despite the importance of INPs for climate and precipitation, the scientific understanding of the composition, concentrations, and sources of INPs in the atmosphere remains uncertain.

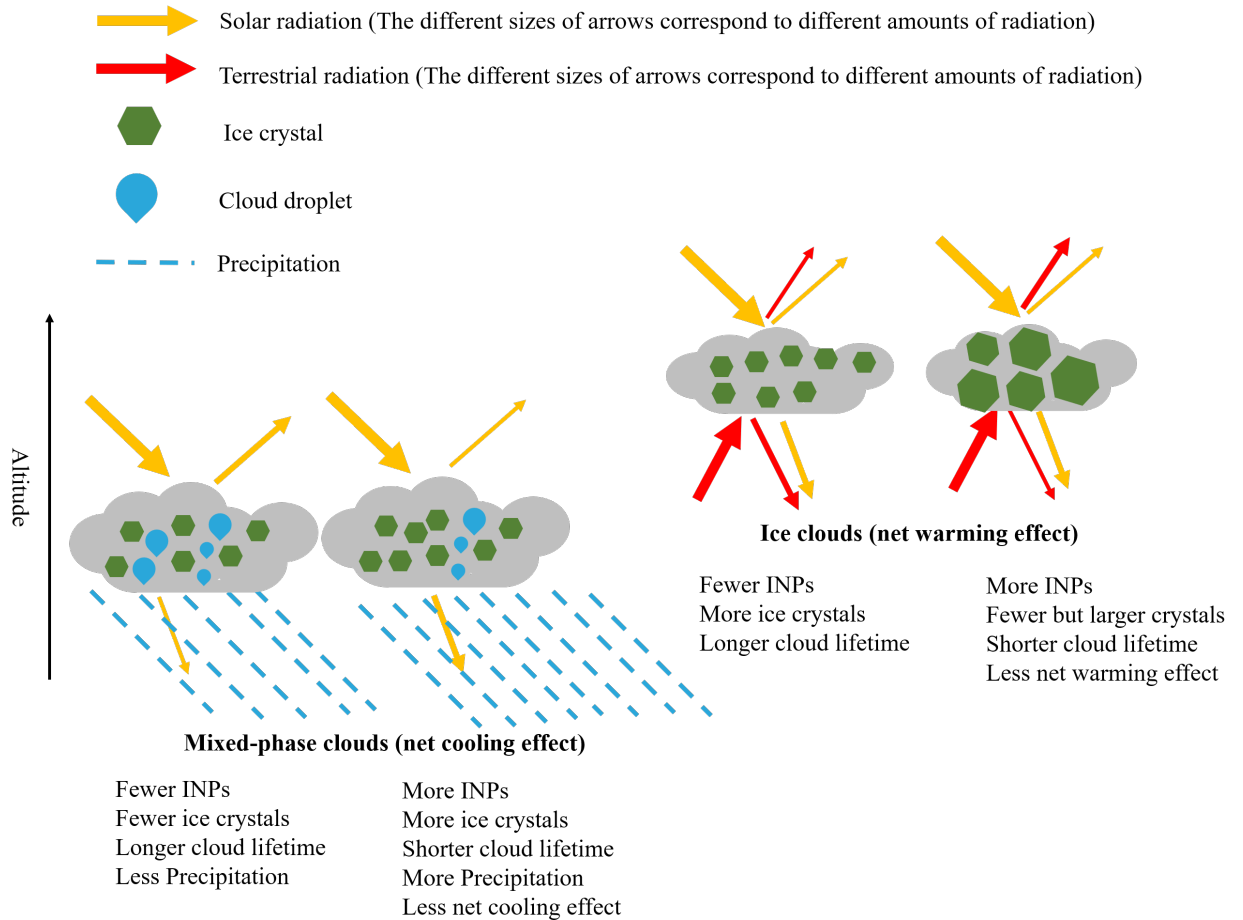


Figure 1.3: Schematic for the climatic effect of INPs on mixed-phase clouds and ice clouds. Adapted from DeMott et al. (2010).

1.2.3 Types of INPs in the atmosphere

Pruppacher and Klett (1997) have summarized a few general requirements for an aerosol particle to be an effective INP: 1) the particle needs to be insoluble or at least partially insoluble to provide a solid surface; 2) the surface of the particle needs to form hydrogen bonds with water molecules; 3) the particle has to be larger than 0.1 μm in diameter; 4) the crystallography of the aerosol particle needs to match with ice; 5) there should be defects, such as cracks and cavities, at the surface of the aerosol particle. As a result, INPs are only a small subset of total aerosol particle population. Approximately 1 in 10^5 atmospheric particles is an INP (Rogers et al., 1998).

Although the above conditions are required for an INP in general, there are some INPs that do not strictly meet these requirements. For example, some studies have shown that soluble salts and soluble organic acids can act as INPs in the deposition and immersion freezing mode (Zuberi et al., 2001; Shilling et al., 2006; Zobrist et al., 2006; Wagner et al., 2011; Wagner and Möhler, 2013; Knopf et al., 2018). In addition, some glassy organic aerosols with non-crystalline structure can also nucleate ice in the deposition freezing mode (Murray et al., 2010; Wang and Knopf, 2011; Wang et al., 2012; Knopf et al., 2018).

In the atmosphere, the main INPs include the following types of aerosol particles: 1) mineral dust; 2) biological particles; 3) combustion particles; 4) organic and glassy particles; 5) crystalline salts (Hoose and Möhler, 2012; Murray et al., 2012; Kanji et al., 2017). This thesis mainly focuses on mineral dust and biological INPs.

1.2.3.1. Mineral dust INPs

Mineral dust particles are ubiquitous in the atmosphere, with an emission flux to the atmosphere of 1000-4000 Tg per year, making up 13% of the natural aerosol mass flux to the atmosphere (Gieré and Querol, 2010). The source of mineral dust in the atmosphere is mainly wind-blown dust from arid and semi-arid regions represented by the “dust belt” extending from the Sahara Desert, over the Middle East, Central and South Asia, to China (Prospero et al., 2002). Dust from volcanic activity and anthropogenic activity, such as transportation and agriculture, are also important (Seinfeld and Pandis, 2006). The lifetime of mineral dust is approximately 2 weeks, during which mineral dust can travel over long distances, far away from their sources (Duce et al., 1980; Schütz, 1980; Merrill et al., 1989; Prospero, 1999; van der Does et al., 2018). The composition of atmospheric mineral dust has been characterized in numerous field studies. On

average, clays, feldspars, quartz, and calcite are the major constituents, although the mineralogy also depends on sampling location and time (Murray et al., 2012).

Laboratory studies have shown that the main types of mineral dust, including clays, feldspars, quartz, and natural dust collected from the Earth's surface, are efficient INPs (Field et al., 2006; Knopf and Koop, 2006; Eastwood et al., 2008; Kanji and Abbatt, 2010; Murray et al., 2011; Atkinson et al., 2013; Wex et al., 2014; Hiranuma et al., 2015; Boose, Welti, et al., 2016). In addition, field measurements have shown that the concentrations of INPs in the atmosphere often correlate with mineral dust, and mineral dust is often the main component of ice residual in clouds (Prenni, Demott, et al., 2009; Cziczo et al., 2013; Worringen et al., 2015). Modelling studies have also shown that mineral dust is a major contributor to INP population in the atmosphere (Corinna Hoose et al., 2010; Vergara-Temprado et al., 2017). Among all of the types of minerals studied, potassium-rich feldspar (K-rich feldspar) has the best ice nucleating ability (Augustin-Bauditz et al., 2014; Zolles et al., 2015; Harrison et al., 2016; Kaufmann et al., 2016; Peckhaus et al., 2016; Kiselev et al., 2017). Some global modelling studies have used K-rich feldspar to predict the global INP distribution (Atkinson et al., 2013; Vergara-Temprado et al., 2017).

1.2.3.2. Biological INPs

Biological aerosols are less abundant than mineral dust in the atmosphere, with an emission to the atmosphere of less than 10 Tg to 1000 Tg per year (Després et al., 2012). They are biological organisms or dispersal units, such as bacteria, fungi, spores, and pollen, or fragments of these organisms and dispersal units (Després et al., 2012). The sources of biological aerosols are all living things in the biosphere, including plants, animals, microorganisms, and humans (Després et al., 2012).

Although biological aerosols are a smaller subset of the total aerosol population than mineral dust, laboratory studies have shown that some proteinaceous materials in biological aerosols have exceptionally high ice nucleating ability and can induce heterogeneous freezing at warm temperatures, up to $-2\text{ }^{\circ}\text{C}$ (Lindemann et al., 1982; Kieft, 1988; Constantinidou et al., 1990; Kieft and Ruscetti, 1990; Pouleur et al., 1992; Richard et al., 1996; Diehl et al., 2002; Möhler et al., 2008; Morris et al., 2008; Knopf et al., 2011; Peter A. Alpert et al., 2011; Pummer et al., 2012). Field measurements have also suggested that biological aerosols are potentially important regional INPs, especially at warm temperatures, which are relevant for mixed-phase clouds (Christner et al., 2008; Bowers et al., 2009; Pratt et al., 2009; Prenni, Petters, et al., 2009; Conen et al., 2011; Garcia et al., 2012). Although the effect of biological particles on the climate via ice nucleation has been investigated in numerous modelling studies, our understanding of this topic is still far from complete due to limited data of atmospheric biological INP concentrations (Diehl et al., 2006; Grützun et al., 2008; Phillips et al., 2009; C. Hoose et al., 2010; Diehl and Wurzler, 2010; Sesartic et al., 2012, 2013; Sahyoun et al., 2017; Hummel et al., 2018). Constraints on biological INPs in the atmosphere are needed to better resolve the uncertainty of aerosol-cloud interactions.

1.3 Description of data from freezing experiments

In order to predict concentrations of INPs in atmospheric models, the ice nucleating ability of atmospheric particles needs to be quantified. There are two ways to describe the ice nucleating ability of atmospheric particles: the stochastic description and the singular description (Murray et al., 2012).

1.3.1 Stochastic description

The stochastic description is based on the nucleation process being a stochastic process. For the stochastic description, the occurrence of freezing events is dependent on both time and

surface area of the INPs (Kashchiev, 2000; Mullin J., 2001; Murray et al., 2012). Consider an array of droplets containing INPs and a given time interval, Δt . In the single component stochastic description, the number of droplets freezing in Δt is calculated with the following equation:

$$\frac{\Delta n_{ice}(T)}{N} = 1 - \exp(-J_{het}(T)S\Delta t) \quad (1.1),$$

where Δn_{ice} is the number of droplets that freeze in Δt , N is the number of total droplets, J_{het} is the heterogeneous freezing rate coefficient for the INP, and S is the surface area of the INP in each droplet. In the multiple component stochastic description, the number of droplets freezing in Δt is calculated with the following equation:

$$\frac{\Delta n_{ice}(T)}{N} = 1 - \exp(-\sum J_{het,i}(T)S_i\Delta t) \quad (1.2),$$

where $J_{het,i}$ is the heterogeneous freezing rate coefficient for the INP of type i and S_i is the surface area of the ice nucleating material of type i in each droplet.

1.3.2 Singular description

The singular description assumes that the time dependence is of secondary importance compared to the ice nucleation properties of aerosol particles and can be neglected (Vali, 1994, 2008; Pruppacher and Klett, 1997; Murray et al., 2012). Using the singular description, the number of frozen droplets as a function of temperature can be calculated with the following equation:

$$\frac{\Delta n_{ice}(T)}{N} = 1 - \exp(-n_s(T)S) \quad (1.3),$$

where $\Delta n_{ice}(T)$ is the number of frozen droplets at temperature T , N is the number of total droplets, S is the surface area of the ice nucleating material in each droplet, and $n_s(T)$ is the density of surface sites that are ice active at temperature T , also referred to as the ice nucleating active site density (Vali et al., 2015). This value refers to the number of sites per unit surface area of INPs

that can cause ice nucleation at temperature T , and this value is used to quantify the freezing ability of INPs and allows for easy comparison between the freezing ability of different types of INPs.

This dissertation uses the singular description to assess the ice nucleation properties of particles, since previous studies have shown that in immersion freezing experiments the time dependence is of secondary importance compared to the surface area of INPs.

1.4. Effects of solutes on the freezing of cloud droplets.

Within the lifetime of INPs in the atmosphere, INPs can become coated with water-soluble materials, before being activated into cloud droplets (Tinsley et al., 2000; Usher et al., 2003; Hinz et al., 2005; McNaughton et al., 2009; Ma et al., 2012; He et al., 2014). Numerous field studies have also shown that cloud droplets contain various types of solutes, including both inorganic and organic materials (Gioda et al., 2011; Van Pinxteren et al., 2016; Cook et al., 2017).

Solutes can affect the freezing of cloud droplets by two mechanisms: lowering the chemical potential of solutions (Fig. 1.4) and modifying the surface properties of INPs. In the first mechanism, solutes can lower the chemical potential of solutions and hence lower the driving force for nucleation. For dilute solutions, the freezing point depression by solutes through the first mechanism can be estimated with the following equation (Atkins and Paula, 2009):

$$\Delta T_f = K_f \cdot m \cdot i \quad (1.4),$$

where K_f is the freezing point depression constant ($1.86 \text{ }^\circ\text{C} \cdot \text{mol} \cdot \text{kg}^{-1}$), m is the molality of the solutes, and i is the van't Hoff factor for the solutes. For concentrated solutions, the freezing point depression caused by solutes through the first mechanism can be estimated with a water activity model (Koop et al., 2000; Koop and Zobrist, 2009). Several laboratory experiments have shown that freezing point depression expected from the first mechanism can explain the effect of solutes on the freezing of droplets (Zobrist et al., 2008; Koop and Zobrist, 2009; Sullivan, Miñambres, et

al., 2010; Knopf et al., 2011; P. A. Alpert et al., 2011; Peter A. Alpert et al., 2011; Knopf and Alpert, 2013; Rigg et al., 2013; Wex et al., 2014).

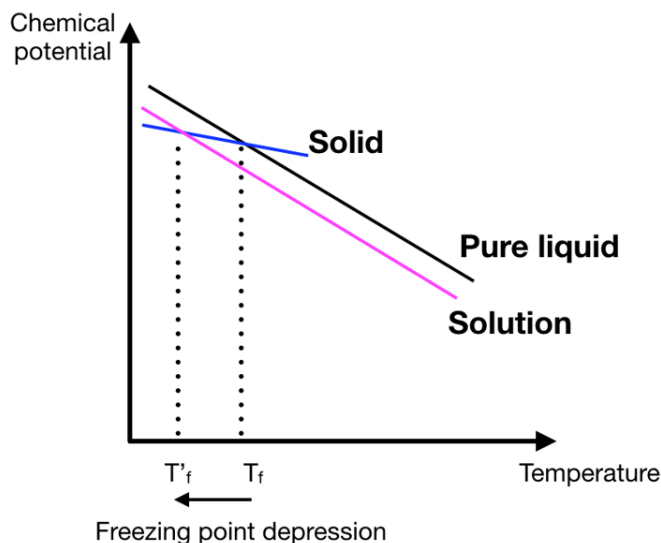


Figure 1.4: Schematic for the freezing point depression of solutes due to lowering the chemical potential of solutions. The blue line represents the chemical potential of a solid phase (ice in this case) as a function of temperature. The black line represents the chemical potential of a pure liquid phase (pure liquid water in this case) as a function of temperature. The magenta line represents the chemical potential of a solution phase (aqueous solution in this case) as a function of temperature. T_f represents the freezing point of pure water and T'_f represents the freezing point of the aqueous solution.

Numerous laboratory measurements have shown that some solutes can alter the surface properties of INPs and change the freezing temperatures more than expected based on the freezing point depression (Reischel and Vali, 1975; Kumar et al., 2018, 2019b, 2019a; Whale et al., 2018; Perkins et al., 2020; Yun et al., 2020; Worthy et al., 2021). For example, previous studies showed that the ice nucleating ability of feldspars, quartz, and clay minerals was significantly enhanced when suspended in ammonium-containing solutions (Kumar et al., 2018, 2019b; Whale et al., 2018; Worthy et al., 2021), while the ice nucleating ability of feldspars was significantly suppressed by sodium salts (Kumar et al., 2018; Whale et al., 2018; Perkins et al., 2020; Yun et

al., 2020). Given that solutes are ubiquitous in cloud droplets, a more comprehensive understanding of solute effects on the ice nucleating ability of atmospherically relevant particles is needed to more accurately predict ice formation in the atmosphere.

1.5. Motivation for laboratory and field studies of INPs

Both laboratory studies and field measurements are needed to better understand INPs. An important advantage of laboratory studies is that properties of INPs can be examined systematically under well-controlled conditions. For example, in laboratory studies a single type of particle can be used in freezing experiments and hence n_s values for different types of INPs found in the atmosphere can be determined. In this dissertation, laboratory studies were performed to systematically quantify the effect of solutes on the ice nucleating ability of mineral dust since in the atmosphere, solutes, even at low concentrations, can significantly affect the freezing ability of INPs and hence impact climate indirectly, as discussed above.

Besides laboratory studies, field studies are also needed to quantify the concentrations, properties, and sources of INPs in the real atmosphere to provide data for climate models. An area where field studies are especially needed is the Arctic region, which is a focus of this dissertation. In the Arctic, mixed-phase clouds are abundant and play an important role in climate and precipitation in the region (Shupe, 2011; Morrison et al., 2012). As discussed in Section 1.2.2, INPs can modify the properties of these clouds, including their lifetime and optical properties, by changing the ratio of ice to liquid water in these clouds (Lohmann and Feichter, 2005; Lohmann et al., 2016; Storelvmo, 2017; Kudzotsa et al., 2018; Takeishi and Storelvmo, 2018). Acquiring information on the concentration, properties, and sources of INPs in the Arctic is critical to predict climate in this region.

Studies have shown that the temperature in the Arctic is increasing more rapidly compared to lower-latitude regions (Serreze and Francis, 2006; IPCC, 2013; Cohen et al., 2014). This phenomenon is also known as Arctic Amplification. As the temperature increases in the Arctic (Serreze and Francis, 2006; IPCC, 2013; Cohen et al., 2014), sea ice and land snow are expected to decrease (Derksen and Brown, 2012). This decrease in sea ice and land snow may lead to a change in the sources and fluxes of INPs to the Arctic atmosphere (Tobo et al., 2019), leading to possible changes in the properties of mixed phase clouds, climate, and hydrological cycle in the region. Hence, knowledge of the concentrations, composition, and sources of INPs in the Arctic is needed to accurately predict climate feedbacks in the region.

1.6. Overview of Dissertation

This thesis includes studies on the ice nucleation properties of mineral dust via laboratory-based experiments and aerosol samples collected in the Arctic. Chapter 1 gives a general introduction to INPs in the atmosphere and highlights the importance of studying the properties of atmospheric INPs. Chapters 2-4 are research chapters. Chapter 5 is a summary of this thesis and presents ideas for future research.

Chapter 2 investigates the effect of alkali cations Li^+ , Na^+ , K^+ , Rb^+ , and Cs^+ on the ice nucleating ability and the surface composition of K-rich feldspar using the droplet freezing technique and cryogenic X-ray photoelectron spectroscopy (cryo-XPS). The relation between the surface composition and the ice nucleating ability of K-rich feldspar is discussed. Chapter 3 focuses on the effect of inorganic acids (HCl and HNO_3) and organic solutes (carboxylic acids and polyols) on the ice nucleating ability of K-rich feldspar using similar techniques as in Chapter 2. The effect of H^+ on the surface composition of K-rich feldspar was also investigated with cryogenic X-ray photoelectron spectroscopy. Based on the results of freezing experiments and

cyro-XPS experiments, the mechanisms for the inorganic acids and carboxylic acids decreasing the ice nucleating ability of K-rich feldspar are discussed in this chapter.

Chapter 4 presents the results of a field campaign conducted at a site in the Canadian High Arctic during the fall of 2018. The contributions of mineral dust and proteinaceous particles to the total INP population were evaluated by testing the responses of the INP concentrations of the samples to heat treatment and ammonium sulfate treatment. Possible source regions of the INPs were investigated by combining results from particle dispersion modelling and a correlation analysis between concentrations of INPs and Al, Na⁺, and Cl⁻.

Chapter 2: Surface composition dependence on the ice nucleating ability of potassium-rich feldspar

2.1 Introduction

Mineral dust particles are an important type of INP in the atmosphere. Laboratory studies have shown that certain types of mineral dust particles, such as feldspars and clays are able to initiate ice formation at temperatures significantly warmer than temperatures required for homogeneous freezing (Hoose and Möhler, 2012; Murray et al., 2012; Tang et al., 2016; Kanji et al., 2017). Field measurements and modelling studies have also shown that mineral dust particles make up a large fraction of the total population of atmospheric INP (Prenni, Demott, et al., 2009; Corinna Hoose et al., 2010; Cziczo et al., 2013; Boose, Sierau, et al., 2016; Vergara-Temprado et al., 2017; O’Sullivan et al., 2018; Irish, Hanna, Willis, et al., 2019; Si et al., 2019).

Mineral dust particles can be transported over long distances in the atmosphere far from their sources (Duce et al., 1980; Schütz, 1980; Merrill et al., 1989; Prospero, 1999; van der Does et al., 2018). During their transport, these particles can become coated with water-soluble solutes by coagulation with other aerosol particles, condensation of gases, multiphase reactions, or cloud processing (Tinsley et al., 2000; Usher et al., 2003; Hinz et al., 2005; McNaughton et al., 2009; Ma et al., 2012; He et al., 2014). These water-soluble solutes can subsequently modify the ice nucleating properties of mineral dust particles.

In the immersion freezing mode, solutes can affect the ice nucleating properties of mineral dust particles by decreasing the water activity in the liquid droplets (i.e. freezing point depression) (Koop et al., 2000; Zobrist et al., 2008; Koop and Zobrist, 2009; Knopf and Alpert, 2013). In

addition, solutes can affect the ice nucleating properties of mineral dust particles in the immersion freezing mode by partitioning to or reacting with the surfaces of the mineral dust particles. Several recent studies have shown that the latter mechanism is important even at low solute concentrations. For example, several studies have shown that ammonia and ammonium salts at 10^{-3} M to 10^{-1} M increase the ice nucleating ability of several types of mineral dust particles (feldspars, kaolinite gibbsite, and mica) (Kumar et al., 2018, 2019a, 2019b; Whale et al., 2018). Reischel and Vali (1975) have also shown that LiI at low concentrations (10^{-1} M) also increases the ice nucleating ability of kaolinite particles. On the other hand, several studies have shown that sodium salts and potassium salts at 10^{-3} M to 10^0 M can decrease the ice nucleating ability of some types of mineral dust particles (feldspars and Arizona Test Dust) (Kumar et al., 2018, 2019b; Whale et al., 2018; Perkins et al., 2020). Other studies have shown that strong acids even at low concentrations decrease the ice nucleating ability of some minerals, depending on reaction time, and the type of acid and minerals (Cziczo et al., 2009; Sullivan, Petters, et al., 2010; Augustin-Bauditz et al., 2014; Wex et al., 2014; Burkert-Kohn et al., 2017). Although these combined studies have shown that solutes at low concentrations can modify the ice nucleating ability of mineral dust particles, our understanding of the effects of solutes on the ice nucleating ability of mineral dust particles remains incomplete. For example, the reason why some water-soluble solutes improve the ice nucleating ability of mineral dust particles while others decrease the ice nucleating ability is not well understood. A better understanding of the effects of water-soluble solutes on the ice nucleating properties of mineral dust particles is needed for accurate predictions of ice nucleation in the atmosphere.

To improve our understanding of the effects of water-soluble solutes on the ice nucleating properties of mineral dust particles, we investigated the ice nucleating ability and surface

composition of potassium-rich feldspar (K-rich feldspar) in the immersion mode in the presence of a series of alkali metal nitrates (LiNO_3 , NaNO_3 , KNO_3 , RbNO_3 and CsNO_3). The immersion freezing experiments were performed using the droplet freezing technique, and the surface composition was determined using cryogenic X-ray photoelectron spectroscopy (cryo-XPS). By holding the anion (i.e., NO_3^-) constant, we isolated the effects of the alkali metal cation on the ice nucleating properties and surface composition of K-rich feldspar. The concentration of alkali metal cations used in our experiments ranged from 5×10^{-5} M to 5×10^{-3} M, which is relevant for mixed phase clouds in the atmosphere (Reischel and Vali, 1975). K-rich feldspar was used in this study because it is an effective ice nucleus (Augustin-Bauditz et al., 2014; Zolles et al., 2015; Harrison et al., 2016; Kaufmann et al., 2016; Peckhaus et al., 2016; Kiselev et al., 2017) and thought to be an important component of atmospheric INPs (Atkinson et al., 2013; Boose, Welti, et al., 2016; Vergara-Temprado et al., 2017).

2.2 Experimental

2.2.1 Chemicals

A K-rich feldspar sample was obtained from the Pacific Museum of Earth, University of British Columbia, and ground into powder using a mortar and pestle. Based on the Brunauer-Emmett-Teller (BET) nitrogen adsorption method, the specific surface area of the powder was $0.75 \text{ m}^2/\text{g}$. Based on X-ray diffraction (XRD) measurements and a Rietveld analysis (Rietveld, 1969), the composition of the powder, after micronizing to $<10 \text{ }\mu\text{m}$ for XRD data collection, was 85% microcline (KAlSi_3O_8) and 15% albite ($\text{NaAlSi}_3\text{O}_8$).

Milli-Q water and the following inorganic salts (including vendor and purity) were used to prepare solutions and suspensions: LiNO_3 (Sigma-Aldrich, $\geq 95\%$), NaNO_3 (Caledon, $\geq 99\%$), KNO_3 (Caledon, $\geq 99\%$), RbNO_3 (Sigma-Aldrich, 99.7%), and CsNO_3 (Sigma-Aldrich, $\geq 99\%$).

2.2.2 Droplet freezing technique

The freezing experiments were carried out using the droplet freezing technique (Fig. 2.1) as described in (Whale et al., 2015) and used previously in our laboratory to study immersion freezing (Irish et al., 2017). The freezing apparatus consisted of a cold stage (Grant Aymptote EF600) covered by an airtight chamber. In the freezing experiments, 20 droplets with a volume of 2 μL each were pipetted onto a hydrophobic glass slide (Hampton Research) located on the cold stage. After depositing the droplets and covering the cold stage with the airtight chamber, the temperature of the cold stage was decreased from 20 $^{\circ}\text{C}$ to 2 $^{\circ}\text{C}$ at a rate of 10 $^{\circ}\text{C}/\text{min}$, then decreased at a rate of 3 $^{\circ}\text{C}/\text{min}$ until all the droplets froze. Based on the manufacturer's specification, the uncertainty in the temperature measurement is ± 0.25 $^{\circ}\text{C}$. This was verified by measuring the melting temperatures of water and dodecane and comparing with melting temperatures reported in the literature (0 $^{\circ}\text{C}$ for water and -9.6 $^{\circ}\text{C}$ for dodecane) (Haynes et al., 2014). A camera was located above the cold stage to record the freezing temperature of the droplets. The freezing temperature of each droplet was determined from the recorded temperature and the videos, which were analyzed manually or with a MATLAB script (Xi et al., 2021). During the freezing experiments, a small flow of dry nitrogen gas (flow rate = 0.2 L/min) was passed through the chamber to prevent the growth of frost on the slides. Observations of the droplets during the freezing experiments confirmed that the small flow of dry nitrogen gas did not cause significant evaporation of the droplets.

Freezing experiments were repeated six times with a different set of droplets for each repetition. Uncertainties in reported freezing temperatures were based on the uncertainty of the temperature measurements (i.e., 0.25 $^{\circ}\text{C}$) and 95 % confidence intervals based on the Student's *t*-distribution.

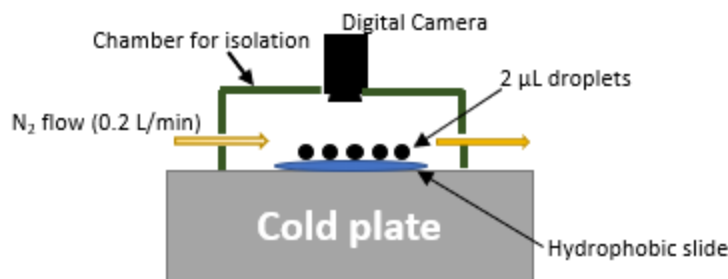


Figure 2.1: Schematic of the setup for the freezing experiments.

The following procedure was used to generate 2 μL droplets containing water, K-rich feldspar, and solutes on the hydrophobic glass slides. First, for each new day of experiments, a new suspension of K-rich feldspar (0.1 wt %) in water was made and stirred overnight. After stirring overnight, 1 μL droplets of the suspension were pipetted onto hydrophobic glass slides, and then a second 1 μL droplet of nitrate solution (or pure water for comparison purposes) was pipetted on to each original droplet produced from the suspension. This resulted in the droplets having a volume of 2 μL and containing K-rich feldspar with a concentration of 0.05 wt %. Based on calculations of diffusion rates of solutes in water (Appendix B, Table B.1 and Section B.1), the solutes had sufficient time to mix within the droplets prior to freezing.

In addition to measuring the freezing temperatures of 2 μL droplets containing water, K-rich feldspar, and solutes (i.e., samples), we also measured the freezing temperature of 2 μL droplets consisting of just Milli-Q water (i.e. blanks). The fraction frozen of the blank droplets were subtracted from the fraction frozen of sample droplets. However, subtraction of the blanks did not significantly influence the results, since the overlap in the freezing temperatures of the blanks and samples was small, if at all.

2.2.3 Freezing point depression correction

Solutes can decrease the freezing temperature by lowering the water activity in the solution (i.e. freezing point depression). The freezing point depression for dilute solutions can be estimated with the following equation (Atkins and Paula, 2009):

$$\Delta T_f = K_f \cdot m \cdot i \quad (2.1)$$

where ΔT_f is the estimated freezing point depression, K_f is the freezing point depression constant ($1.86 \text{ }^\circ\text{C} \cdot \text{mol} \cdot \text{kg}^{-1}$), m is the molality of the solutes, and i is the van't Hoff factor (2 for alkali metal nitrates). Molality of the solutes (m) were calculated from the molarity of the solutes (M) used in our experiments. Based on this equation and the solute concentrations used in our experiments ($5 \times 10^{-5} \text{ M}$ to $5 \times 10^{-3} \text{ M}$), the freezing point depression caused by the solutes was small ($< 0.1 \text{ }^\circ\text{C}$), and smaller than the uncertainty of our temperature measurements ($0.25 \text{ }^\circ\text{C}$). Hence, no correction was applied to the freezing temperatures to account for the freezing point depression.

2.2.4 Cryogenic X-ray photoelectron spectroscopy (cryo-XPS)

The relative abundance of atoms at K-rich feldspar surfaces before and after exposure to the solutes (or pure water) was determined with cryo-XPS (Shchukarev and Ramstedt, 2017). Cryo-XPS gives ratios of atoms at the mineral/aqueous interface under near in-situ conditions, and this technique has been used previously to determine surface loadings of weakly bound electrolytes at mineral/aqueous interfaces (Kozin et al., 2013; Shimizu et al., 2013). For the cryo-XPS analysis, a suspension of K-rich feldspar (0.1 wt %) in water was stirred overnight. After stirring overnight, the K-rich feldspar suspensions was mixed with nitrate solutions (10^{-2} M) in equal amounts resulting in suspensions containing K-rich feldspar (0.05 wt %) and alkali metal nitrates ($5 \times 10^{-3} \text{ M}$). After mixing, the suspensions were stirred for approximately 15 minutes and centrifuged for

10 minutes at 5000 rpm. The supernatant was then decanted, resulting in a wet paste with a high solid-to-water ratio. The wet paste was then smeared onto a molybdenum sample holder. The sample holder was then loaded onto the precooled (-170 °C) sample transfer rod and held at a vacuum of $4-5 \times 10^{-5}$ Pa during freezing. The fast-frozen wet paste sample was thereafter transferred to the precooled (-155 °C) sample manipulator in the analysis chamber for XPS spectra collection. The collected spectra were processed with Kratos software to obtain the relative abundance of elements at the K-rich feldspar surfaces. The total exposure time of K-rich feldspar surfaces to alkali nitrates in the cryo-XPS experiments (~25 minutes) was similar to the total exposure time in the freezing experiments (15 – 20 minutes).

Since samples are centrifuged and aqueous solutions are decanted prior to cryo-XPS measurements, only a thin layer (~ 1 nm) of ice is detected on mineral surfaces in cryo-XPS measurements (Shchukarev and Ramstedt, 2017). For our studies, the sampling depth of the cryo-XPS measurements was 5-6 nm. As a result, approximately 4-5 nm of the K-rich feldspar surfaces were probed in our cryo-XPS measurements.

2.3 Results and Discussion

2.3.1 Ice nucleating ability of K-rich feldspar in pure water

Fig. 2.2a shows the fraction frozen of droplets containing K-rich feldspar (0.05 wt %) in pure water (i.e. no solutes) as a function of temperature. Also included are the fraction frozen of 2 μ l pure Milli-Q water droplets (i.e. blanks) for comparison. The presence of K-rich feldspar in the droplets increased the median freezing temperatures by approximately 10 °C. Fig. 2.2b shows the ice nucleating active site density (n_s) values of K-rich feldspar as a function of temperature, calculated using the freezing data from Fig. 2.2a and the following equation (Vali et al., 2015):

$$n_s(T) = -\ln \left(\frac{N_u(T)}{N} \right) / S \quad (2.2)$$

where $N_u(T)$ is the number of unfrozen droplets at temperature T , N is the number of total droplets, and S is the average surface area of K-rich feldspar in a droplet. We used a value of $0.75 \text{ m}^2/\text{g}$ for S based on the BET measurements. The n_s values obtained here were consistent with previous measurements of n_s values for K-rich feldspar (Atkinson et al., 2013; Harrison et al., 2016; Peckhaus et al., 2016; Whale et al., 2017), and a previously established parametrization for the n_s values of K-rich feldspar (solid line, Fig. 2.2b).

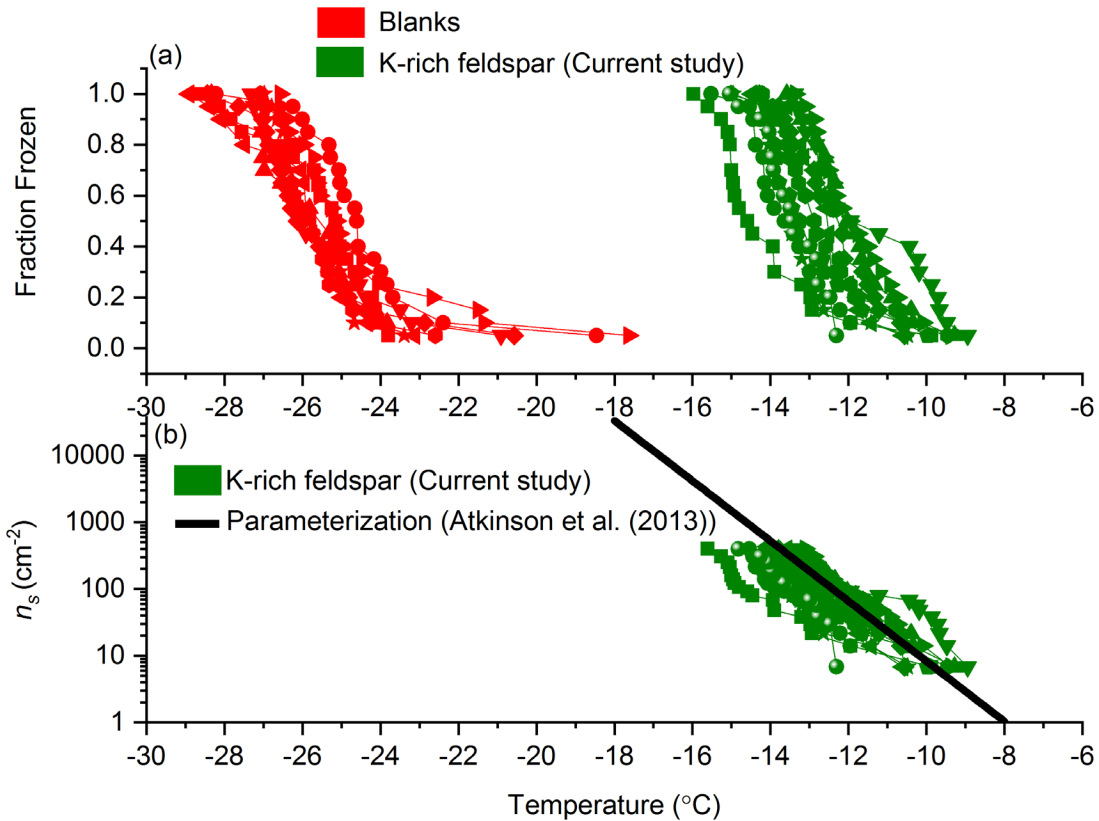


Figure 2.2: Freezing data for pure water droplets only containing K-rich feldspar (0.05 wt%), as well as blanks (pure water droplets): (a) fraction frozen of droplets from multiple trials as a function of temperature and (b) ice nucleating active site density (n_s) as a function of temperature. Different symbols but with the same color represent different trials. For panel (b), the black solid line corresponds to the parameterization of n_s values for K-rich feldspar from Atkinson et al. (2013).

The variability shown in Fig. 2.2a-b (variability of up to 2.5 °C in the median freezing temperatures) is likely due, at least in part, to the limited statistics in the freezing experiments (20 freezing events for one trial) and the variability in the properties of the K-rich feldspar suspensions, which were produced on a daily basis. The variability in the freezing curves is less if data from the same suspension are compared (Appendix B, Fig. B.1).

2.3.2 Ice nucleating ability of K-rich feldspar in alkali metal nitrate solutions

To illustrate the effects of solutes on the freezing properties of K-rich feldspar, we focused on the change in the median freezing temperature (ΔT_{50}) of the droplets due to the presence of solutes, which was calculated with the following equation:

$$\Delta T_{50} = T_{50,solute} - T_{50,H_2O} \quad (2.3)$$

where T_{50,H_2O} is the median freezing temperature of pure water droplets containing K-rich feldspar, and $T_{50,solute}$ is the median freezing temperature of water droplets containing K-rich feldspar and solutes. When calculating ΔT_{50} values, we only used T_{50,H_2O} and $T_{50,solute}$ values measured on the same day to avoid the variability of freezing temperatures for different K-feldspar suspensions. As mentioned above, the variability of the median freezing temperatures from day-to-day is greater than the variability in the median freezing temperature within the same day (compare Fig. 2.2a and Fig. B.1 in Appendix B), likely due to small variations in the properties of the K-rich feldspar suspensions produced on a daily basis.

Fig. 2.3 shows the ΔT_{50} values as a function of concentration for the solutes studied. For all the concentrations investigated, K^+ led to an increase in ΔT_{50} , while the other alkali metal cations led to either no change or a decrease in ΔT_{50} . For Na^+ , Rb^+ , and Cs^+ , as the concentrations increased, the average ΔT_{50} decreased. The largest ΔT_{50} values were observed at the concentration of 5×10^{-3} M. At these concentrations, ΔT_{50} ranged from approximately -7 to 1 °C, representing a variability of approximately 8 °C in the freezing temperatures. At the concentration of 5×10^{-5} M, the effects of cations were weakest, and ΔT_{50} values ranged from approximately -2 to 0.5 °C. The ΔT_{50} values had the following order: $K^+ \geq Li^+ \geq Na^+ \geq Rb^+ \geq Cs^+$.

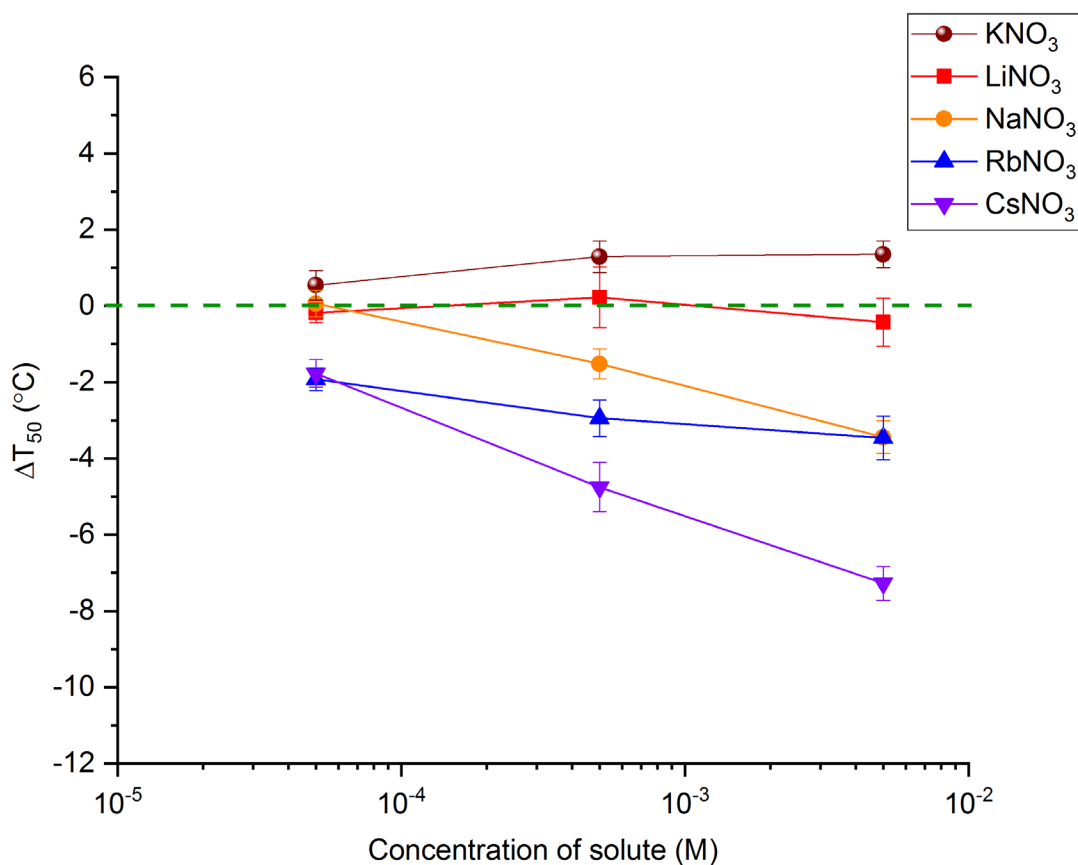


Figure 2.3: ΔT_{50} of aqueous droplets containing K-rich feldspar as a function of nitrate concentration. ΔT_{50} represents the difference of T_{50} (temperature where 50% droplets froze) between droplets containing K-rich feldspar and nitrates and droplets containing K-rich feldspar with no solutes. The type of nitrate is indicated on the right of the figure. Error bars represent the uncertainty of the temperature measurements (i.e., 0.25 °C) and 95 % confidence intervals based on the Student's *t*-distribution. The olive dashed line indicates the position where ΔT_{50} is 0.

2.3.3 Comparison with previous studies that investigated the effects of K⁺ and Na⁺ on the ice nucleating ability of K-rich feldspar.

In Fig. 2.4a, our results for K⁺ are compared with previous studies that have investigated the effect of K⁺ on the ice nucleating ability of K-rich feldspar (Kumar et al., 2018; Whale et al.,

2018; Perkins et al., 2020). The concentration range of K^+ explored in Kumar et al. (2018) and Perkins et al. (2020) overlapped with the concentration range used in the current study, so discrepancies between our results and their results cannot be explained by differences in concentrations. Possible explanations for the apparent discrepancies between our results and theirs include the following: 1) differences in anion type used in the experiments, 2) differences in freezing temperature range investigated, and 3) differences in the sources of K-rich feldspar powder used. Differences in freezing temperature range investigated can lead to different types of ice nucleating sites investigated. The temperature ranges investigated by us, Kumar et al. (2018), and Perkins et al. (2020) were $-20\text{ }^{\circ}\text{C}$ to $-6\text{ }^{\circ}\text{C}$, $-38\text{ }^{\circ}\text{C}$ to $-16\text{ }^{\circ}\text{C}$, and $-15\text{ }^{\circ}\text{C}$ to $-5\text{ }^{\circ}\text{C}$, respectively. Differences in the sources of K-rich feldspars can lead to different compositions and micro-textures of the samples. Micro-texture in addition to composition can be important for the ice nucleating ability of feldspars (Whale et al., 2017).

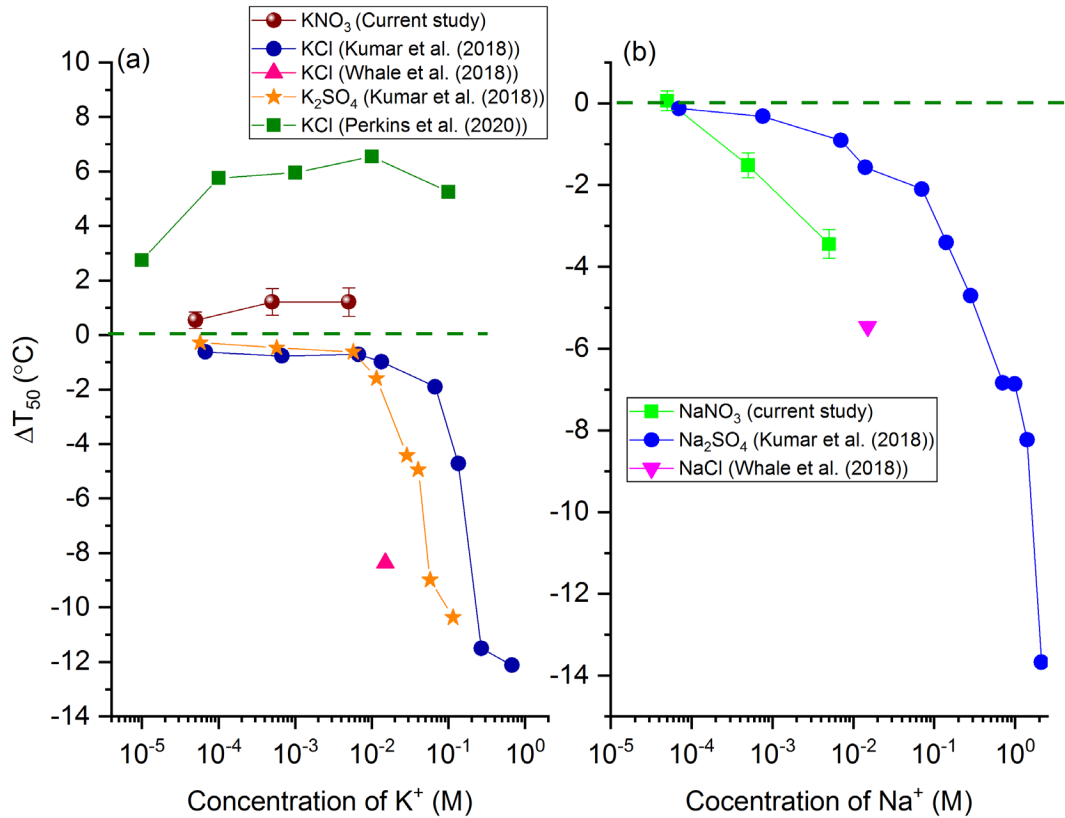


Figure 2.4: ΔT_{50} as a function of concentration of K^+ (panel (a)) and Na^+ (panel (b)) from the current study and a comparison with results reported in the literature. Neither Kumar et al. (2018) nor Perkins et al. (2020) reported median freezing temperatures or ΔT_{50} . The data from Kumar et al. (2018) represents the change in the onset freezing temperatures as a function of concentration of K^+ and Na^+ , since these authors only reported the changes in onset heterogeneous freezing temperatures. The data from Perkins et al. (2020) represents the change in freezing temperatures at an INP concentration of 10^4 per gram of their K-rich feldspar sample. We chose to evaluate the change in freezing temperatures at an INP concentration of 10^4 per gram of their K-rich feldspar sample because their freezing temperatures at this INP concentration for K-rich feldspar suspensions without solutes were similar to our results. The error bars represent the uncertainty of temperature measurements (i.e., 0.25 °C) and 95 % confidence intervals based on the Student's t-distribution. The olive dashed line indicates the position where ΔT_{50} is 0.

To explore the effect of anion type (possible explanation 1), in a separate series of measurements, we compared the freezing temperatures of droplets containing K-rich feldspar and the following potassium salts: KNO_3 , KCl , KBr , and K_2SO_4 (Fig. 2.5). These measurements show that the freezing temperatures do not depend strongly on the anion type when using K^+ with concentration of 5×10^{-3} M.

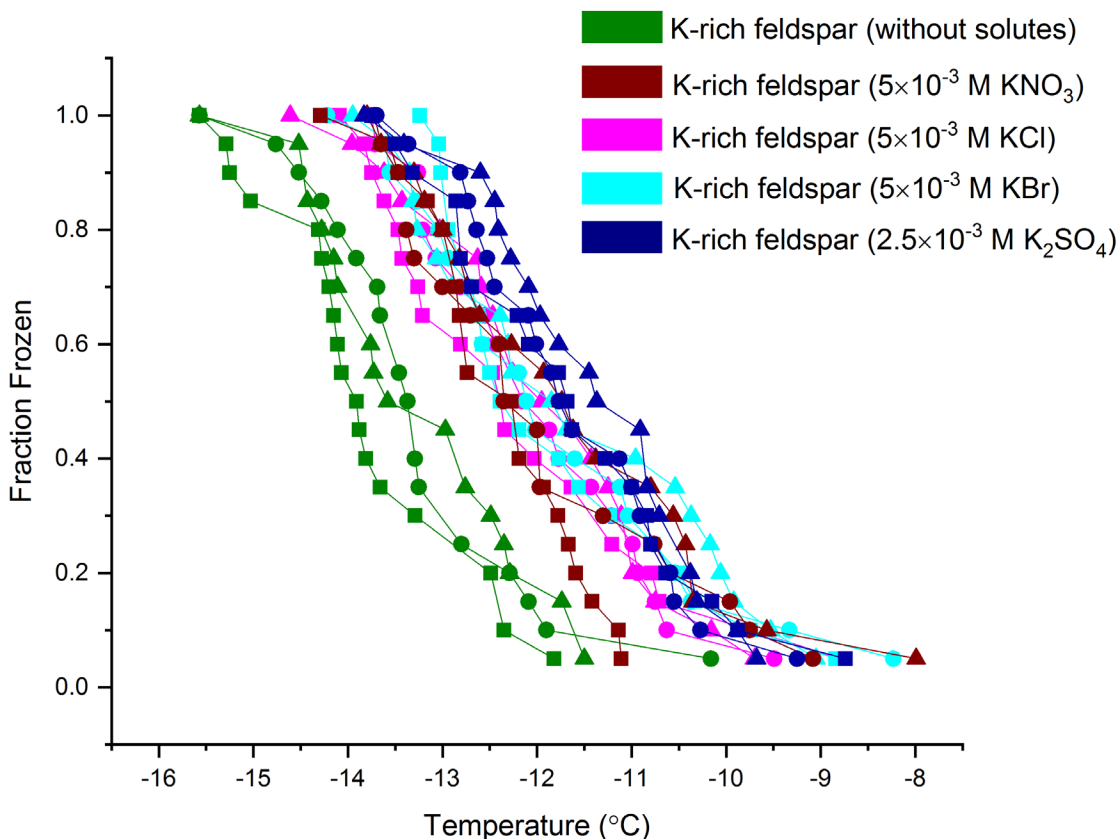


Figure 2.5: Fraction frozen of droplets containing K-feldspar (0.05 wt %) without solutes and droplets containing K-feldspar (0.05 wt %) with potassium salts. The potassium salts used were KNO_3 (5×10^{-3} M), KCl (5×10^{-3} M), KBr (5×10^{-3} M), and K_2SO_4 (2.5×10^{-3} M).

To explore the effect of freezing temperature range (possible explanation 2), we compared the temperature-dependent freezing spectra of droplets containing K-rich feldspar with and without

KNO₃ (Fig. 2.6). These results illustrate that K⁺ (5×10^{-3} M) increases the ice nucleation ability of K-rich feldspar in our experiments at freezing temperatures between -14 and -11 °C. However, at the freezing temperature of approximately -15 °C, K⁺ appeared to have a smaller effect on the ice nucleation ability or even decreased the ice nucleation ability of K-rich feldspar. We conclude that a plausible explanation for the discrepancy between our results and the results from Kumar et al. (2018) shown in Fig. 2.4a is differences in the freezing temperature ranges explored.

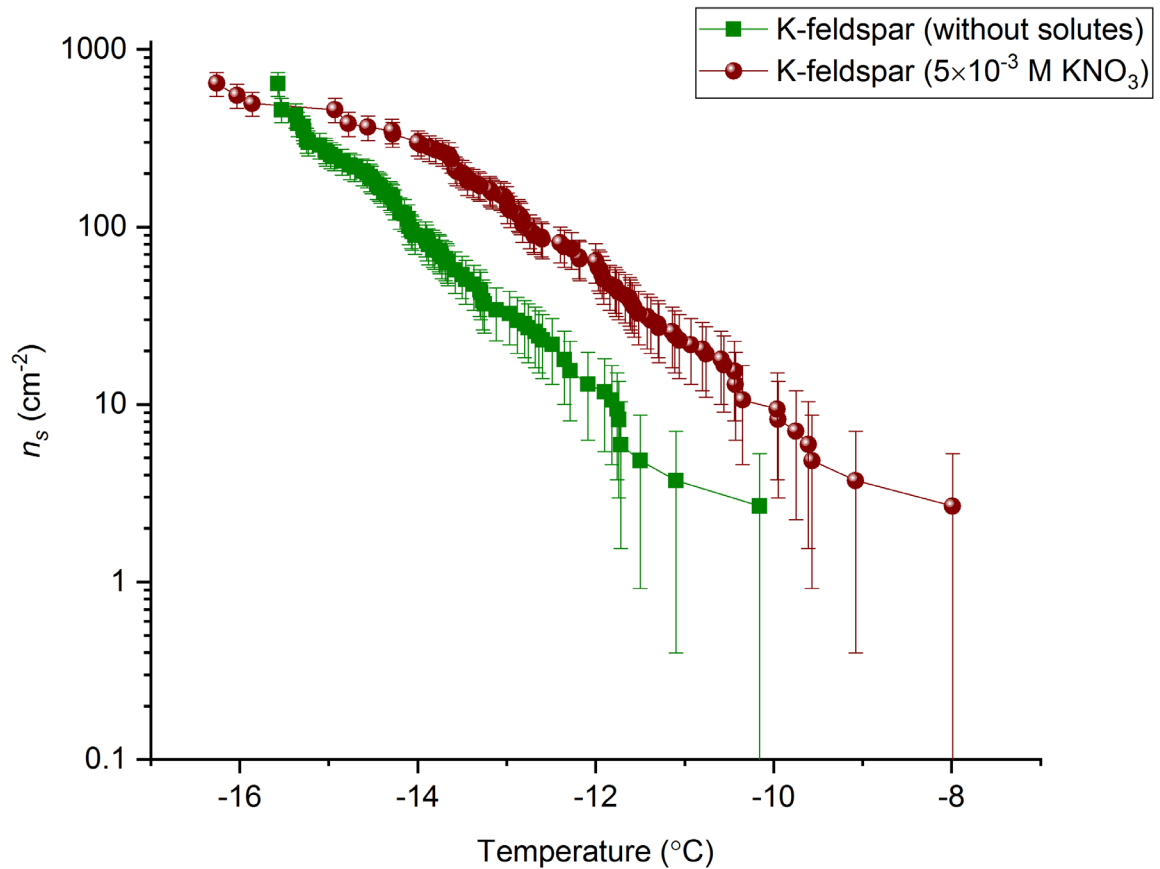


Figure 2.6: Temperature-dependant freezing spectrum of droplets containing K-rich feldspar with and without KNO_3 (5×10^{-3} M). The freezing data for K-rich feldspar in pure water and KNO_3 solutions were obtained by combining the freezing data from six trials (i.e. each freezing spectrum corresponds to 120 droplets). Ice nucleating active site density (n_s) values as a function of temperature were calculated using Eq. 2.2 from the main text. The error bars correspond to 95 % confidence intervals based on the nucleation statistics from Koop et al. (1997).

The discrepancies between our results and Perkins et al. (2020) cannot be explained by the freezing temperature range since similar ranges were used in both experiments. Hence, we are left with differences in the sources of K-rich feldspars as possible explanation for the discrepancies.

Fig. 2.4a, suggests that ΔT_{50} can decrease dramatically when K^+ concentrations exceed 10^{-2} M. To explore this further, we measured the freezing temperature of droplets containing K-rich feldspar and 5×10^{-2} M KNO_3 (Fig. 2.7). Consistent with previous studies, we observed a decrease in the ice nucleation ability of K-rich feldspar when K^+ concentrations exceeded 10^{-2} M.

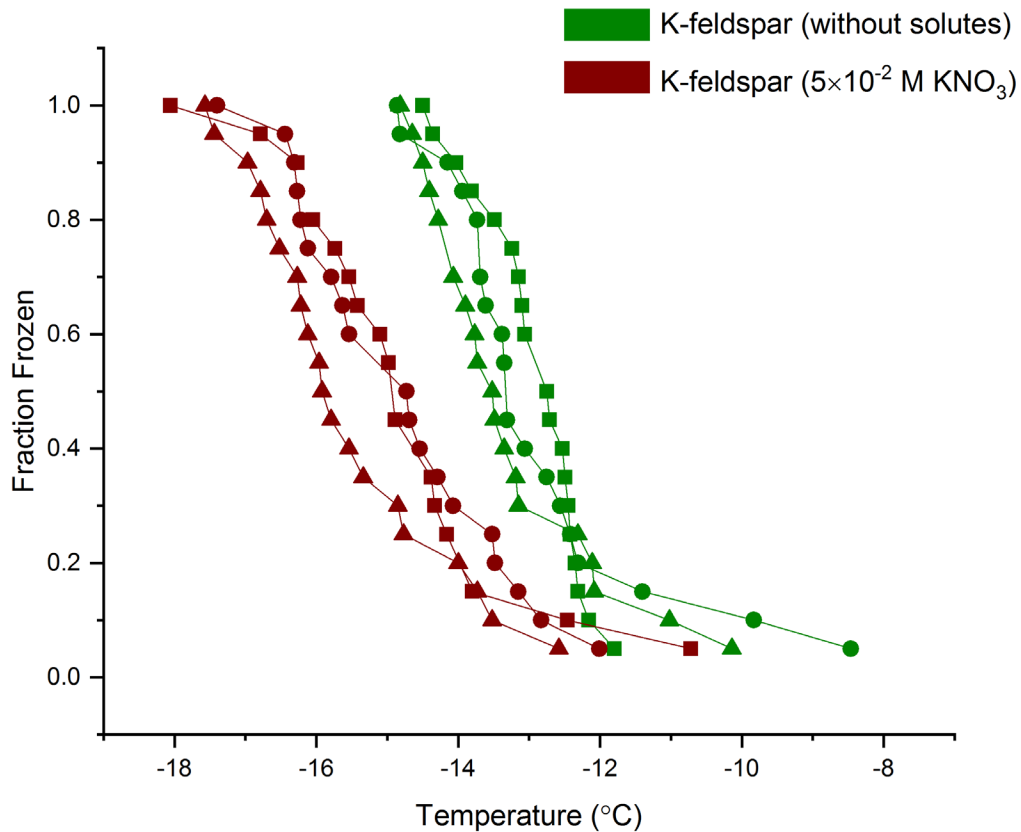


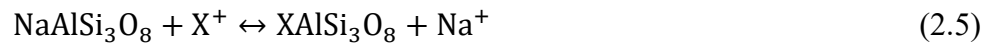
Figure 2.7: Comparison of the freezing spectrum for droplets containing only K-rich feldspar (0.05 wt %) without solutes and droplets containing K-rich feldspar (0.05 wt %) and KNO_3 (5×10^{-2} M). The freezing temperature of the droplets containing K-rich feldspar and KNO_3 has been corrected for freezing point depression using Eq. 2.1 from the main text.

Two previous studies also investigated the effect of Na^+ on the ice nucleating ability of K-rich feldspar (Kumar et al., 2018; Whale et al., 2018) (Fig. 2.4b). Both of the studies observed a

decrease in the ice nucleating ability of K-rich feldspar when exposed to Na^+ , consistent with the current results, although our results are quantitatively different than Kumar et al. (2018). Possible reasons for this apparent difference are discussed above.

2.3.4 The relative abundance of atoms at K-rich feldspar surfaces before and after the exposure to alkali nitrate solutions

As mentioned above, the K-rich feldspar sample we studied contained 85% microcline (KAlSi_3O_8) and 15% albite ($\text{NaAlSi}_3\text{O}_8$). The crystal structures of microcline and albite are very similar, but not identical (Appendix B, Table B.2). Microcline and albite are composed of AlO_4^- and SiO_4 tetrahedral groups linked in 3 dimensions, with K^+ (for microcline) and Na^+ (for albite) compensating the negative charge due to AlO_4^- in the crystal lattice. Ion exchange can occur between foreign cations from aqueous solutions and parent K^+ at microcline surfaces and parent Na^+ at albite surfaces (Nash and Marshall, 1957; Gülgönül et al., 2012). This ion exchange can be represented by Eq. 2.4 and 2.5 for microcline and albite, respectively (Stumm and Morgan, 1981):



where X^+ represents the foreign cations in the aqueous solutions including alkali cations and H_3O^+ . This ion exchange likely occurs first at defects, edges, or corners of the mineral crystal, since the cations will be less tightly held at these locations. In addition to ion exchange, the alkali metal cations can be absorbed to the K-rich feldspar surfaces. In our experiments, the surface of K-rich feldspar was negatively charged since the pH of the solutions (~ 6) was above the point of zero charge of K-rich feldspar ($\sim 1-2$) (Kosmulski, 2009). Therefore, cations were more likely to interact with the negatively charged K-rich feldspar surfaces than anions in our experiments.

Cryo-XPS was used to measure ion exchange and adsorption at the K-rich feldspar surfaces (Fig. 2.8). For the dry powder of K-rich feldspar, the average K/Al and Na/Al ratios were 0.93 and 0.17, respectively, which is roughly consistent with the composition of our K-rich feldspar samples (85 % microcline and 15 % albite). Upon exposure to pure water, average K/Al and Na/Al values decreased slightly, indicating a small amount of ion exchange between parent K^+ in microcline and parent Na^+ in albite with H_3O^+ in pure water (Eq. 2.4 and 2.5). This small amount of ion exchange is consistent with previous measurements that quantified ion-exchange in K-rich feldspar when exposed to water at near-neutral pH conditions. For example, Peckhaus et al. (2016) and Gülgönül et al. (2012) quantified the release of K^+ from K-rich feldspar when exposed to water, and based on their measurements, the depth of full exchange of K^+ when exposed to water is approximately 21% and 49% respectively of the top unit cell in K-rich feldspar (Appendix B, Section B.2). In addition, a previous study that combined molecular simulations and surface spectroscopy is consistent with only partial exchange of K^+ with H_3O^+ when K-rich feldspar is exposed to water (Kerisit et al., 2008).

When exposed to KNO_3 solutions, the average K/Al ratio increased slightly while the average Na/Al ratio decreased slightly compared to pure water conditions, which is consistent with the replacement of parent Na^+ in albite with K^+ from solution (Eq. 2.5) and a decrease in ion exchange between parent K^+ in microcline and H_3O^+ in water (Eq. 2.4). For $NaNO_3$ solutions, the average K/Al ratio decreased while the average Na/Al ratio increased compared to pure water conditions, consistent with parent K^+ of microcline being partially replaced by the Na^+ from solutions (Eq. 2.4) and a decrease in ion exchange between parent Na^+ in albite and H_3O^+ in water (Eq. 2.5). When K-rich feldspar was exposed to other alkali nitrate solutions ($LiNO_3$, $RbNO_3$, or $CsNO_3$), the average K/Al and Na/Al ratios both decreased compared to pure water conditions,

while the average Li/Al, Rb/Al, or Cs/Al ratio increased, consistent with parent K^+ in microcline and parent Na^+ in albite being replaced by the foreign cations (Li^+ , Rb^+ , or Cs^+) from solutions (Eq. 2.4 and 2.5). In some cases (e.g., $LiNO_3$, $NaNO_3$, and $CsNO_3$), the average $(Li+Na+K+Rb+Cs)/Al$ ratio (i.e., the total alkali metal cation ratio) was greater than the dry powder case, suggesting that ion adsorption, in addition to ion exchange, was significant in some experiments.

The smallest K/Al ratio observed in our experiments was ~ 0.6 (Rb^+ results in Fig. 2.8). As mentioned earlier, the analysis depth of the cryo-XPS measurements was 5-6 nm. If we assume the samples were bare (i.e. not coated with ice) in the cryo-XPS measurements and the intensity of the XPS signal was independent of depth over the entire analysis depth, an K/Al ratio of 0.6 corresponds to full depletion of K^+ from the top 2-2.4 unit cells in the K-rich Feldspar samples. However, full depletion from the top 2-2.4 unit cells should be considered as an upper limit for the following reasons: 1) in cryo-XPS measurements mineral surfaces are covered with a layer of ice ~ 1 nm thick, suggesting the depth of the K-rich Feldspar samples analyzed was $\sim 4-5$ nm, rather than 5-6 nm (Shchukarev and Ramstedt, 2017); 2) The intensity of the XPS signal has an exponential dependence on depth, resulting in the top 1/3 of the analysis depth contributing $> 50\%$ of the overall XPS signal.

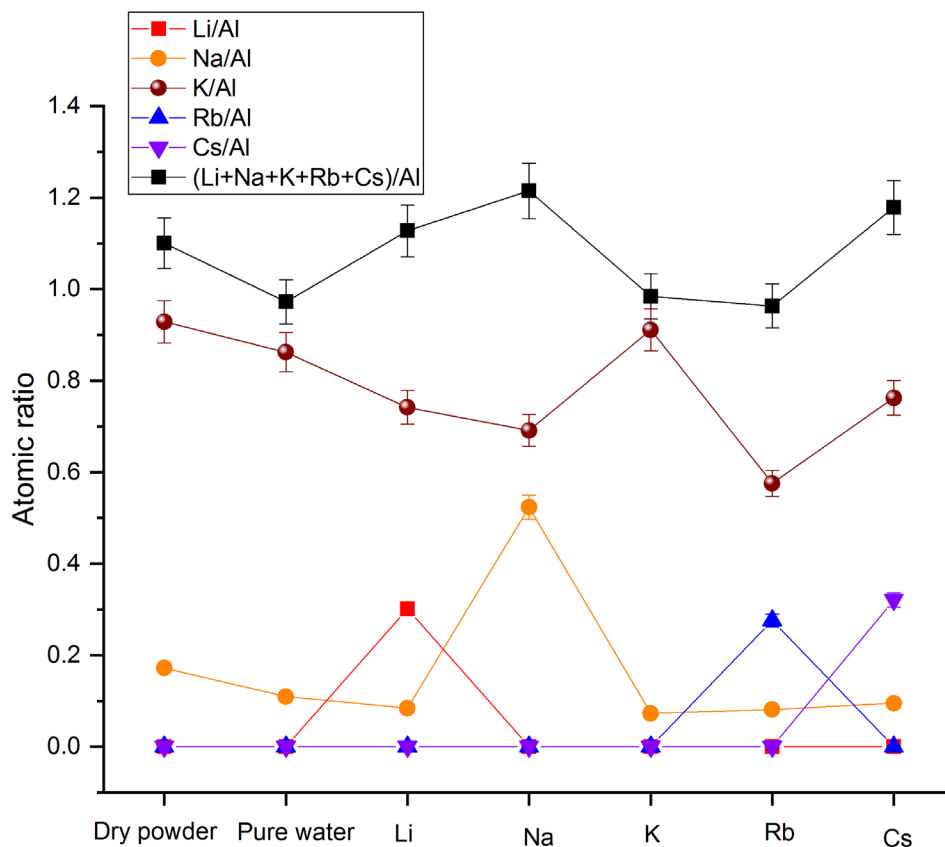


Figure 2.8: Results obtained from cryo-XPS measurements: the atomic ratio Li/Al, Na/Al, K/Al, Rb/Al, Cs/Al and (Li+Na+K+Rb+Cs)/Al for dry powder of K-rich feldspar and K-rich feldspar particles exposed to pure water and alkali nitrate solutions (5×10^{-3} M). The error bars of the atomic ratio are the uncertainty of cryo-XPS measurements (5%) which is obtained from repeating 3 trials for the same experimental conditions.

2.3.5 The effect of K^+ on the ice nucleating ability of K-rich feldspar

What is especially striking about the freezing results shown in Fig. 2.3 is that the presence of KNO_3 as a solute led to an increase in ΔT_{50} , while the other alkali metal cations led to either no change or a decrease in ΔT_{50} . As mentioned earlier, the structures of microcline and albite are very similar (Appendix B, Table B.2), except for the different charge balancing cations (K^+ for microcline and Na^+ for albite). Previous studies have shown that, in general, microcline is a better

ice nucleus than albite (Atkinson et al., 2013; Zolles et al., 2015; Harrison et al., 2016; Peckhaus et al., 2016; Whale et al., 2017). Related, a recent study suggested that the superior ice nucleating ability of microcline samples compared to albite samples may be related to the micro-texture of the samples (Whale et al., 2017). Based on the studies that showed microcline is a better ice nucleus than albite, we assume that the microcline component of the K-rich feldspar sample is likely responsible for ice nucleation in our freezing experiments. Based on this assumption and the cryo-XPS data discussed above, a likely explanation for the enhancement of ice nucleating ability of K-rich feldspar after exposure to KNO_3 solutions is a decrease in ion exchange between parent K^+ in microcline and H_3O^+ in water (Eq. 2.4) to form additional K-bearing microcline surfaces (i.e. microcline surfaces containing K^+), followed by ice nucleation on certain types of K-bearing microcline surfaces. Consistent with this explanation, Peckhaus et al. (2016) observed a decrease in the ice nucleating ability of K-rich feldspar coincident with the depletion of framework cations from K-rich feldspar surfaces due to aging in water. Possibly related, ice nucleation active sites on K-rich feldspar identified by Kiselev et al. (2017) likely can undergo ion exchange.

2.3.6 Relation between ΔT_{50} and the atomic ratio K/Al

Based on the discussion above, we tested the ability of the K/Al ratio determined from cryo-XPS to predict ΔT_{50} , as shown in Fig. 2.9. The correlation coefficient between ΔT_{50} and the K/Al ratio for all the alkali nitrates was moderate and not statistically significant ($R=0.55$ and $p=0.13$; dashed red line in Fig. 2.9), suggesting that the K/Al ratio is not the only parameter controlling ΔT_{50} in our experiments. After excluding Cs^+ from the correlation, a strong and statistically significant correlation was observed ($R=0.92$ and $p=0.005$; solid black line in Fig. 2.9). This stronger correlation possibly suggests that the K/Al ratio is an indicator of the abundance of certain types of K-bearing microcline surfaces that best host ice nucleation for our experimental

conditions. Cs^+ does not fit this correlation. Cs^+ caused a decrease in the freezing temperature of $\sim 7^\circ\text{C}$, much more than expected based on the correlation between ΔT_{50} and K/Al when Cs^+ was excluded from the correlation. Of all the cations studied, Cs^+ has the largest atomic radius, and perhaps this larger radius is related to why Cs^+ does not follow the same trend as the other cations and why it has a much larger effect on the freezing temperature than expected based on the K/Al ratio. One possibility is that Cs^+ decreased the ice nucleation ability by adsorbing to ice nucleating active sites in addition to ion exchange with parent K^+ in microcline.

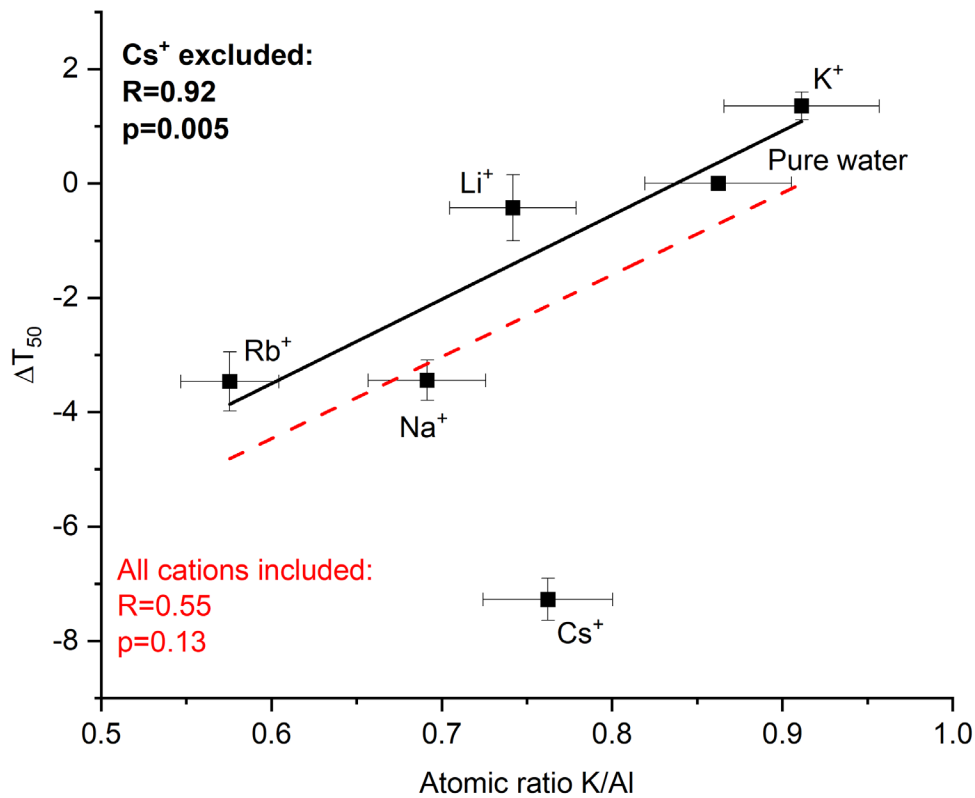


Figure 2.9: ΔT_{50} for alkali cations at the concentration of 5×10^{-3} M as a function of the atomic ratio K/Al at the surfaces of K-rich feldspar particles exposed to alkali nitrate solutions. Two correlations correspond to cases: 1) all the cations included (red dashed line); 2) cations excluding Cs⁺ (black solid line). The correlation coefficient R and the p-value for each correlation are indicated in the plot. The error bars for ΔT_{50} represent the uncertainty of temperature measurements (i.e., 0.25 °C) and 95 % confidence intervals based on the Student's t-distribution. The error bars of the atomic ratio are the uncertainty of cryo-XPS measurements (5%) which is obtained from repeating 3 trials for the same condition.

2.3.7 Relation between ΔT_{50} and cation charge density

Previous studies have suggested that cation charge density (charge density over the surface area of a single cation) may be important in the immersion freezing of mineral dust (Zolles et al.,

2015; Boose, Sierau, et al., 2016). In aqueous solutions, cations with higher cation charge density (often referred to as kosmotropes) interact strongly with water, while cations with lower cation charge density (often referred to as chaotropes) interact less strongly with water (Collins, 1997; Zhao, 2006). Strong interactions between water and cations at the surfaces of mineral dust could limit the mobility of water molecules and hinder ice formation while weak interactions between water and cations could make water molecules free to form an ice embryo (Zolles et al., 2015; Boose, Sierau, et al., 2016). To test if the cation charge density was a controlling factor in our ice nucleation experiments, we examined the correlation between ΔT_{50} and cation charge density (Fig. 2.10). The correlations were weak and not statistically significant. In addition, the correlations were positive (i.e., a lower cation charge density correlated with the decrease of ice nucleating ability of K-rich feldspar), which is opposite to the trend expected based on the discussion above. Therefore, we conclude that a low cation charge density is not a good predictor of the enhanced ice nucleating ability in our experiments. An alternative explanation based on the data from our droplet freezing and cryo-XPS experiments is that certain types of K-bearing microcline surfaces have the ideal geometry and optimal interactions with water molecules to facilitate ice nucleation. Any deviations of these surfaces reduce the ice nucleating ability.

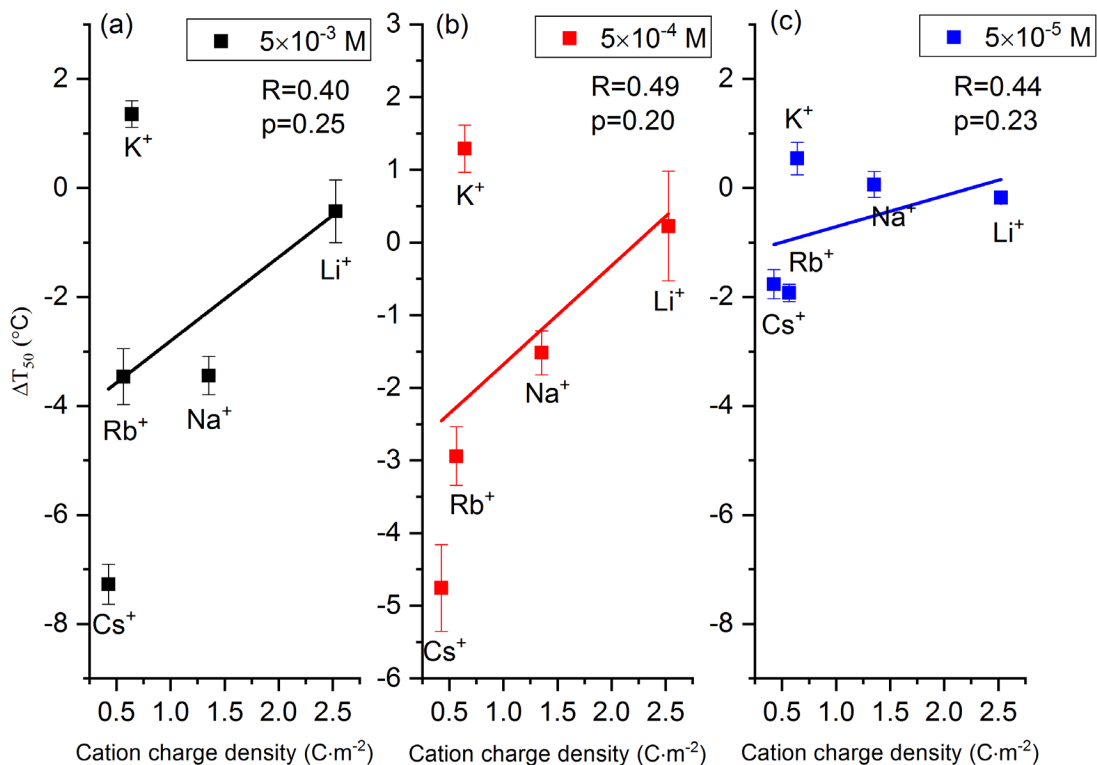


Figure 2.10: ΔT_{50} for alkali cations as a function of their cation charge density (i.e., charge density over the surface area of a single cation) at three concentrations studied: (a) 5×10^{-3} M; (b) 5×10^{-4} M; (c) 5×10^{-5} M. The error bars represent the uncertainty of temperature measurements (i.e., 0.25 °C) and 95 % confidence intervals based on the Student's t-distribution. The correlation coefficient R and p-values are indicated in each panel.

2.4 Conclusions and outlook

In this chapter, we investigated the effects of a series of alkali metal cations (Li⁺, Na⁺, K⁺, Rb⁺, and Cs⁺) at low concentrations ($\leq 5 \times 10^{-3}$ M) on the ice nucleation properties of K-rich feldspar in the immersion freezing mode. Only K⁺ had a positive effect while the other alkali cations had either negative effects or no effects on the ice nucleating ability of K-rich feldspar. Except for Cs⁺, the ice nucleating ability correlated with the atomic ratio K/Al at the K-rich feldspar surfaces after exposure to alkali metal nitrate solutions, possibly suggesting that the K/Al

ratio is an indicator of abundance of K-bearing microcline surfaces (i.e., microcline surfaces containing K^+) and ice nucleation occurs on certain types of K-bearing microcline surfaces for the freezing temperature ranges and concentrations investigated here. Overall, these results highlight the importance of K^+ for ice nucleation by K-rich feldspar. The fact that Cs^+ is an outlier suggests that Cs^+ influences the immersion freezing of K-rich feldspar by an additional mechanism, possibly blocking of ice nucleating sites by adsorption.

Previous studies have suggested that cation charge density (charge density over the surface area of a single cation) may be important in the immersion freezing of mineral dust, (Zolles et al., 2015; Boose, Sierau, et al., 2016) with a lower cation charge density leading to a better ice nucleation ability. However, our results did not support this previous suggestion.

Our results illustrate the importance of solute type on the immersion freezing of droplets containing mineral dust. In the atmosphere, different types of solutes including inorganics and organics can appear in cloud droplets simultaneously (Gioda et al., 2011; Van Pinxteren et al., 2016; Cook et al., 2017). The effects of the mixtures may be non-additive and different from the effects of a single type of solute. Additional studies using mixtures of solutes would be useful.

Chapter 3: Effects of inorganic acids and organic solutes on the ice nucleating ability and surface properties of potassium-rich feldspar

3.1 Introduction

One of the main types of INPs in the atmosphere is mineral dust (Prenni, Petters, et al., 2009; Murray et al., 2012; Cziczo et al., 2013; Boose, Welti, et al., 2016; Tang et al., 2016; Kanji et al., 2017; O’Sullivan et al., 2018; Si et al., 2019). These particles can be coated with inorganic salts, inorganic acids, and water-soluble organic compounds by condensation of gases, coagulation, cloud processing, and heterogeneous reactions (Tinsley et al., 2000; Wurzler et al., 2000; Usher et al., 2003; Falkovich, 2004; Hinz et al., 2005; McNaughton et al., 2009; Ma et al., 2012; He et al., 2014). Solutes can influence the ice nucleating ability of mineral dust immersed in droplets by decreasing water activity and by modifying the surface properties of the mineral dust. Although solutes at low concentrations (e.g. < 0.1 M) have little impact on water activity (Koop et al., 2000; Zobrist et al., 2008; Koop and Zobrist, 2009), solutes at low concentrations can still alter the ice nucleating ability of mineral dust particles by modifying their interfacial properties (Reischel and Vali, 1975; Sullivan, Petters, et al., 2010; Tobo et al., 2012; Wex et al., 2014; Kumar et al., 2018, 2019b, 2019a; Whale et al., 2018; Perkins et al., 2020; Yun et al., 2020).

Numerous studies have shown that inorganic salts at low concentrations can significantly alter the ice nucleating ability of mineral dust in the immersion freezing mode. For example, several studies have shown that sodium salts at low concentrations can significantly decrease the ice nucleating ability of feldspars (Kumar et al., 2018; Whale et al., 2018; Yun et al., 2020), while potassium salts can either enhance or suppress the ice nucleating ability of K-rich feldspar depending on the sources of K-rich feldspar samples, the freezing temperature, and the

concentration of K^+ (Kumar et al., 2018; Whale et al., 2018; Perkins et al., 2020; Yun et al., 2020). Ammonium salts at low concentrations were also found to significantly enhance the ice nucleating ability of several types of aluminosilicates, including feldspars, kaolinite, muscovite, and gibbsite (Reischel and Vali, 1975; Kumar et al., 2018, 2019b; Whale et al., 2018). Lithium iodide was also shown to enhance the ice nucleating ability of kaolinite particles in the immersion freezing mode (Reischel and Vali, 1975), although this enhancement was not observed in a recent study (Ren et al., 2020).

Several studies have also shown that inorganic acids at low concentrations can significantly alter the ice nucleating ability of mineral dust in the immersion freezing mode. For example, Kumar et al. (2018) showed that the ice nucleating ability of K-rich feldspar was lowered by approximately 7 °C after aging K-rich feldspar particles in a NH_4HSO_4 solution (pH = 1.2) for 10 days. Burkert-Kohn et al. (2017) also observed a strong reduction in the ice nucleating ability of K-rich feldspar in the immersion freezing mode after exposure to 1 M HNO_3 and H_2SO_4 for 12 h followed by washing to remove the acids. Abdelmonem et al. (2017) showed that immersion freezing by sapphire surfaces was suppressed after exposing the surfaces to HNO_3 solutions (pH = 3 and 4), and they attributed the decrease in ice nucleating ability to the modification of the surface charge caused by the change of pH. Several studies also showed that immersion freezing by several types of mineral dust particles (kaolinite, K-rich feldspar, Arizona Test Dust) was suppressed after the particles were coated with sulfuric acid (Sullivan, Petters, et al., 2010; Tobo et al., 2012; Augustin-Bauditz et al., 2014; Wex et al., 2014). In contrast to these results, Sullivan and Miñambres et al. (2010) did not observe a significant reduction in the immersion freezing of Arizona Test Dust (ATD) particles after exposing the particles to HNO_3 vapors. Similarly, Link et

al. (2020) reported no significant suppression in the immersion freezing of ATD particles after exposure to HCl solutions (pH = 1 and pH = 3) for up to 14 days.

A few studies have also investigated the effects of organic solutes at low concentrations on the ice nucleating ability of mineral dust particles in the immersion freezing mode. Zobrist et al. (2008) and Koop and Zobrist (2009) showed that the presence of polyethylene glycol at low concentrations did not significantly reduce the ice nucleating ability of ATD. Tobo et al. (2012) and Wex et al. (2014) showed that levoglucosan coatings did not significantly influence the ice nucleating ability of kaolinite particles in the immersion freezing mode. In addition, Kanji et al. (2019) showed that secondary organic aerosol (SOA) coatings from the dark ozonolysis of α -pinene did not influence the ice nucleating ability of natural mineral dust particles in the immersion freezing mode.

Despite the studies mentioned above, our understanding of the effects of inorganic acids and organic solutes at low concentrations on the ice nucleating ability of mineral dust remains incomplete. Additional studies are needed to relate the actual composition of mineral surfaces to their ice nucleating ability. In addition, studies are needed to better understand the effect of organic acids on the ice nucleating ability of mineral dust particles, since organic acids are abundant in atmospheric aerosols (Saxena and Hildemann, 1996; Decesari et al., 2000; Fuzzi et al., 2001; Hawkins et al., 2010). In particular, a focus on K-rich feldspar is needed as it is a more effective ice nucleus than other types of mineral dust (Atkinson et al., 2013; Zolles et al., 2015; Harrison et al., 2016; Peckhaus et al., 2016; Kiselev et al., 2017), and it has been used in climate models to predict atmospheric INP concentrations (Atkinson et al., 2013; Vergara-Temprado et al., 2017).

In this chapter, we first investigated the impact of 10^{-5} to 10^{-1} M solutions of HNO₃ and HCl on the ice nucleating ability of K-rich feldspar in the immersion freezing mode. HNO₃ and

HCl are two common inorganic acids in the atmosphere resulting from industrial, marine, and volcanic sources (Eldering et al., 1991; Seinfeld and Pandis, 2006). By comparing the results for these two inorganic acids, we were able to isolate the effect of H^+ on the freezing properties of K-rich feldspar. The ice nucleation measurements were supported by measurements of the composition of K-rich feldspar surfaces exposed to different concentrations of HCl solutions, using cryo-XPS.

We also investigated the effects of carboxylic acids and polyols on the immersion freezing of K-rich feldspar. The concentration of the organic solutes used ranged from 3×10^{-5} M to 3×10^{-3} M, which is relevant for mixed phase clouds (Reischel and Vali, 1975). Carboxylic acids and polyols were chosen as solutes because they make up a large fraction of water-soluble organic compounds in the atmosphere (Saxena and Hildemann, 1996; Decesari et al., 2000; Fuzzi et al., 2001; Hawkins et al., 2010). The specific organics studied and relevant properties are listed in Table 3.1, and their structures are included in Table C.1 and Table C.2 (Appendix C). All of the organic solutes studied have been detected in atmospheric aerosols (Decesari et al., 2000; Graham et al., 2002; Hawkins et al., 2010; Jung and Kawamura, 2011; Lei et al., 2014).

Table 3.1: Organic molecules studied and their relevant properties.

Compounds	Formula	Molecular Weight	O:C ratio	Types and number of functional groups	
Levoglucosan	C ₆ H ₁₀ O ₅	162	0.83	Alcohol (3)	
Glycerol	C ₃ H ₈ O ₃	92	1	Alcohol (3)	
Glucuronic acid	C ₆ H ₁₀ O ₇	194	1.17	Alcohol (4), carboxyl (1)	
Citric acid	C ₆ H ₈ O ₇	192	1.17	Alcohol (1), carboxyl (3)	
Azelaic acid	C ₉ H ₁₆ O ₄	188	0.44	Carboxyl (2)	
Oxalic acid	C ₂ H ₂ O ₄	90	2	Carboxyl (2)	
Acetic acid	C ₂ H ₄ O ₂	60	1	Carboxyl (1)	
Phthalic acid	C ₈ H ₆ O ₄	166	0.5	Carboxyl (2)	
M5 ^a	Malic acid	C ₄ H ₆ O ₅	134	1.25	Alcohol (1), carboxyl (2)
	Malonic acid	C ₃ H ₄ O ₄	104	1.33	Carboxyl (2)
	Maleic acid	C ₄ H ₄ O ₄	116	1	Carboxyl (2)
	Glutaric acid	C ₅ H ₈ O ₄	132	0.8	Carboxyl (2)
	Methylsuccinic acid	C ₅ H ₈ O ₄	132	0.8	Carboxyl (2)

^aM5 refers to a mixture of malic acid, malonic acid, maleic acid, glutaric acid, and methysuccinic acid (Marcolli et al., 2004). Mass ratios of 5:8:2:4:1 for malic acid : malonic acid : maleic acid : glutaric acid : methylsuccinic acid were used following Primm et al. (2017).

3.2 Experimental

3.2.1 Chemicals

The K-rich feldspar powder was ground from a K-rich feldspar rock provided by the Pacific Museum of Earth, University of British Columbia. The same K-rich feldspar powder was used in the study described in Chapter 2 (Yun et al., 2020). The BET specific surface area of K-rich feldspar particles was $0.75 \text{ m}^2/\text{g}$, and the composition of K-rich feldspar powder was 85% microcline and 15% albite, confirmed by XRD with Rietveld modelling (Rietveld, 1969).

The following are the inorganic acids and organic solutes (as well as vendors and purities of the chemicals) used in the current study: levoglucosan (Sigma-Aldrich, 99%), citric acid (Sigma-Aldrich, 99%), glucuronic acid (Sigma-Aldrich, $\geq 98\%$), azelaic acid (Fluka, $\geq 99\%$), oxalic acid (Fisher Scientific, certified A.C.S), acetic acid (Sigma-Aldrich, $\geq 99\%$), phthalic acid (Sigma-Aldrich, $> 99.5\%$), malic acid (Sigma-Aldrich $> 99\%$), malonic acid (Fluka, $\geq 99\%$), maleic acid (Sigma-Aldrich, $\geq 99\%$), glutaric acid (Sigma-Aldrich, 99%), methylsuccinic acid (Sigma-Aldrich, 99%), nitric acid (J.T. Baker, A.C.S. Reagent), and hydrochloric acid (Alfa Aesar, Environmental grade).

All of the solutions and suspensions were prepared with Milli-Q water in polypropylene tubes (Falcon, Fisher Scientific). The pH of the carboxylic acid and inorganic acid solutions was determined with a pH glass electrode (accuTupH, Fisher Scientific) and a pH meter (Beckman 350). Based on information from the manufacturer, the uncertainty of pH measurements was 0.01 unit.

3.2.2 Droplet freezing technique

The freezing temperature of droplets containing K-feldspar with or without solutes was determined using the droplet freezing technique, which is described in detail in Chapter 2 and other studies (Whale et al., 2015; Irish et al., 2017; Irish, Hanna, Willis, et al., 2019; Yun et al., 2020). For each trial, a hydrophobic siliconized slide (Hampton Research) was placed on a cold plate (Grant Aymptote EF600), and then 1- μ L droplets of a K-rich feldspar suspension in water (0.1 wt % K-rich feldspar) were pipetted onto the hydrophobic slide. The K-rich feldspar suspension was always made the day before the freezing experiments and stirred overnight. After generating the initial 1- μ L droplets, a second set of 1- μ L droplets containing the solutes or just pure water were pipetted onto the previously made droplets. This produced 2- μ L droplets containing K-rich feldspar (0.05 wt %) with or without solutes. A total of 20 droplets was generated for each trial. Three replicates were performed for each experimental condition, which allowed us to assess the variability in the freezing temperatures from trial to trial. The three replicates were also used to determine the uncertainty (95 % confidence intervals) of the change in median freezing temperature caused by the solutes.

A transparent chamber was placed over the slides to isolate the droplets from ambient air. The temperature of the cold plate was then decreased at a rate of 3 °C per minute from 0 °C until all the droplets froze. Freezing of the droplets was captured by a digital camera located at the top of the transparent chamber. The recorded video was analyzed either manually or automatically by a MATLAB script to determine the freezing temperature of each droplet (Xi et al., 2021). The interaction time of the K-rich feldspar with the solute was 10-15 minutes before freezing, which is sufficient to ensure full mixing in the droplets, as detailed further in Section C.1 of Appendix C.

The uncertainty in temperature measurements was 0.25 °C according to the manufacturer, which was verified by measuring melting temperatures of water and dodecane and comparing the measurements with melting temperatures reported in the literature. Freezing point depression caused by the solutes was estimated using Eq. 2.1 from Chapter 2. For cases where the organics were used as solutes, the concentrations of organics ranged from 5.2×10^{-5} M to 2.6×10^{-3} M. We assumed a van't Hoff factor of 1. Based on Eq. 2.1, the largest freezing point depression was 0.005 °C when the concentration of organics was 2.6×10^{-3} M.

For cases where HNO₃ or HCl was used as the solute, the concentration of HNO₃ or HCl ranged from 1×10^{-5} M to 5×10^{-2} M resulting in a pH from 1.5 to 5. We assumed a van't Hoff factor of 2. Based on Eq. 2.1, the largest freezing point depression was 0.186 °C when the concentration of HNO₃ was 0.05 M. All the freezing temperatures reported here have been corrected for the freezing point depression.

From the fraction of the frozen droplets, the ice nucleating active site density (n_s) was calculated using Eq. 2.2 from Chapter 2. For the freezing experiments, 2- μ L droplets of Milli-Q water were used as blanks. The uncertainty in n_s (95% confidence intervals) was calculated with the nucleation statistics from Koop et al. (1997). When calculating the final n_s values for the samples, average n_s values of the blanks were subtracted from original n_s values of the samples. The average n_s values for the blanks were calculated using Eq. 2.2 from Chapter 2 and by assuming the surface area in droplets of the blanks was the same as the surface area in droplets of the samples.

3.2.3 Cryo-XPS measurements of K-rich feldspar surfaces exposed to HCl solutions

The elemental composition of K-rich feldspar surfaces before and after exposure to HCl solutions was determined by cryo-XPS (Shchukarev and Ramstedt, 2017). Briefly, a K-rich feldspar suspension (0.05 wt %) in a HCl solution or pure water was mixed for approximately 15 minutes, and then centrifuged for 10 minutes at 5000 rpm. The supernatant was thereafter decanted to obtain a wet paste with a high solid-to-water ratio. The wet paste was then loaded onto a sample holder and frozen within ~45 seconds at a temperature of -170 °C and pressure of $\sim 5 \times 10^{-5}$ Pa. It was then transferred into the analytical chamber, at -155 °C and 2×10^{-7} Pa, where the XPS spectra were collected with the Kratos Axis Ultra DLD electron spectrometer. Kratos software was used to analyze the XPS spectra and to calculate the elemental composition of the K-rich feldspar surfaces.

For our experimental conditions, the sampling depth was approximately 5-6 nm. Due to the method of preparing the samples, a thin layer of ice (~1 nm thick) was expected to cover the K-rich feldspar surface prior to the cryo-XPS measurements (Shchukarev and Ramstedt, 2017). As a result, the depth of the K-rich feldspar surfaces analyzed in our experiments is expected to be approximately 4-5 nm. Based on a previous triplicate analysis of the K-rich feldspar surfaces under the same experimental conditions (Yun et al., 2020), we used error bars of $\pm 5\%$ in our reported atomic ratios, which corresponds to two standard deviations of the 3 replicates.

3.3 Results and Discussion

3.3.1 The effects of inorganic acids at low concentrations on the immersion freezing of K-rich feldspar

Shown in Fig. 3.1 and 3.2 are freezing data for the K-rich feldspar exposed to different concentrations of HNO₃ and HCl. Median freezing temperatures of the droplets containing K-rich

feldspar were approximately 4 to 12 °C warmer than median freezing temperatures of the droplets of Milli-Q water (i.e., blanks). HNO₃ or HCl decreased median freezing temperatures by up to 7 °C but did not have a large effect on the shapes of the freezing curves (i.e., slopes in Fig. 3.1 and 3.2). In terms of the ice nucleating active site density, HNO₃ or HCl decreased n_s by up to 2 orders of magnitude, assuming the relationship between n_s and temperature is relatively linear for K-rich feldspar. To simplify our analysis below, we focused on change in median freezing temperatures (ΔT_{50}) caused by the solutes, which was calculated with Eq. 2.3. When calculating ΔT_{50} values, we only compared freezing data generated from the same K-rich feldspar suspensions. As we have shown previously (Yun et al., 2020), the variability of the median freezing temperature between different K-rich feldspar suspensions (approximately ± 1.25 °C) is larger than the variability within the same suspension.

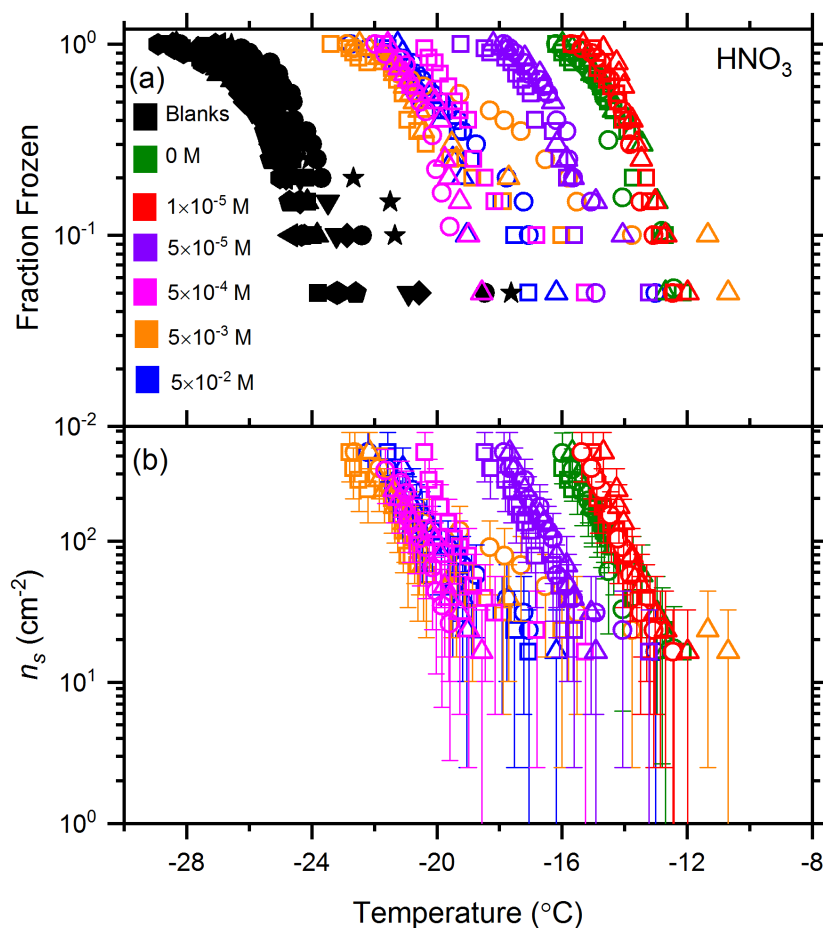


Figure 3.1: Freezing data for the effect of HNO₃ on the ice nucleating ability of K-rich feldspar. (a) The fraction of frozen droplets containing K-rich feldspar as a function of HNO₃ concentration (0 M, olive; 1×10⁻⁵ M, red; 5×10⁻⁵ M, violet; 5×10⁻⁴ M, magenta; 5×10⁻³ M, orange; 5×10⁻² M, blue). Also included are the fraction frozen of pure water droplets (i.e., blanks) from multiple trials. Different symbols with the same color correspond to different trials. (b) ice nucleating active site density (n_s) as a function of temperature calculated with the freezing data from panel (a). The error bars for n_s correspond to the 95 % confidence intervals calculated with the nucleation statistics from Koop et al. (1997).

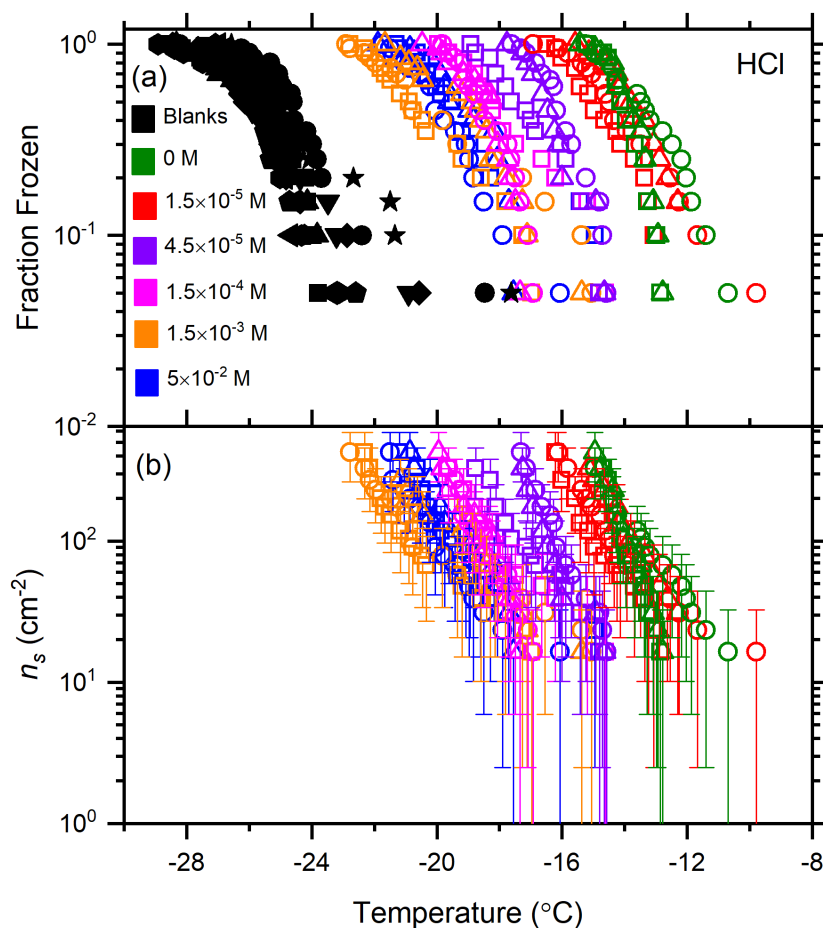


Figure 3.2: Freezing data for the effect of HCl on the ice nucleating ability of K-rich feldspar. (a) The fraction of frozen droplets containing K-rich feldspar as a function of HCl concentration (0 M, olive; 1.5 × 10⁻⁵ M, red; 4.5 × 10⁻⁵ M, violet; 1.5 × 10⁻⁴ M, magenta; 1.5 × 10⁻³ M, orange; 5 × 10⁻² M, blue). Also included are the fraction frozen of pure water droplets (i.e., blanks) from multiple trials. Different symbols with the same color correspond to different trials. (b) ice nucleating active site density (n_s) as a function of temperature calculated with the freezing data from panel (a). The error bars for n_s correspond to the 95% confidence intervals calculated with the nucleation statistics from Koop et al. (1997).

Shown in Fig. 3.3 are the ΔT_{50} values for the droplets containing K-rich feldspar as a function of HNO₃ and HCl concentrations. At the lowest concentrations ($\sim 1 \times 10^{-5}$ M), ΔT_{50} was

smaller than the uncertainties in the measurements. On the other hand, at the highest concentrations ($\sim 1 \times 10^{-3}$ M to 5×10^{-2} M), ΔT_{50} was approximately -6 °C (corresponding to a decrease of n_s by up to 2 orders of magnitude, assuming linearity between n_s and temperature). A clear trend of decreasing ΔT_{50} with an increasing concentration of inorganic acids is observed over the range of 1×10^{-5} M to 5×10^{-2} M. Furthermore, the results for HNO_3 overlap with the results for HCl . This overlap suggests that the decrease in the median freezing temperatures was induced by the cation (H^+), and not the anions (NO_3^- or Cl^-). Consistent with these results, Whale et al. (2018) and Kumar et al. (2018) showed that the increase in the ice nucleating ability of K-rich feldspar by ammonium salts at low concentrations was also caused by the cation (NH_4^+), and was independent of the anions. Yun et al. (2020) also showed that the change in freezing temperature of K-rich feldspar caused by potassium salts was due to the cation (K^+) and independent of the anion type.

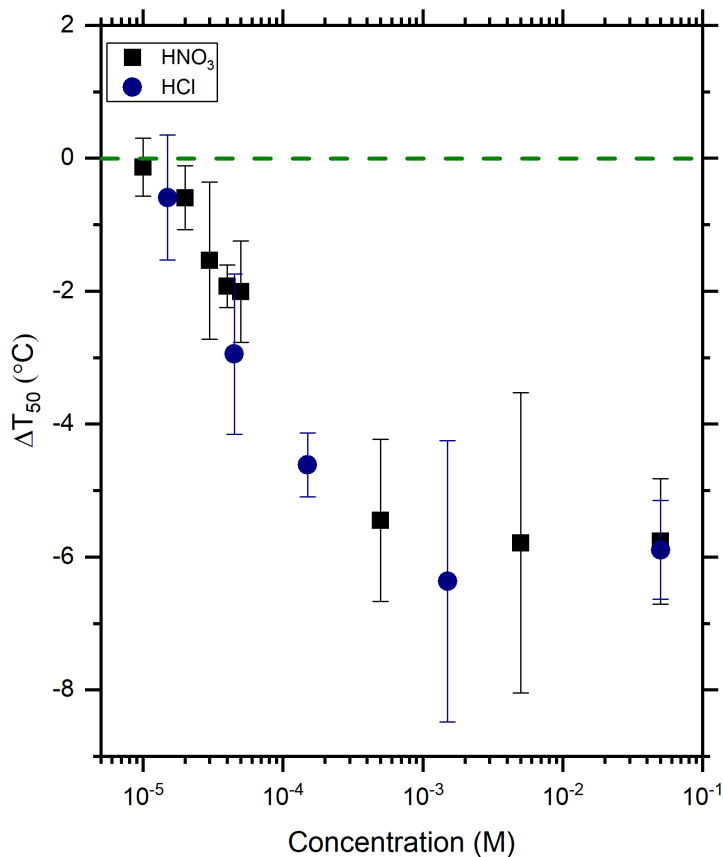


Figure 3.3: ΔT_{50} values as a function of concentration for HNO₃ and HCl solutions, where ΔT_{50} is the difference of median freezing temperature between the droplets containing K-rich feldspar with and without the inorganic acids. The error bars are the propagation of temperature measurement uncertainty (0.25 °C) and 95 % confidence intervals from 3 trials based on Student's t-distribution. The olive dashed line indicates the position where ΔT_{50} is 0 °C.

The pH dependence of ΔT_{50} for K-rich feldspar in solutions of HCl and HNO₃ is plotted in Fig. 3.4. The data reveals a sharp decrease in ΔT_{50} values from approximately 0 °C at the pH of ~5, down to -6 °C below the pH of ~3.5. These data can be well fitted with a Boltzmann sigmoid function, which was added to guide the eye and has no physical significance. The result of (Kumar

et al., 2018), with a ΔT_{50} of about $-7\text{ }^{\circ}\text{C}$ for K-rich feldspar submerged in a NH_4HSO_4 solution of $\text{pH} = 1.2$ for 10 days, aligns with ours. Burkert-Kohn et al. (2017) showed that the immersion freezing temperature induced by K-rich feldspar decreased by at least $10\text{ }^{\circ}\text{C}$ after exposure to 1 M HNO_3 and H_2SO_4 ($\text{pH} = 0$ and -0.1 , respectively) for 12 h followed by washing to remove the acids. This reduction in freezing temperature was greater than predicted by an extrapolation of the Boltzmann sigmoid function to lower pH values (Fig. 3.4). This could indicate that the fitted Boltzmann sigmoid function might not be suitable for predicting the effect of inorganic acids at extremely low pH values (< 1). The difference between the results from Burkert-Kohn et al. (2017) and current results could be due to different exposure times of K-rich feldspar to the inorganic acids and different concentrations of inorganic acids. Burkert-Kohn et al. (2017) used an exposure time of 10 days and concentrated inorganic acids (1 M), while the exposure time in our study was approximately 15-20 minutes and the concentration of the inorganic acids were less than 0.1 M. Longer exposure times could lead to larger decrease in freezing temperature, although more work is needed to confirm this hypothesis. Note that the freezing temperature range of the unaffected K-rich feldspar particles probed in our study is ~ -16 to $-10\text{ }^{\circ}\text{C}$, which corresponds much rarer ice nucleating active sites compared to Burkert-Kohn et al. (2017), who investigated a freezing temperature range of ~ -38 to $-30\text{ }^{\circ}\text{C}$. In addition, the sources of K-rich feldspar samples were different, which could lead to different results (Yun et al., 2020).

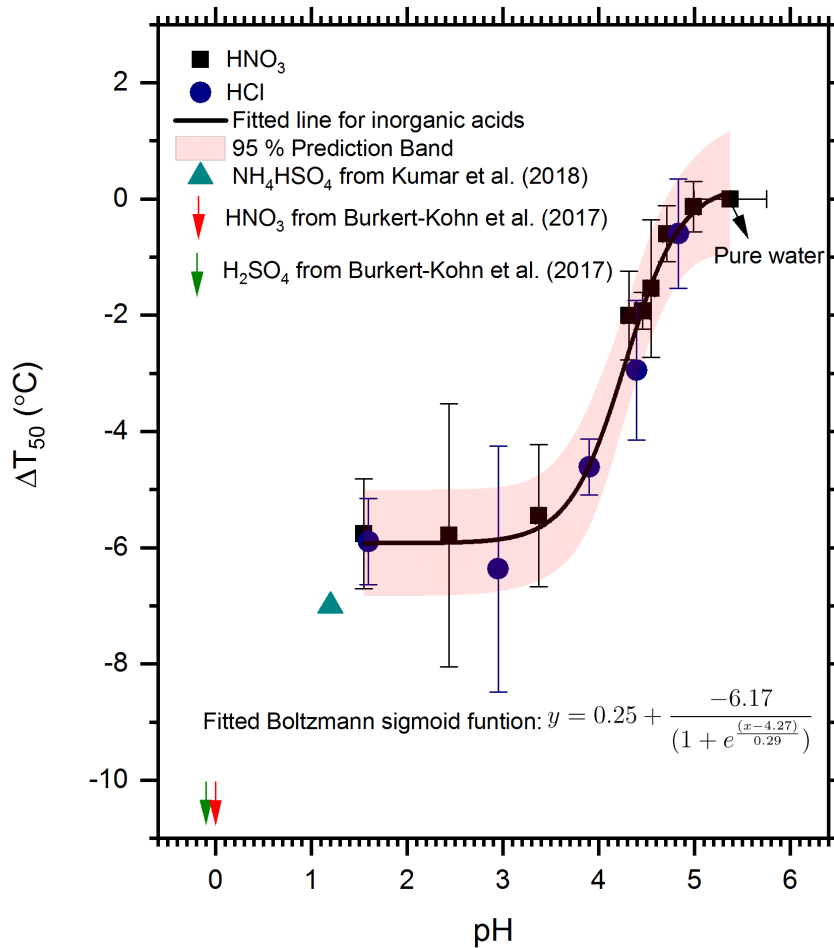
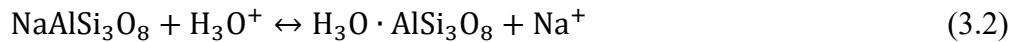
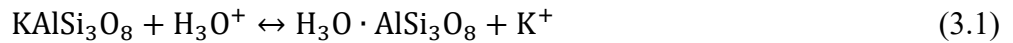


Figure 3.4: ΔT_{50} values as a function of pH for HNO₃ and HCl containing droplets, where ΔT_{50} is the difference of median freezing temperature between the droplets containing K-rich feldspar with and without the inorganic acids. The error bars for ΔT_{50} are the propagation of temperature measurement uncertainty (0.25 °C) and 95 % confidence intervals from 3 trials based on Student's t-distribution. The error bars for pH take into account the pH meter uncertainty (0.01 unit) and 95 % confidence intervals from 3 pH measurements based on Student's t-distribution. The black solid line is a fit to the ΔT_{50} values for both HNO₃ and HCl using a Boltzmann sigmoid function. The shaded region is the 95 % prediction band of the fitted line. Also included in the figure are the data from Kumar et al. (2018) where they exposed K-rich feldspar to a NH₄HSO₄ solution (pH = 1.12), and Burkert-Kohn et al. (2017) where they exposed K-rich feldspar to sulfuric acid (pH = -0.1)

and nitric acid (pH = 0), with pH values estimated with the Extended Aerosol Inorganic Model (Clegg et al., 2001). The results from Burkert-Kohn et al. (2017) are upper limits for the ΔT_{50} values since they mainly observed homogeneous nucleation after exposing K-rich feldspar to the strong acids.

3.3.2 Surface composition of K-rich feldspar before and after exposure to HCl and its relationship to ΔT_{50} .

The K-rich feldspar used for this work consists of 85 % microcline (KAlSi_3O_8) and 15 % ($\text{NaAlSi}_3\text{O}_8$). These minerals consist of a three-dimensional network of SiO_4 and AlO_4^- tetrahedra, and K^+ (microcline) or Na^+ (albite) ions locked in nanometric interstices within the framework. Exposing microcline and albite particles to acidic solutions can readily exchange the alkali metal ions through the following reactions (Stumm and Morgan, 1981):



and thus, alter the surface loadings of alkali metal ions that could intervene in the ice nucleation process.

In addition to the direct ion exchange, acidic solutions can preferentially leach Al from the surface of K-rich feldspar, leaving a silica-rich altered layer resulting from this incongruent dissolution (Nesbitt et al., 1991; Gautier et al., 1994; Welch and Ullman, 1996; Kobayashi et al., 2001; Chardon et al., 2006; Lee et al., 2008; Hellmann et al., 2012; Ruiz-Agudo et al., 2014; Yang et al., 2014; Yuan et al., 2019). Alkali feldspars can also undergo natural weathering, resulting in formation of clay minerals and simpler oxides on geological time scale (Lee et al., 2008; Yuan et al., 2019). In our experiments, the exposure time of K-rich feldspar to solution was ~ 20 minutes. For this time scale, the dissolution of feldspars is in the early stage, and ion exchange is expected

to occur rapidly accompanied by some dissolution (Chardon et al., 2006; Yuan et al., 2019). However, the formation of new mineral phases is not expected to be important.

To determine the extent to which the original composition of the K-rich feldspar surfaces was altered by exposure to acid solutions, we monitored the atomic ratios K/Si, Na/Si, and Al/Si of our samples using cryo-XPS (Fig. 3.5a). These samples were mixed with pure water or HCl for approximately 25 minutes before the cryo-XPS measurements, as in our ice nucleation experiments.

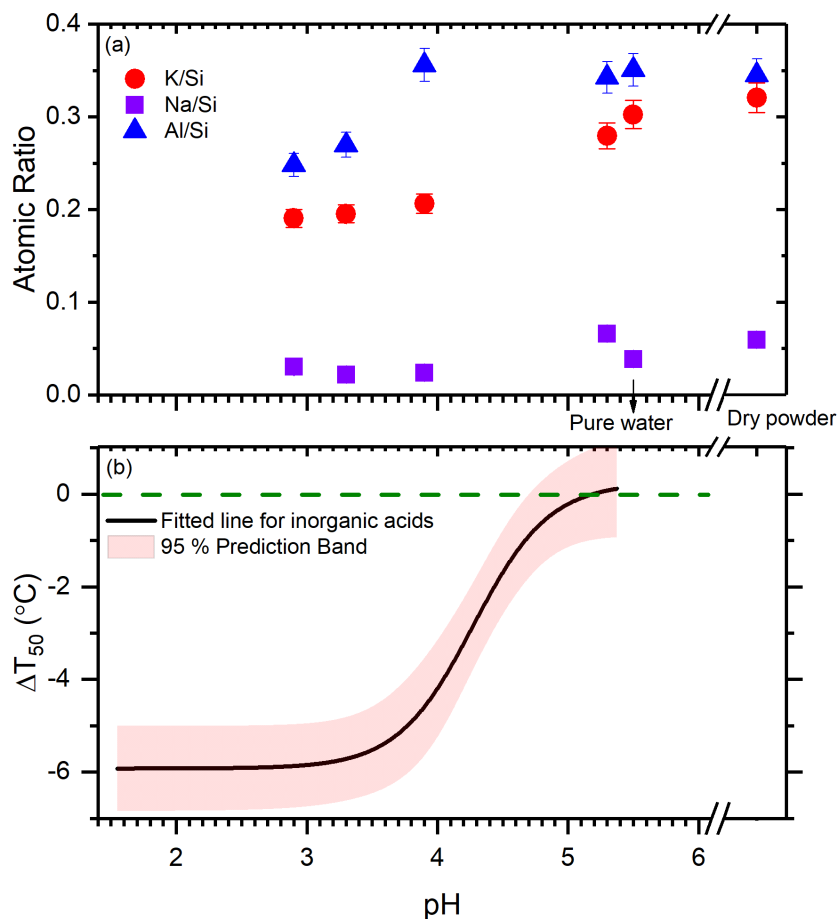


Figure 3.5: Atomic ratios K/Si, Na/Si, and Al/Si (panel (a)) for K-rich feldspar exposed to pure water or HCl solutions and ΔT_{50} (panel (b)) for K-rich feldspar exposed to HCl and HNO₃ solutions. The pure water case is indicated in the figure. Also included in panel (a) are atomic ratios for a dry powder of K-rich feldspar. The error bars for the atomic ratios are the uncertainty of the cryo-XPS measurements (5%) which corresponds to two standard deviations determined from repeating 3 trials under the same condition.

The data from cryo-XPS (Fig. 3.5a) suggests the K/Si and Al/Si ratios of our samples exposed to pure water (pH = ~ 5.5) (K/Si = ~0.32; Al/Si = ~0.34) were close to those of the dry powder and agreed with the stoichiometry of K-rich feldspar. The atomic ratio Na/Si was approximately 0.05, which is also close to the expected value considering that our K-rich feldspar

contained 15 % albite. Under conditions of small to negligible ion exchange and incongruent dissolution (pH = 5 - 5.5), ΔT_{50} remained approximately 0 °C. However, under conditions where ion exchange was larger and incongruent dissolution remained small (pH = 3.9), ΔT_{50} became negative (approximately -5 °C) and close to the maximum values. This is consistent with the results in Chapter 2 (Yun et al., 2020) that showed K^+ surface loadings acquired in solutions of low salt concentrations ($\leq 5 \times 10^{-3}$ M) were positively correlated to the ice nucleating ability of K-rich feldspar. Na^+ also undergoes ion exchange but this should not affect freezing temperatures as strongly as variations in K^+ loadings since Na^+ surface loadings acquired in solutions of low salt concentrations ($\leq 5 \times 10^{-3}$ M) were not positively correlated to the ice nucleating ability of K-rich feldspars (Yun et al., 2020). Under conditions where incongruent dissolution became more important (pH = 3.3 and 2.9), ΔT_{50} decreased further to a value of approximately -6 °C, the largest value observed in our experiments. These combined observations illustrate that the decrease in the ice nucleating ability of K-rich feldspar is correlated to both ion exchange and incongruent dissolution. This is consistent with Kumar et al. (2018) where they suggested that the irreversible loss of ice nucleating active sites for K-rich feldspar under conditions of pH = 1.2 was possibly due to the accelerated dissolution of K-rich feldspar surfaces.

Whale et al. (2017) showed that the high ice nucleating ability of alkali feldspars is associated with defect sites at the regions of feldspar with perthitic texture. Kiselev et al. (2017) also showed that the high ice nucleating ability of K-rich feldspar may be due to high-energy (100) surfaces exposed at surface defects. These defect sites and high-energy surfaces are likely especially susceptible to ion exchange and incongruent dissolution in the early stages of weathering processes (Lee and Parsons, 1995).

3.3.3 The effects of organic solutes on the immersion freezing by K-rich feldspar at low concentrations

Shown in Fig. 3.6 and Fig. 3.7 are the freezing data for K-rich feldspar exposed to different concentrations of levoglucosan (an example of polyols) and citric acid (an example of carboxylic acids). Freezing data of K-rich feldspar exposed to the other organic solutes studied here are shown in Fig. C.1 – C.7. Like the inorganic acids, the organic solutes did not have a large effect on the shape of the freezing curves. Therefore, to simplify our analysis, we focused on the change in median freezing temperatures (ΔT_{50}) caused by the organic solutes, which is similar to the approach used for the inorganic acids.

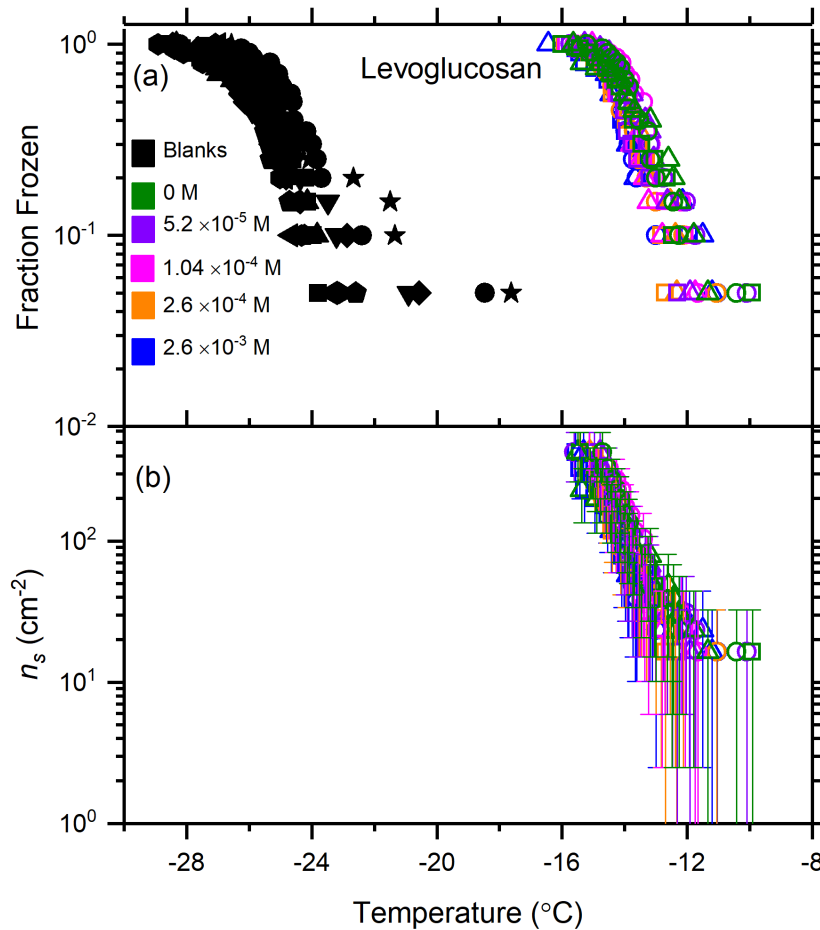


Figure 3.6: Freezing data for the effect of levoglucosan on the ice nucleating ability of K-rich feldspar. (a) The fraction frozen of droplets containing K-rich feldspar as a function of levoglucosan concentration (0 M, olive; 5.2×10^{-5} M, violet; 1.04×10^{-4} M, magenta; 2.6×10^{-4} M, orange; 2.6×10^{-3} M, blue). Also included are the fraction frozen of pure water droplets (i.e., blanks) from multiple trials. Different symbols with the same color correspond to different trials. (b) Ice nucleating active site density (n_s) as a function of temperature calculated with the freezing data from panel (a). The error bars for n_s correspond to the 95% confidence intervals calculated with the nucleation statistics from Koop et al. (1997).

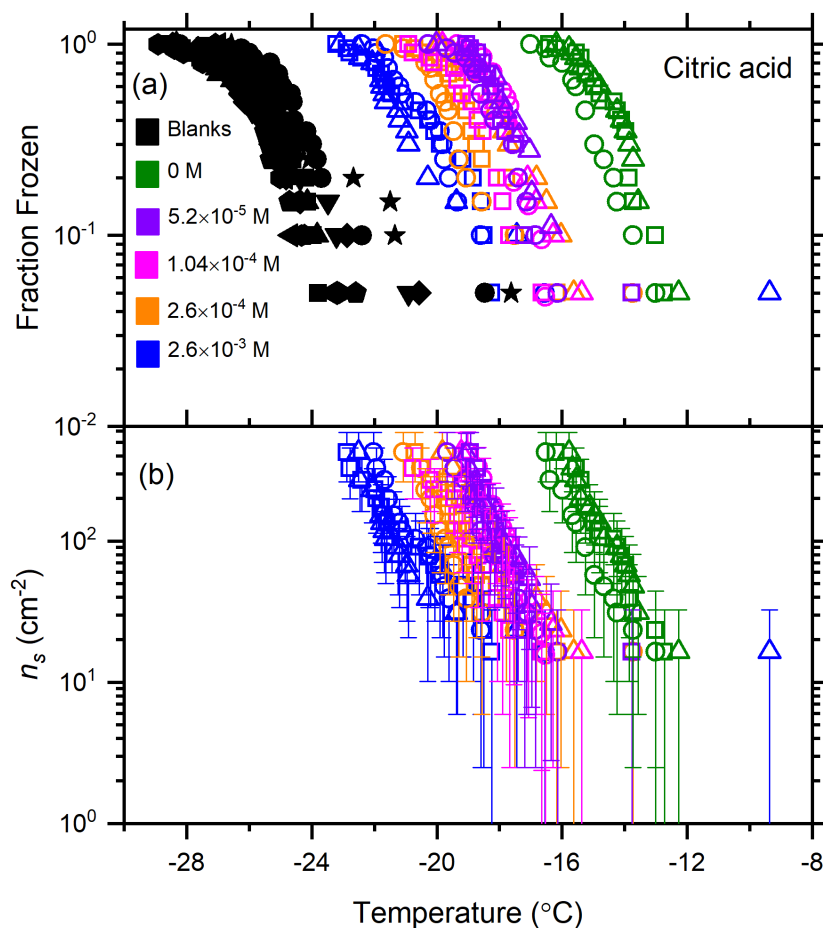


Figure 3.7: Freezing data for the effect of citric acid on the ice nucleating ability of K-rich feldspar. (a) The fraction frozen of droplets containing K-rich feldspar as a function of citric acid concentration (0 M, olive; 5.2×10^{-5} M, violet; 1.04×10^{-4} M, magenta; 2.6×10^{-4} M, orange; 2.6×10^{-3} M, blue). Also included are the fraction frozen of pure water droplets (i.e., blanks) from multiple trials. Different symbols with the same color correspond to different trials. (b) Ice nucleating active site density (n_s) as a function of temperature calculated with the freezing data from panel (a). The error bars for n_s correspond to the 95% confidence intervals calculated with the nucleation statistics from Koop et al. (1997).

Shown in Fig. 3.8 are the ΔT_{50} values for the polyols and carboxylic acids as a function of their concentrations. The polyols changed the freezing temperature of the droplets by less than 0.5

°C and less than the uncertainty of the measurements in all cases, except for levoglucosan at a concentration of 2.6×10^{-3} M. These results reveal that polyols had only a small affect, if any, on the ice nucleating ability of K-rich feldspar for the entire concentration range studied. On the other hand, the carboxylic acids decreased the freezing temperature by greater than approximately 1.5 °C and by more than the uncertainty of the measurements in all cases. At concentrations of 5.2×10^{-5} M and 1.04×10^{-4} M, the carboxylic acids decreased the ΔT_{50} by approximately 1.5 to 3.5 °C (corresponding to a decrease in n_s values by a factor of approximately 5 – 20, assuming a linear relationship between n_s and temperature). At concentrations of 2.6×10^{-4} M and 2.6×10^{-3} M, the carboxylic acids decreased the ΔT_{50} by approximately -4.5 to -6.5 °C (corresponding to a decrease in n_s values by a factor of approximately 50 – 200, also assuming a linear relationship between n_s and temperature). A clear trend was observed between the concentration of the carboxylic acids and ΔT_{50} with the ΔT_{50} values becoming more negative as the concentration increased.

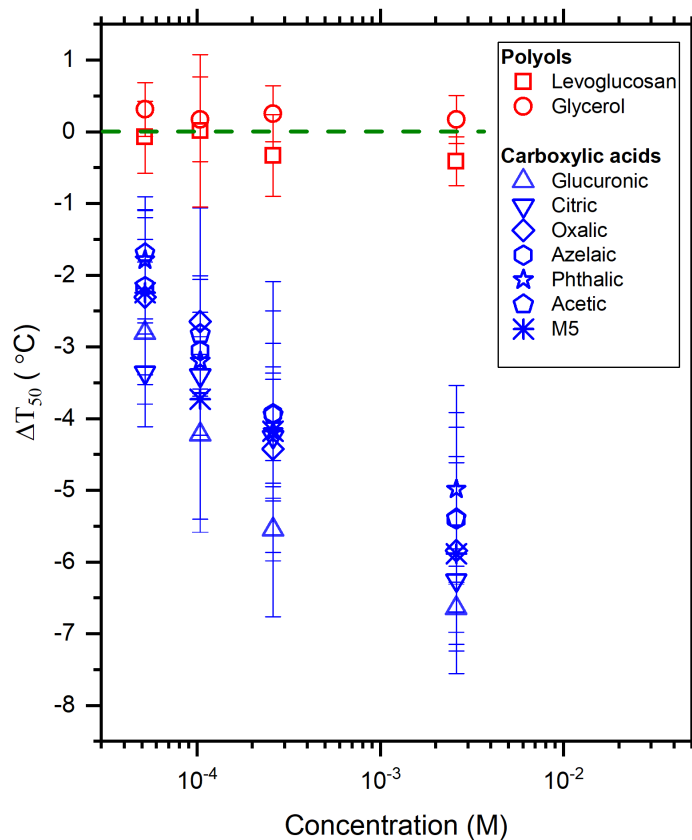


Figure 3.8: ΔT_{50} values as a function of concentration for the organic molecules studied, where ΔT_{50} is the difference of median freezing temperature of droplets containing K-rich feldspar with and without the organic molecules. The error bars are the propagation of temperature measurement uncertainty (0.25 °C) and 95 % confidence intervals from 3 trials based on Student's t-distribution. The olive dashed line indicates the position where ΔT_{50} is 0 °C.

As mentioned in the Introduction, Tobo et al. (2012) and Wex et al. (2014) investigated the effect of levoglucosan coatings on the ice nucleating ability of kaolinite, and Zobrist et al. (2008) and Koop and Zobrist (2009) investigated the effect of polyethylene glycol on the ice nucleating ability of ATD. In all of these studies, the polyols did not significantly decrease the ice nucleating ability of the mineral dust, which is consistent with our results. Kanji et al. (2019) investigated the

effect of SOA coatings from the dark ozonolysis of α -pinene on the ice nucleating ability of natural Sahara dust and Asian dust particles. These coatings were expected to contain carboxylic acids, as well as other types of organic molecules. The authors did not observe a significant decrease in the ice nucleating ability of the mineral dust particles, while we observed a decrease in the ice nucleating ability of K-rich feldspar in the presence of carboxylic acids. This apparent discrepancy could be due to differences in the concentrations of the carboxylic acids studied in our experiments compared to Kanji et al. (2019) or differences in the type of mineral dust used. The Sahara dust and Asian dust particles studied by Kanji et al. (2019) have a high fraction of quartz, which may be less sensitive to carboxylic acid solutes than the K-rich feldspar studied here.

In Fig. 3.8 error bars often overlapped, making a comparison between the individual carboxylic acids difficult. To facilitate a better comparison of between individual carboxylic acids, in Fig. 3.9 we show the ΔT_{50} values as a function of the carboxylic acid types. No clear trend between the types of carboxylic acids and the ΔT_{50} values is observed in Fig. 3.9. In other words, none of the individual carboxylic acids had consistently higher or lower ΔT_{50} values at any of the concentrations studied. In addition, a clear relationship between ΔT_{50} and the number of carboxyl groups in the molecules is not observed.

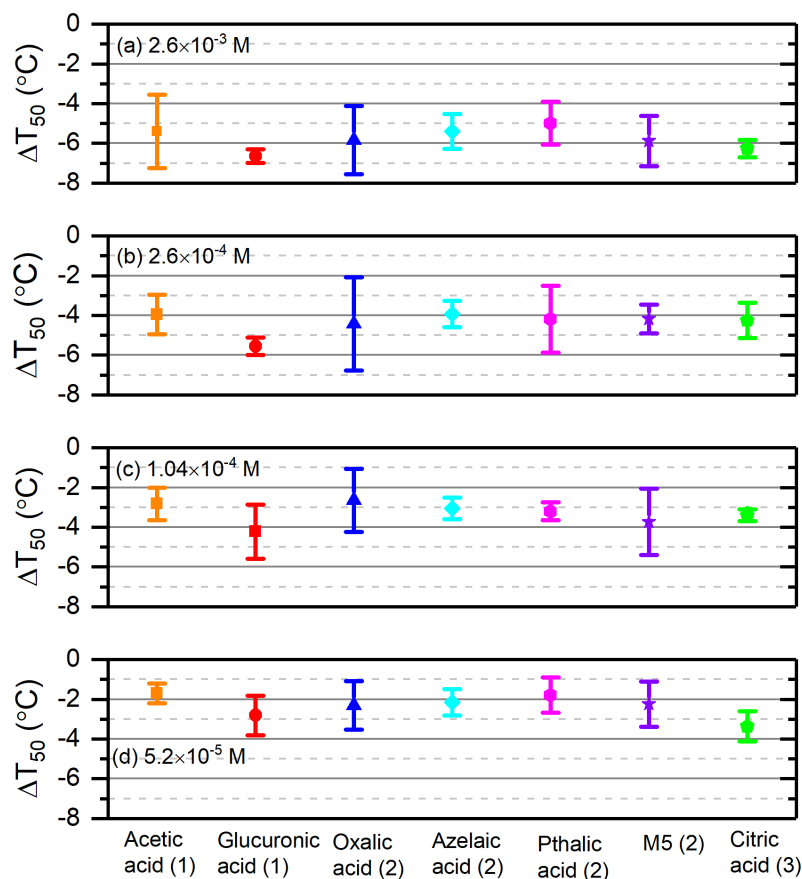


Figure 3.9: The ΔT_{50} values for carboxylic acids at concentrations of 2.6×10^3 M (panel (a)), 2.6×10^4 M (panel (b)), 1.04×10^4 M (panel (c)), and 5.2×10^5 M (panel (d)). The error bars for ΔT_{50} are the propagation of temperature measurement uncertainty (0.25 °C) and 95 % confidence intervals from 3 trials based on Student's t-distribution. The numbers within the brackets in the x-axis label indicate the number of carboxyl groups in the carboxylic acids.

The pH of carboxylic acid solutions used in the freezing experiments ranged from 2.5 to 4.5. Shown in Fig. 3.10 are ΔT_{50} values for the carboxylic acids plotted as a function of pH of the solutions. A clear relationship between the ΔT_{50} values and the pH of the solution was observed, where the lower pH values correspond to lower ΔT_{50} values. Even more interesting, the ΔT_{50}

values for the carboxylic acids overlap with the 95 % prediction band for the inorganic acids if all the results are plotted as a function of pH of the solutions. This suggests that the decrease in freezing temperature caused by the carboxylic acids can simply be explained by the increase in concentration of H^+ (i.e. pH) brought by the carboxylic acids rather than complexation between the mineral surfaces and carboxylate anions in the solutions. This can be explained by the low point of zero charge of K-rich feldspar (< 2) (Kosmulski, 2009), which does not favor carboxylate anions as binding ligands, and by the small reaction time (~ 15 - 25 min) limiting surface loadings and the formation of inner-sphere complexes (Axe and Persson, 2001) that could possibly form with Al surface sites. This also aligns with previous work pointing to the small effects of carboxylate anion adsorption on feldspar dissolution (Oelkers and Schott, 1998). Our work consequently points to a greater effect of H_3O^+/K^+ ion exchange and acid-induced incongruent dissolution than the binding of ligands over short reaction times on ice nucleation initiated by the rare active sites within the temperature regime probed in this study. However, we do not rule out the possibility that the binding of ligands has a significant effect on the ice nucleating ability of K-rich feldspar for longer exposure times, at lower freezing temperatures, or for different K-rich feldspar samples.

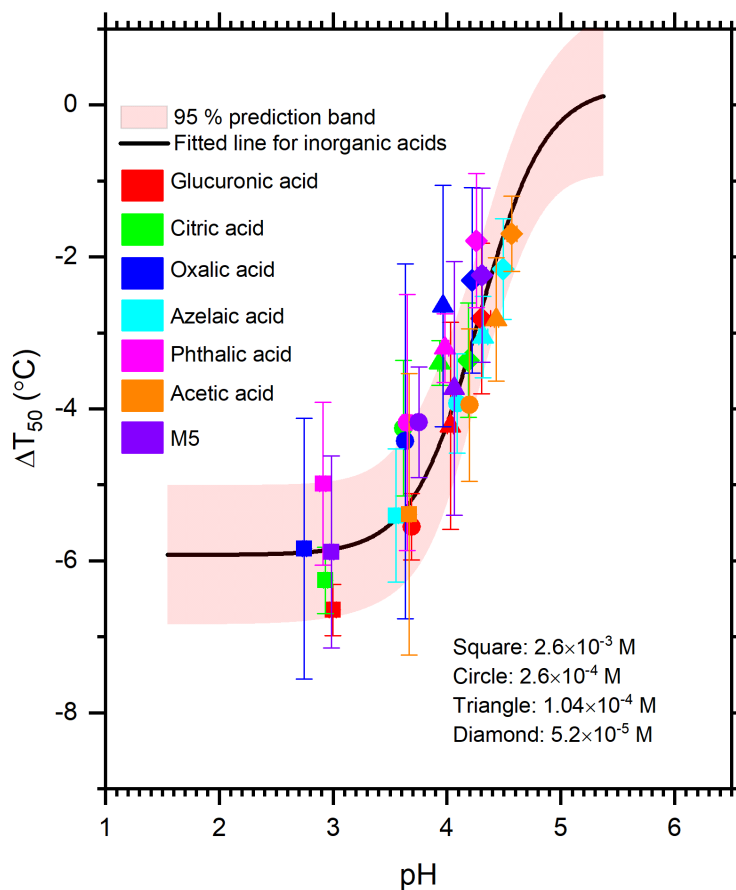


Figure 3.10: ΔT_{50} values as a function of pH for the carboxylic acids. The color indicates the type of carboxylic acid and the symbol type indicates the concentration (see legends). The error bars for ΔT_{50} are the propagation of temperature measurement uncertainty (0.25 °C) and 95 % confidence intervals from 3 trials based on Student's t-distribution. The error bars for pH are the propagation of pH meter uncertainty (0.01 unit) and 95 % confidence intervals from 3 pH measurements based on Student's t -distribution. The black solid line is a fit to the ΔT_{50} values for both HNO_3 and HCl using a Boltzmann sigmoid function. The shaded region is the 95 % prediction band of the fitted line.

3.4 Summary and conclusion

The effect of inorganic acids (10^{-5} M to 5×10^{-2} M) on the ice nucleating ability and surface properties of K-rich feldspar was examined in this study for short exposure times (~ 15 -20 min). The presence of HNO_3 and HCl caused the median freezing temperature of K-rich feldspar to decrease by up to 7°C with a clear trend of decreasing freezing temperature with a decreasing pH. Significant ion exchange and incongruent dissolution of the K-rich feldspar surface were observed at the pH of ~ 3 , at which, a decrease of 6°C in median freezing temperature was also observed. We conclude that the decrease in ice nucleating ability of the K-rich feldspar exposed to inorganic acids was most likely due to ion exchange and irreversible incongruent dissolution at the K-rich feldspar surface.

In addition, we studied the effect of polyols and carboxylic acids at low concentrations (approximately 3×10^{-5} to 3×10^{-3} M) on the immersion freezing of K-rich feldspar at short exposure times (~ 15 -20 min). We observed no significant reduction in the median freezing temperature of K-rich feldspar when using polyols as solutes but found a large decrease (up to approximately 7°C) when using carboxylic acids as solutes. The decrease in the ice nucleating ability of K-rich feldspar caused by the carboxylic acids was most likely due to the increased H^+ contributed by the carboxylic acids. Based on our results, the complexation between carboxylate anions and K-rich feldspar surfaces had little or no role in reduction in the ice nucleating ability of K-rich feldspar. This is likely due to the low point of zero charge of K-rich feldspar and the short interaction time between carboxylate anions and the K-rich feldspar surfaces in our experiments.

Overall, our results suggest that the pH of inorganic acid and organic acid aqueous coatings can impact the ice nucleation ability of K-rich feldspar. At a pH of 5 – 6, the acid had no effect.

As the pH decreased from ~5 to ~3.5, the freezing temperature decreased by approximately 6 °C. At pH of 1.5 – 3.5, the acid consistently decreased the freezing temperature by approximately 6 °C. The pH in clouds droplets in the atmosphere range from 2 to 7 (Pye et al., 2020). In addition, the pH in aerosol particles range from -1 to 8 (Pye et al., 2020). Hence the pH range we investigated is atmospherically relevant. A decrease in freezing temperature by 6 °C corresponds to a decrease in ice nucleating active site densities of up to two orders of magnitude, which can lead to significant changes in ice crystal concentrations, and hence optical properties and lifetime of mixed-phase clouds. However, the effect of acid coatings is rarely considered in atmospheric models when predicting concentrations of mineral dust INPs (Lohmann and Hoose, 2009; Atkinson et al., 2013; Vergara-Temprado et al., 2017).

This chapter probes a freezing temperature range of -16 °C to -10 °C for the unaffected K-rich feldspar particles, which corresponds to rare ice nucleating active sites, and focuses on the effect of short exposure times between the solutes and the K-rich feldspar. To provide more insights into the effects of solutes on the immersion freezing of K-rich feldspar, experiments investigating longer exposure times, lower freezing temperatures, and K-rich feldspar samples from other sources are needed in the future.

Chapter 4: Mineral dust and biological ice nucleating particles in the Canadian High Arctic during the fall of 2018 based on ammonium sulfate and heat assays.

4.1 Introduction

Several studies have measured the concentrations of INPs in the Arctic (Fountain and Ohtake, 1985; Bigg, 1996; Bigg and Leck, 2001; Rogers et al., 2001; Prenni, Demott, et al., 2009; Conen et al., 2016; Mason et al., 2016; Creamean et al., 2018, 2019; Šantl-Temkiv et al., 2019; Si et al., 2019; Wex et al., 2019; Irish, Hanna, Willis, et al., 2019; Hartmann, Adachi, et al., 2020; Hartmann, Gong, et al., 2020). In most cases, these measurements were carried out for relatively short periods of time during intensive field campaigns. A few studies have quantified how INP concentrations vary with season (Fountain and Ohtake, 1985; Bigg, 1996; Bigg and Leck, 2001; Wex et al., 2019). Fountain and Ohtake (1985) measured INP concentrations at 3 ground sites in Alaska for a full year and showed that the INP concentrations were higher in the summer and lower in the winter. Bigg (1996) and Bigg and Leck (2001) observed a decline in the INP concentrations in the Arctic Ocean from the summer to the fall. In addition, Wex et al. (2019) recently monitored the weekly INP concentrations at 4 stations in the Arctic and observed a seasonal variation in the concentrations of INPs with higher concentrations in the summer and fall and lower concentrations in the winter and spring. Despite these previous studies, additional measurements of the concentrations of INPs in the Arctic will improve our understanding of the concentrations of INPs in the region and how these concentrations vary with freezing temperature, season, and location in the Arctic.

Compared to studies that measured the concentrations of INPs in the Arctic, fewer studies have directly probed the composition of INPs in the Arctic. Kumai and Francis (1962) characterized residuals of snow crystals over Greenland in the summer using electron microscopy and concluded that the snow crystals were formed mainly on clay mineral particles. Using transmission electron spectroscopy and energy dispersive X-ray (EDX), Rogers et al. (2001) showed that INPs over the Arctic Ocean during the late spring consisted of mostly crustal minerals and carbonaceous particles. Similarly, using transmission electron spectroscopy and EDX, Prenni and Demott et al. (2009) showed that INPs over northern Alaska in October often consisted of metal oxides or mineral dust and carbonaceous particles. Šantl-Temkiv et al. (2019) showed that a large fraction of INPs over Greenland in the summer were heat-labile, and hence, likely biological. Similarly, two very recent studies showed that a large fraction of INPs over the Arctic Ocean during the spring and early summer were heat-labile, and hence, likely biological (Hartmann, Adachi, et al., 2020; Hartmann, Gong, et al., 2020). Despite these measurements, more work is needed to better understand the composition of INPs in the Arctic. For example, more information is needed on the relative contributions of mineral dust particles and biological particles to the INP population and how the relative contributions change with the freezing temperature, season, and location in the Arctic.

In the following, we investigated the concentration of INPs in the immersion freezing mode during October and November at Alert, Nunavut, in the Canadian High Arctic. Immersion freezing refers to ice nucleation on INPs immersed in liquid droplets. This mode of heterogeneous freezing has been shown to be a dominant mode of ice nucleation in mixed-phase clouds (Ansmann et al., 2009; Westbrook and Illingworth, 2011).

In addition to measuring the concentrations of INPs, we probed the composition of the INPs by monitoring the changes of the INP concentrations after exposing the samples to ammonium sulfate (an ammonium sulfate assay) and heating at 100 °C (a heat assay). The ammonium sulfate assay was used to detect mineral dust INPs in the samples, and the heat assay was used to detect biological INPs in the samples. The ammonium sulfate assay has not been used previously to detect mineral dust INPs in the atmosphere, and here we show that this is a useful assay to determine the composition of atmospheric INPs as a function of temperature. We also investigated correlations between the concentrations of INPs and concentrations of Al, Na⁺, and Cl⁻ to provide complementary information on the composition and source regions of the INPs. Finally, we used a Lagrangian particle dispersion model to provide additional information on the source regions of the INPs.

4.2 Experimental Method

4.2.1 Sampling site and aerosol sampling

Sampling was performed daily at the Dr. Neil Trivett Global Atmosphere Watch Observatory, Alert, Nunavut, Canada (82.5°N, 62.5°W) from October 19th to November 17th, 2018. The observatory is operated by Environment and Climate Change Canada and located on a plateau with an altitude of 185 m and 6 km from the Canadian Forces Station Alert. The population of the Canadian Forces Station was reported as 62 in 2016. The closest town is Grise Fiord, which is located 800 km to the south of Alert and has a population of 129. The meteorological variables during sampling are indicated in Fig. 4.1. During the sampling campaign, the precipitation was low, and the ambient temperature ranged from -35 °C to -10 °C (with an average of -20.8 °C). The relative humidity usually stayed above 75 % (with an average of 80.8%), and the wind mainly came from southwest and northwest with the speed below 15 km/h.

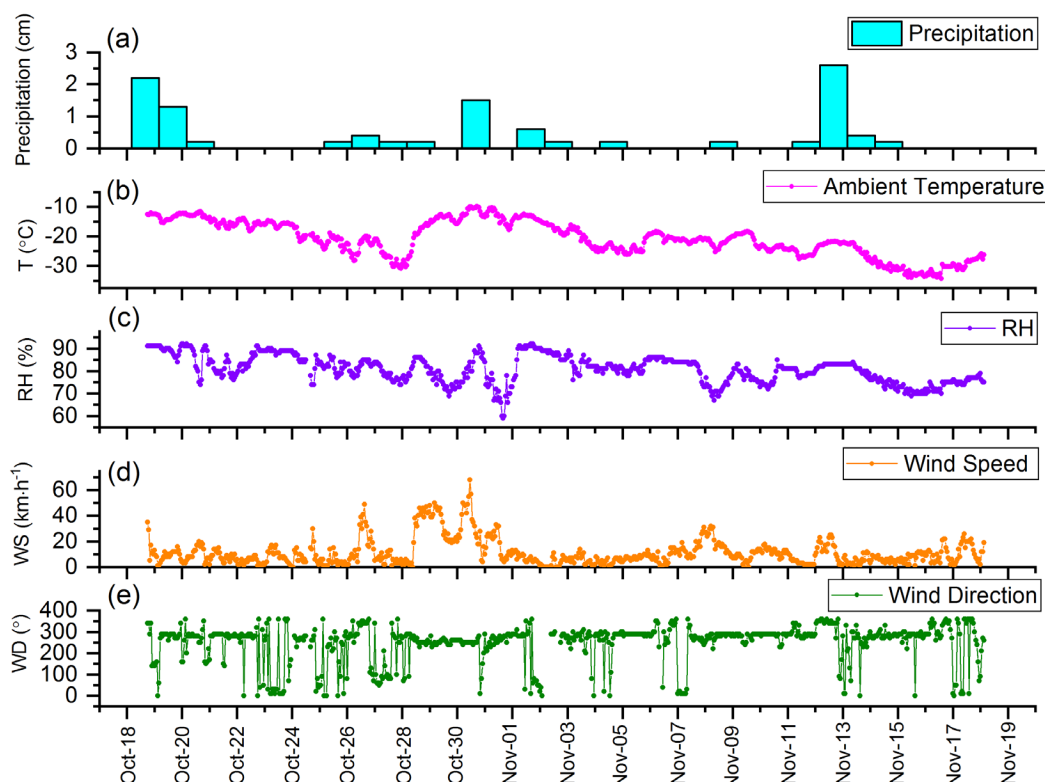


Figure 4.1: The time series of meteorology data at Alert during the campaign: precipitation (panel (a)), ambient temperature (panel (b)), relative humidity (panel (c)), wind speed (panel (d)), and wind direction (panel (e)). The meteorology data were retrieved from the Environment Canada website, <http://climate.weather.gc.ca/>.

For INP measurements, aerosol particles were collected on 47 mm diameter Nucleopore membrane filters (GE Healthcare Whatman™). The collection time for these samples ranged from 17 to 24 hours, with a flow rate of 12 L/min. The membrane filters had a pore size of 0.2 μm and a high collection efficiency of aerosol particles ($> 80\%$ for diameters $> 0.1 \mu\text{m}$) (Spurny and Lodge, 1972; DeMott et al., 2017). This type of filter has been used previously for INP collection (DeMott et al., 2017). After collection, the membrane filters were stored in 50 mL polypropylene tubes (Corning™ Falcon) until analyzed (Section 4.2.2).

For the measurements of Al, Na⁺, and Cl⁻, 47 mm diameter Teflon PM2.5 filters (Measurement Technology Laboratories) were used to collect aerosol samples daily at a flow rate of 16.7 L/min for 17-24 hours. This type of Teflon filter has a collection efficiency of higher than 99.99% for particles $\geq 0.1 \mu\text{m}$ in diameter based on manufacturer's specifications. After collection, the Teflon filters were stored in petri slides until analyzed (Section 4.2.6).

4.2.2 INP measurements for samples without any treatment

The Nucleopore membrane filters collected at Alert were analyzed for INPs at the University of British Columbia. To extract the aerosols from the filters, 5 mL of Milli-Q water was added to the polypropylene tubes containing the filters and then the tubes were shaken for one hour with an orbital shaker at 200 rpm. The INP concentration in each suspension was then determined using the droplet freezing technique as described in Chapter 2 and other studies (Whale et al., 2015; Irish et al., 2017; Irish, Hanna, Xi, et al., 2019). For each sample, sixty 1- μL droplets of the suspension were pipetted onto hydrophobic siliconized slides (Hampton Research) located on a cold plate (Grant EF5600). Another 60 1- μL droplets of Milli-Q water were pipetted onto the previous droplets, resulting in a final volume of 2- μL per droplet. The second 1- μL droplets were added to give the same final volume of the droplets as used in the ammonium sulfate treatment (see below for additional details). The droplets were then isolated from the surrounding atmosphere with a transparent chamber with a digital camera located on the top of the chamber. The temperature of the cold plate was first set to 20 °C, then decreased to -2 °C at a rate of 10 °C/min, stabilized for 1 minute, and then cooled at a rate of 3 °C/min until all the droplets froze. Droplet freezing was recorded by the digital camera and the video was analyzed either manually or automatically by a MATLAB script to determine the freezing temperature of each droplet (Xi

et al., 2021). After determining the freezing temperature of each droplet, the INP concentration in the air was calculated with the following equation (Vali, 1971):

$$INP(T) = \frac{-\ln\left(\frac{N_u}{N_0}\right)V_{suspension} \times 2}{V_{droplet}V_{air}} \quad (4.1),$$

where $INP(T)$ is the concentration of INPs in the air at temperature T , N_u is the number of unfrozen droplets, N_0 is the number of total droplets, $V_{suspension}$ is the volume of water (5 ml) used to generate the suspensions containing INPs from the filter, $V_{droplet}$ is the final volume of the droplets (2 μ l) used in the freezing experiments, and V_{air} is the volume of sampled air for each filter. The factor of 2 in Eq. 4.1 was included since the 1- μ l droplets generated from the suspensions were each diluted with a second 1- μ l droplet containing only Milli-Q water.

4.2.3 Ammonium sulfate assay

A previous study by Worthy et al. (2021) suggests that the addition of ammonium sulfate to atmospheric samples of unknown composition could be used as an indicator or assay for the presence of mineral dust INPs in the samples. Here we used this method to determine if our samples contained mineral dust INPs. We refer to this treatment as an ammonium sulfate assay.

The ammonium sulfate assay is based on previous studies on the ice nucleating ability of mineral dust and non-mineral dust INPs after exposure to dilute ammonium sulfate solutions. Previous studies have shown that ammonium sulfate (as well as other ammonium salts) at dilute concentrations (0.001 M to 0.1 M) can enhance the ice nucleating ability of mineral dust including feldspars, kaolinite, montmorillonite, micas, quartz, and gibbsite (Reischel and Vali, 1975; Kumar et al., 2018, 2019a; Whale et al., 2018; Perkins et al., 2020; Worthy et al., 2021). For example, (Whale et al., 2018) showed that the number of INPs per surface area of materials (n_s) of

microcline, sanidine, and quartz increased by a factor of ~ 10 , ~ 10 , and ~ 5 , respectively, when exposed to 0.015 M NH_4^+ . In addition, Worthy et al. (2021) showed that the median freezing temperatures of Arizona Test Dust (ATD, a proxy for atmospheric dust), potassium-rich feldspar, kaolinite, and montmorillonite increased by approximately $5 \text{ }^\circ\text{C}$, $3 \text{ }^\circ\text{C}$, $7.5 \text{ }^\circ\text{C}$, and $5 \text{ }^\circ\text{C}$, respectively, when exposed to 0.05 M ammonium sulfate. In Fig. 4.2 we have plotted the data from Worthy et al. (2021) in terms of the number of INPs per mass of material (n_m). These data show that the n_m values for Arizona Test Dust, potassium-rich feldspar, kaolinite, and montmorillonite increased by approximately a factor of 10 – 30 when exposed to 0.05 M ammonium sulfate. On the other hand, ammonium sulfate in the concentration range of 0.001 M to 0.1 M is not expected to increase the ice nucleation ability of non-mineral aerosol particles typically found in the atmosphere. Worthy et al. (2021) showed that the median freezing temperatures of several non-mineral dust INPs of atmospherically relevance (i.e., bacteria, fungi, sea-ice diatom exudates, sea-surface microlayer samples, and humic substances) did not significantly change when exposed to 0.05 M ammonium sulfate. Whale et al. (2018) also showed that 0.015 M ammonium sulfate did not have any effect on the immersion freezing of humic acid. In addition, Koop and Zobrist (2009) showed that the freezing temperature of Snowmax was not affected significantly, other than by lowering the water activity of aqueous droplets (i.e., freezing point depression) when exposed to ammonium sulfate solutions of $< 2 \text{ M}$. Reischel and Vali (1975) showed that ammonium sulfate with a concentration of 0.01 M to 1 M had little effect on the immersion freezing leaf derived INPs. However, they did observe that some ammonium salts increased the ice nucleating ability of AgI and CuS hydrosols, but aerosols containing AgI and CuS are not expected to be abundant in the Arctic atmosphere (Barrie, 1985; Barrie and Barrie, 1990).

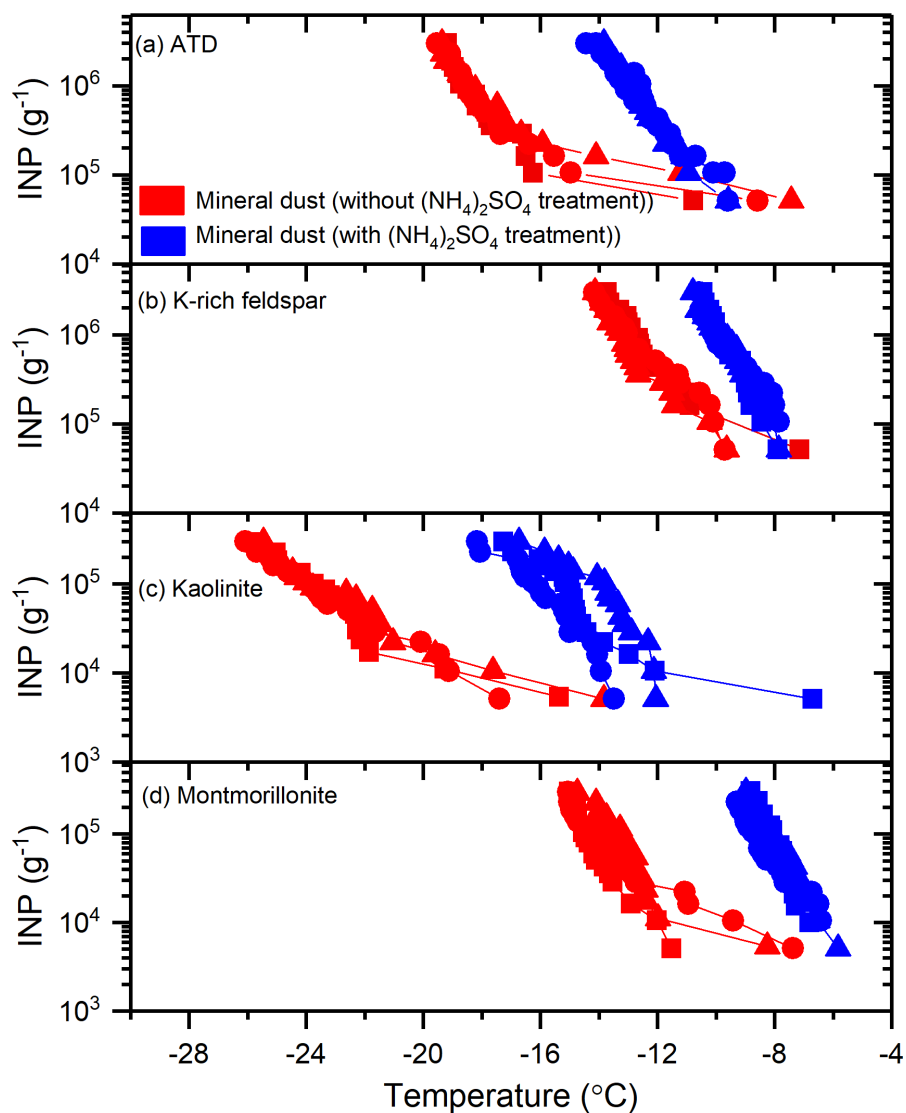


Figure 4.2: The effect of ammonium sulfate treatment on the ice nucleating ability of mineral dust. Panel (a): the number of INPs per gram as a function of temperature for ATD without any treatment and with ammonium sulfate treatment. Panel (b): same as panel (a) but for K-rich feldspar. Panel (c): same as panel (a) but for kaolinite. Panel (d): same as panel (a) but for montmorillonite. The data are from Worthy et al. (2021). For each type of mineral dust, different symbols with the same color represent different trials.

For the ammonium sulfate assay, we first pipetted 60 droplets of the suspensions containing the INPs onto hydrophobic glass slides located on the cold stage. Then a second droplet containing 0.1 M ammonium sulfate was added to each of the previous droplets, resulting in each droplet

having a volume of 2 μL and an ammonium sulfate concentration of 0.05 M. The freezing temperatures of these droplets were then measured and corrected for freezing point depression by ammonium sulfate as described below. The INP concentrations were determined with Eq. 4.1 and compared to the INP concentrations determined for the case without ammonium sulfate. A significant increase in the INP concentration will suggest that the samples contain mineral dust INPs.

The freezing point depression caused by the addition of 0.05 M ammonium sulfate was determined with Eq. 2.1 from Chapter 2. Using Eq. 2.1, the freezing point depression was estimated to be 0.28 $^{\circ}\text{C}$, and all freezing temperatures for droplets with 0.05 M ammonium sulfate were corrected by this amount.

4.2.4 Heat assay

Previous studies have shown that proteinaceous INPs can undergo denaturation and lose their ice nucleating ability after undergoing heating treatment at temperatures from 60 $^{\circ}\text{C}$ to 105 $^{\circ}\text{C}$ (Kieft and Ruscetti, 1990; Pouleur et al., 1992; Garcia et al., 2012; Fröhlich-Nowoisky et al., 2015; Pummer et al., 2015). As a result, heating tests have been used in previous studies as a tool to identify possible biological INPs (Christner et al., 2008; Conen et al., 2011; Garcia et al., 2012; O’Sullivan et al., 2014; Hill et al., 2016; Irish et al., 2017; Šantl-Temkiv et al., 2019; Hartmann, Adachi, et al., 2020; Hartmann, Gong, et al., 2020).

The heat assay to detect the biological INPs in field samples assumes that the ice nucleation properties of non-biological INPs are insensitive to heat. Consistent with this assumption, Conen et al. (2011), Hill et al. (2016) and Peckhaus et al. (2016) showed that the ice nucleating ability of montmorillonite, kaolinite, and K-rich feldspar, respectively, were not significantly affected by heating. Here, we assume that a decrease in the INP concentrations of the samples after heating

and no significant change in the INP concentrations when exposed to 0.5 M ammonium sulfate indicates the presence of biological INP. This is similar to previous studies in the Arctic and other regions that assumed a decrease in INP concentrations after heating likely indicates the presence of biological INPs (Šantl-Temkiv et al., 2019; Hartmann, Adachi, et al., 2020; Hartmann, Gong, et al., 2020). To be conservative, we added the additional constraint that the INP concentrations are not affected by ammonium sulfate.

For the heating assay, an aliquot of each suspension generated from the filter samples was heated at 100 °C for one hour in a heating block (Accublock, Labnet). The freezing temperatures and INP concentrations of the heated samples were then determined as described in Section 4.2.2.

4.2.5 Negative controls for the freezing experiments

As negative controls we used Milli-Q water (5 trials) and an 0.05 M ammonium sulfate solution (3 trials). 5 mL of Milli-Q water or the ammonium sulfate solution was added to polypropylene tubes containing new membrane filters and the tubes were then shaken for one hour with an orbital shaker at 200 rpm. The resulting solution was then used in the freezing experiments as described in Section 4.2.2. The results from these freezing experiments were then used to calculate an average fraction frozen curve for the negative controls (the black curve in Fig. 4.3). Eq. 4.1 was then used to calculate the average INP concentration for the negative controls, assuming the same volume of sampled air as the collected aerosol samples. The average INP concentration for the negative controls was subtracted from the measured INP concentrations for each sample.

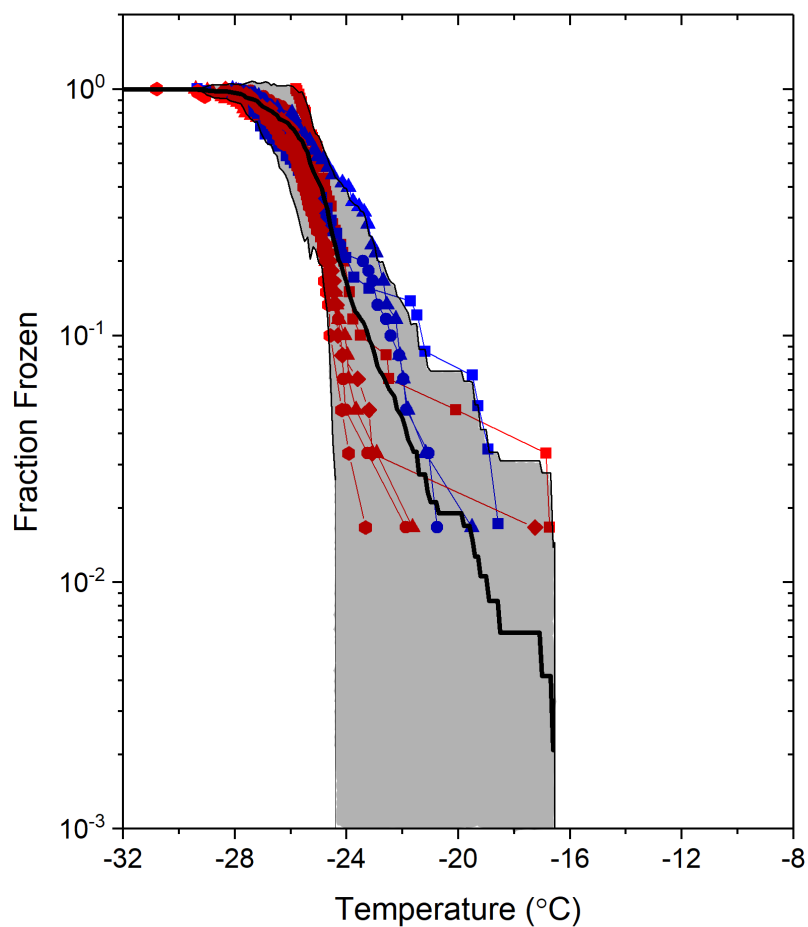


Figure 4.3: The fraction of frozen droplets as a function of temperature for the blanks (8 trials). Red symbols (5 trials) correspond to extracted solutions from the clean filters using Milli-Q water and blue symbols (3 trials) correspond to 0.05 M $(\text{NH}_4)_2\text{SO}_4$ solutions prepared with Milli-Q water. The freezing data for the 0.05 M $(\text{NH}_4)_2\text{SO}_4$ trials was corrected for freezing point depression. The black solid line is the average of the 8 trials and the shading region corresponds to two times the standard deviations of the blanks from the 8 trials.

4.2.6 Measurements of the concentrations of Al, Na^+ , and Cl^-

The Teflon filters collected at Alert were analyzed to determine the concentrations of Al, Na^+ and Cl^- for the same sampling times as the INP samples. The filters were analyzed at Chester

LabNet, Oregon, USA. One set of filters were used to determine the concentration of the element Al by inductively coupled plasma atomic emission spectroscopy (ICP-AES). The element Al is a major constituent of the Earth's crust (Schütz and Rahn, 1982) and has been used in the past as a tracer of mineral dust in the atmosphere (Barrie and Barrie, 1990; Malm et al., 1994; Balasubramanian et al., 2003; Quinn et al., 2004). The other set of filters were used to determine the concentration of Na^+ and Cl^- by ion chromatography (IC). These ions are major constituents of sea salts and have been used as a tracer of sea spray aerosol in the past (Malm et al., 1994; Quinn et al., 2002, 2004; Balasubramanian et al., 2003).

For ICP-AES analysis, the Teflon filters were digested in a heated ultrasonic bath after the addition of concentrated nitric and hydrochloric acids. The resulting solutions were then atomized into an argon plasma and the element Al was identified by a characteristic emission line. For IC analysis, the Teflon filters were immersed in 10 mL of deionized water and sonicated for 60 minutes. Concentrations of soluble ions were then determined by Ion Chromatography (Thermo Scientific ICS-500), following the United States Environmental Protection Agency (USEPA) methods 300.0 and 300.7 (USEPA, 1986; Pfaff, 1993). Briefly, the extracted solution was injected into an ion exchange column operating under high pressure, and the ions were separated by the ion exchange column and detected by conductivity of the post-column eluent.

4.2.7 Particle dispersion modelling

To help determine the possible sources of INPs in the samples, the FLEXible PARTicle dispersion model (FLEXPART) (Stohl, 2006) was used in the backward mode. The model was driven by the National Centers for Environmental Prediction (NCEP) Final (FNL) Operational Global Analysis Data. In each simulation, 100000 particles were released at the sampling site (82.5°N, 62.5°W) within one minute and followed backward for 7 days with outputs generated at

1-hour intervals. For each INP sample collected at Alert, a simulation was run every three hours during the sampling period. The outputs from all the simulations were then averaged to generate a potential emission sensitivity (PES) plot for each sample. Since we wanted to identify the sources of the INPs, which most likely originated from the Earth's surface, we only used data from the surface to 100 meters above the surface resulting in near-surface PES plots (i.e., footprint PES plots).

4.3 Results and Discussion

4.3.1 The concentrations of INPs measured at Alert

Here we only report the INP concentrations at $T \geq -22$ °C. We focus on this temperature range because, in some cases, all droplets froze when $T < -22$ °C (Fig. 4.3). In these cases, the concentration of INPs could not be calculated from Eq. 4.1. For $T \geq -22$ °C, the fraction of droplets that froze for the negative controls on average was $\leq 5\%$ (Fig. 4.3).

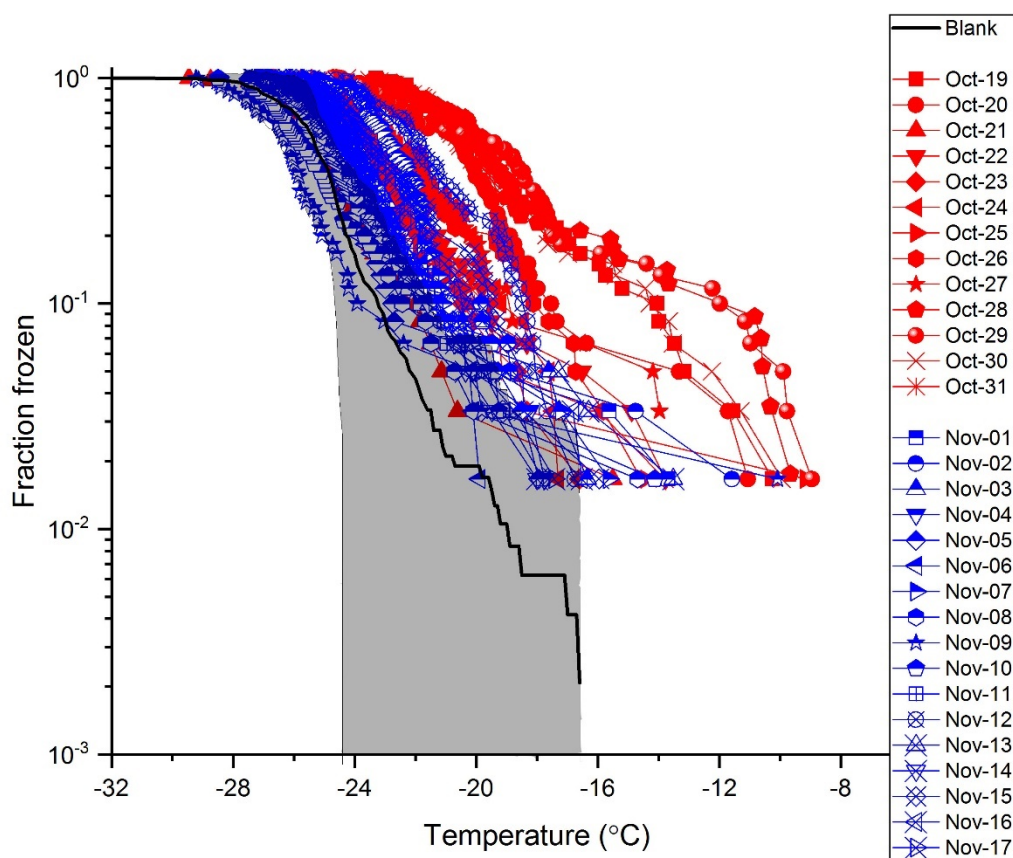


Figure 4.4: The fraction of frozen droplets for the 30 samples collected in the Arctic during October and November. Also included is the average of the blanks and two times the standard deviations of the blanks from the 8 trials. The black solid line is the average of the 8 trials and the shading region corresponds to two times the standard deviations of the blanks from the 8 trials.

Shown in Fig. 4.4a, are the measured INP concentrations for all the 30 samples separated by month. The lower detection limit for the INP measurements was approximately 0.01 L^{-1} for each sample. Within the temperature range investigated ($\geq -22 \text{ }^\circ\text{C}$), the measured INP concentrations for the October samples varied from 0.01 L^{-1} to 0.5 L^{-1} and the measured INP concentrations for the November samples varied from 0.01 L^{-1} to 0.2 L^{-1} . The largest variation of INP concentrations between daily samples occurred at $-22 \text{ }^\circ\text{C}$, with a factor of ~ 20 for the October

samples and a factor of ~ 8 for the November samples. In Fig. 4.4b, we compare the average INP concentrations with 83 % confidence bands for the October and November samples. Two data sets are statistically different at a confidence interval of 95 % if their 83 % confidence bands of the means do not overlap (Goldstein and Healy, 2009). The results in Fig. 4.4b show that the average INP concentrations during October were a factor of 3 to 6 higher than November and the differences were statistically significant at $T \geq -22$ °C.

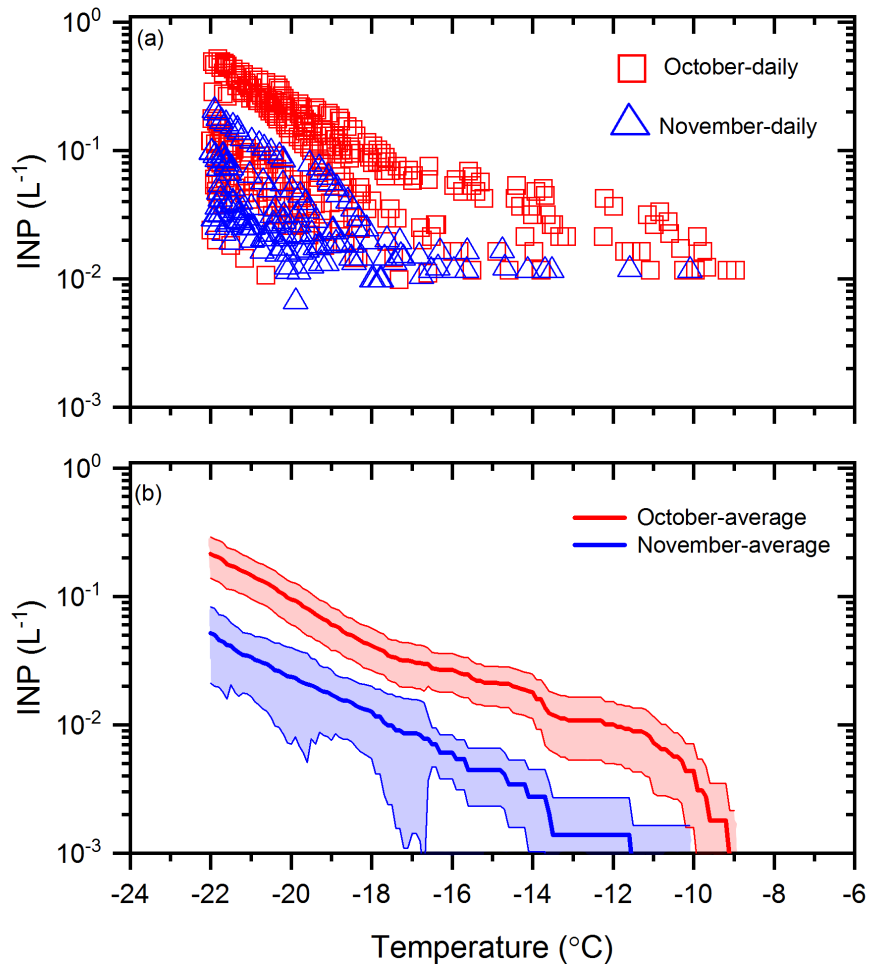


Figure 4.5: INP concentrations during October and November. Panel (a): The INP concentrations measured as a function of temperature for the daily samples collected in October and November. Panel (b): The monthly average INP concentrations as a function of temperature for the samples collected in October and November. The shading regions in panel (b) represent the 83% confidence bands of the monthly average INP concentrations. Two data sets with normal distributions are statistically different at a confidence interval of 95 % if their 83 % confidence bands of the means do not overlap (Goldstein and Healy, 2009).

Consistent with our results Wex et al. (2019) observed higher INP concentrations in the fall, and a lower concentration in the winter and spring at a freezing temperature of $-7^{\circ}C$. Studies

at other sites in the Arctic, have also observed higher INP concentrations in the summer and lower concentrations in the winter (Fountain and Ohtake, 1985; Wex et al., 2019).

Fig. 4.6 shows a comparison of the INP concentrations measured in our study to the INP concentrations measured in previous ground-based or ship-based INP measurements in the Arctic (The locations of previous field measurements are given in Table D.1 in Appendix D). The average INP concentrations at -16 °C and -22 °C in our study were 0.04 L⁻¹ and 0.22L⁻¹, respectively, for the October samples and 0.013 L⁻¹ and 0.052L⁻¹, respectively, for the November samples. These values were within the concentration range of the previous studies (Radke et al., 1976; Fountain and Ohtake, 1985; Bigg, 1996; Bigg and Leck, 2001; Conen et al., 2016; Mason et al., 2016; Creamean et al., 2018, 2019; Si et al., 2019; Wex et al., 2019; Irish, Hanna, Willis, et al., 2019; Šantl-Temkiv et al., 2019).

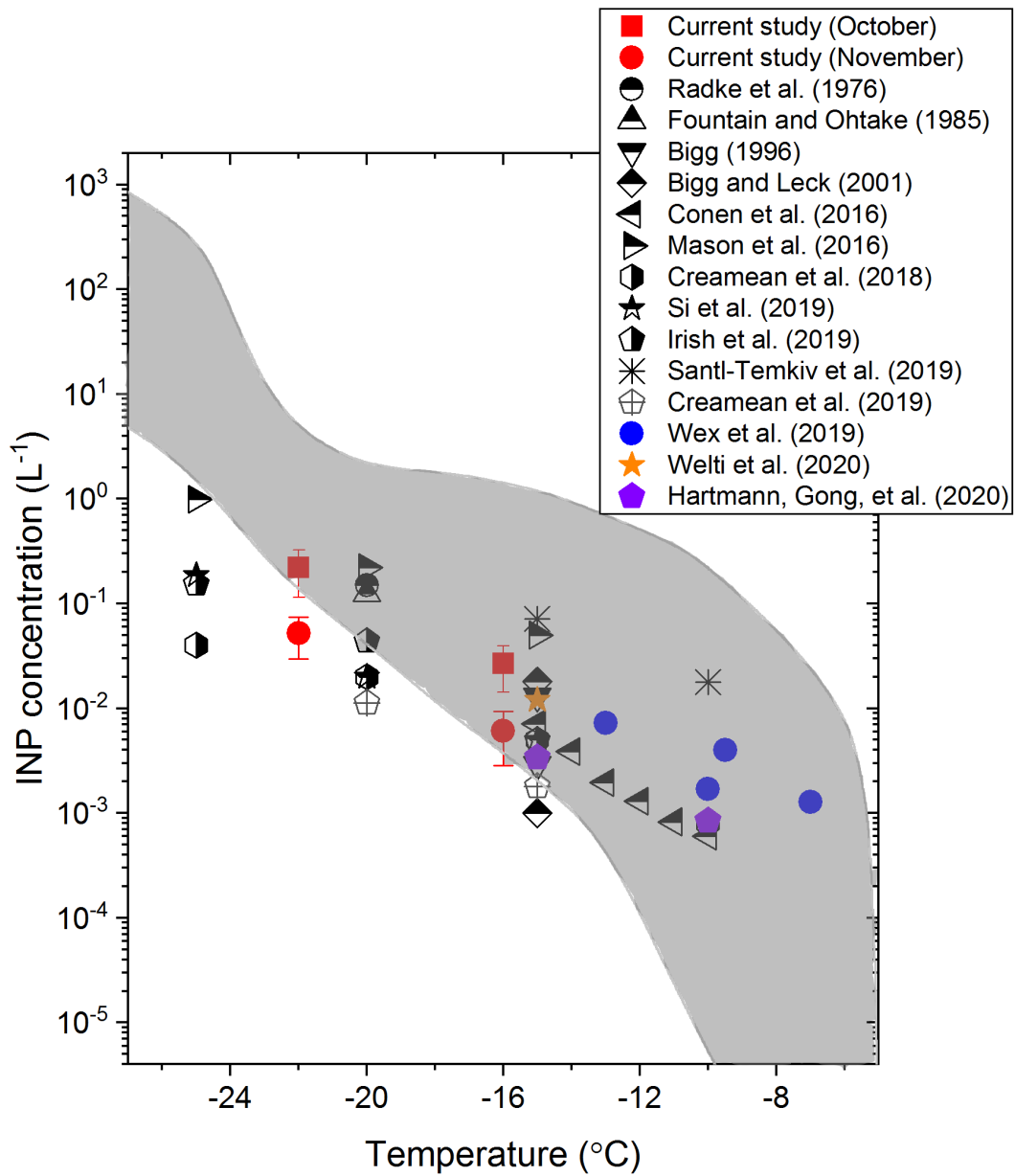


Figure 4.6: The average INP concentrations as a function of temperature in the Arctic measured in the current study and in previous ground-based or ship-based studies. The sampling platform, location, and time of each study is indicated in Table. D.1 (Appendix D). The error bars for the current study correspond to the 95% confidence intervals of the means. The region shaded in grey shows the literature data from Petters and Wright (2015) for precipitation and cloud water samples.

Also included in Fig. 4.6 (shaded region) is the range of INP concentrations measured from precipitation and cloud water samples, which were mainly collected over mid-latitudes in North America and Europe (Petters and Wright, 2015). Based on Fig. 4.6, $T \geq -16$ °C, the INP concentrations measured at the surface in Arctic are mostly consistent with the concentration range reported by Petters and Wright (2015). However, at $T < -16$ °C, the INP concentrations measured at the surface in the Arctic are often less than the concentration range reported by Petters and Wright (2015). These results suggest that INP concentrations at the surface in the Arctic may often be lower than those in mid-latitude continental areas at $T < -16$ °C, consistent with the previous conclusion in Wex et al. (2019) using a similar analysis.

4.3.2 Results from the ammonium sulfate assay

To determine if mineral dust particles are an important component of the INP population, we compared the INP concentrations before and after exposure to a 0.05 M ammonium sulfate solution (see Section 4.2.3). An increase in the INP concentrations after exposure to ammonium sulfate suggests the presence of mineral dust INPs. Shown in Fig. 4.7 are results for the October samples (Fig. 4.7a and Fig. 4.7b) and the November samples (Fig. 4.7c and 4.7d) before and after ammonium sulfate treatment. Fig. 4.7a and 4.7c show the daily measured INP concentrations before and after ammonium sulfate treatment, and Fig. 4.7b and 4.7d show the average values with 83% confidence intervals before and after ammonium sulfate treatment.

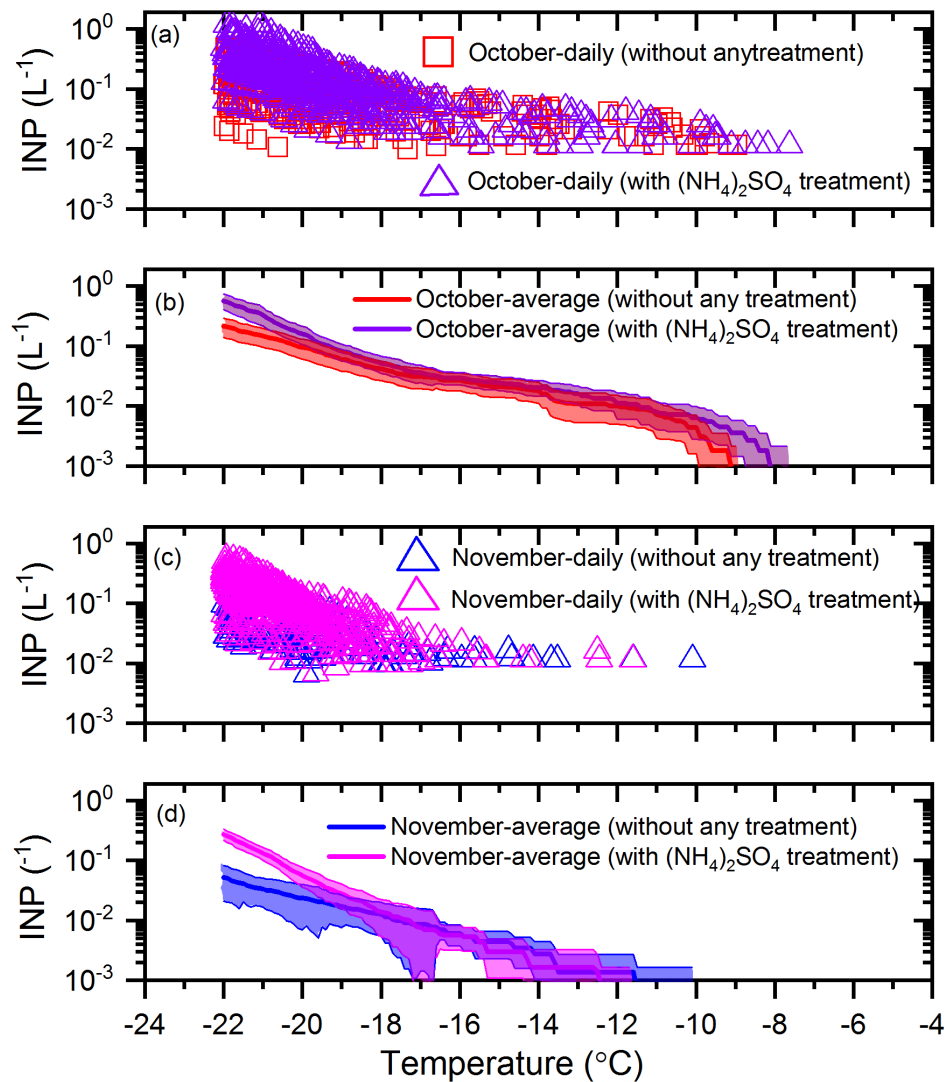


Figure 4.7: The effect of ammonium sulfate treatment on the INP concentrations. Panel (a): The daily INP concentrations measured in October without any treatment and with ammonium sulfate treatment. Panel (b): the monthly average INP concentrations for October without any treatment and with ammonium sulfate treatment. Panel (c): The daily INP concentrations in November without any treatment and with ammonium sulfate treatment. Panel (d): the monthly average INP concentrations for November without any treatment and with ammonium sulfate treatment. The shading regions in panel (b) and panel (d) indicate 83 % confidence bands. Two data sets with normal distributions are statistically different at a confidence interval of 95 % if their 83 % confidence bands of the means do not overlap (Goldstein and Healy, 2009).

For the October samples, the average INP concentrations after ammonium sulfate treatment were statistically higher (95% confidence level) than those before ammonium sulfate treatment for $T < -21$ °C. At -22 °C, the average INP concentrations for October were a factor of ~ 2.5 higher after ammonium sulfate treatment (Fig. 4.7b). For the November samples, the average INP concentrations after ammonium sulfate treatment were statistically higher (95% confidence level) than those before ammonium sulfate treatment for $T < -20$ °C. At -22 °C, the average INP concentrations for November were a factor of ~ 5 higher after ammonium sulfate treatment (Fig. 4.7d). These results suggest that mineral dust is a significant component of the INP population for October and November at $T < -21$ °C and $T < -20$ °C, respectively.

These findings are consistent with the previous studies that have identified mineral dust as an important component of the INP population in the Arctic (Kumai and Francis, 1962; Rogers et al., 2001; Prenni, Demott, et al., 2009). The ammonium sulfate treatment assay appears to be useful when determining the temperature range over which mineral dust is an important component in the INP population.

4.3.3 Results from the heat assay

To estimate the contribution of biological particles to the INP population of the samples, we determined the change in the INP concentrations after heating the samples at 100 °C (see Section 4.2.4). A decrease in the INP concentrations together with no significant increase in the INP concentrations when exposed to ammonium sulfate was assumed to indicate the presence of biological INPs. Shown in Fig. 4.8 are results for the October samples (Fig. 4.8a and Fig. 4.8b) and the November samples (Fig. 4.8c and Fig. 4.8d) before and after heat treatment.

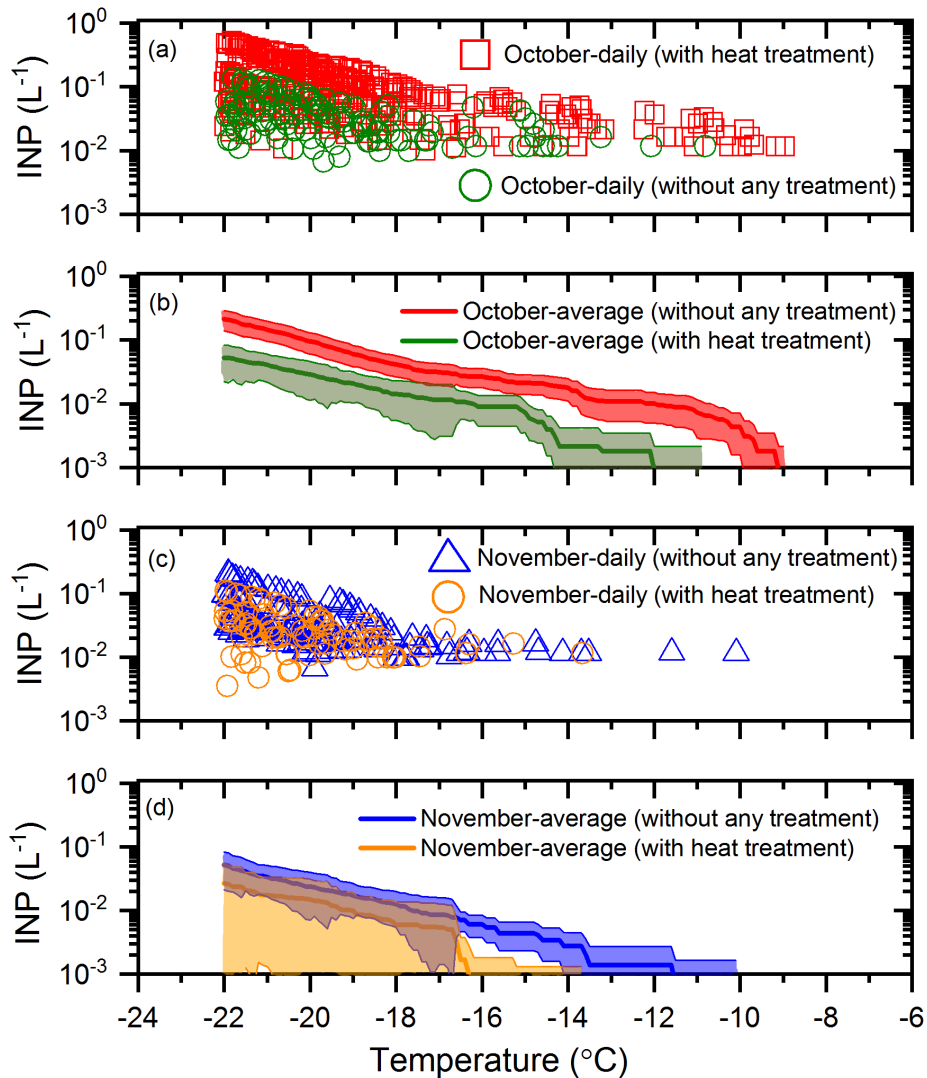


Figure 4.8: The effect of heat treatment on the INP concentrations. Panel (a): The daily INP concentrations measured in October without any treatment and with heat treatment. Panel (b): the monthly average INP concentrations for October without any treatment and with heat treatment. Panel (c): The daily INP concentrations in November without any treatment and with heat treatment. Panel (d): the monthly average INP concentrations for November without any treatment and with heat treatment. The shading regions in panel (b) and panel (d) indicate 83 % confidence bands. Two data sets with normal distributions are statistically different at a confidence interval of 95 % if their 83 % confidence bands of the means do not overlap (Goldstein and Healy, 2009).

For the October samples, the average INP concentrations after heat treatment were statistically lower (95% confidence level), at $T \geq -22$ °C (Fig. 4.8b). For the November samples, the average INP concentrations after heat treatment were statistically lower (95% confidence level) at $T \geq -16.5$ °C (Fig. 4.8d). In combination with the results from ammonium sulfate assay (Section 4.3.2), this suggests that a large fraction of the INPs were likely biological for the October and November samples at $T \geq -21$ °C and $T \geq -16.5$ °C, respectively, since heat decreased the INP concentrations and ammonium sulfate had no significant effect under these conditions.

A few recent studies have used heat treatment at approximately 100 °C to quantify the contribution of biological particles to the INP population in the Arctic (Šantl-Temkiv et al., 2019; Hartmann, Adachi, et al., 2020; Hartmann, Gong, et al., 2020). Šantl-Temkiv et al. (2019) showed that 82% to 100% of the INPs at $T \geq -15$ °C were likely biological for their samples collected over Greenland during the summer. Hartmann and Adachi et al. (2020) and Hartmann and Gong et al. (2020) showed that the 100% of the INPs at $T \geq -15$ °C were likely biological for some of their samples collected over the Arctic Ocean during the spring and early summer. In addition, other researchers have speculated that biological particles were an important source of INPs in the Arctic based on the warm freezing temperatures ($T > -15$ °C) of their samples (Conen et al., 2016; Creamean et al., 2018, 2019; Wex et al., 2019). Overall, our results provide additional evidence that biological INP can make up a significant fraction of the INP population in the Arctic, at least for certain times of the year.

4.3.4 Correlations between the concentrations of INPs and Al, Na⁺, and Cl⁻

In addition to measuring the concentrations of INPs, we measured the concentrations of tracer chemical species for mineral dust and sea spray aerosol. Al was used as a tracer for mineral dust (Barrie and Barrie, 1990; Malm et al., 1994; Balasubramanian et al., 2003; Quinn et al., 2004),

and the ions Na^+ and Cl^- were used as tracers for sea spray aerosols (Malm et al., 1994; Quinn et al., 2002, 2004; Balasubramanian et al., 2003). Table 4.1 shows the correlation coefficients between the concentrations of the tracer chemical species and the concentrations of INPs at freezing temperatures of $-22\text{ }^\circ\text{C}$ and $-16\text{ }^\circ\text{C}$.

Table 4.1: The correlation coefficients and p-values between the concentration of INPs at $-16\text{ }^\circ\text{C}$ and $-22\text{ }^\circ\text{C}$ and concentrations of Al, Na^+ , and Cl^- . Correlations that are statistically significant ($p < 0.05$) are bolded in red.

Correlations between INPs and tracer chemicals (n=30)				
Tracer chemicals	INPs at $-16\text{ }^\circ\text{C}$		INPs at $-22\text{ }^\circ\text{C}$	
	R	p	R	p
Al	0.58	3.4×10^{-4}	0.72	2.8×10^{-6}
Na^+	0.13	0.24	0.25	0.092
Cl^-	0.12	0.26	0.23	0.11

The concentration of Al was correlated ($R = 0.72$) with the INP concentrations at $-22\text{ }^\circ\text{C}$, and the correlation was statistically significant ($p < 0.05$). This is consistent with our finding that a significant fraction of the INP population at $-22\text{ }^\circ\text{C}$ contained mineral dust particles (see Section 4.3.2). At $-16\text{ }^\circ\text{C}$, the correlation coefficient was smaller ($R = 0.58$) but still statistically significant ($p < 0.05$). One possible explanation is that the biological INPs, which were important at the warmer temperatures, and the mineral dust INPs, which were important at lower temperatures in our samples, came from the same sources in some cases. It has been shown that aerosol particles from soil dust contain both biological and mineral dust INPs (Conen et al., 2011; O’Sullivan et al., 2015, 2016; Hill et al., 2016). Similar to our results, Si et al. (2019) found statistically significant and positive correlations between the concentrations of INPs at freezing temperatures of $-25\text{ }^\circ\text{C}$ and $-20\text{ }^\circ\text{C}$ and Al concentrations measured at Alert in the spring,

In contrast to Al, the correlation coefficients between concentrations of Na^+ and Cl^- and INP concentrations at freezing temperatures of $-22\text{ }^\circ\text{C}$ and $-16\text{ }^\circ\text{C}$ were small (≤ 0.25) and not

statistically significant ($p > 0.05$). Hence, the correlation analysis is not consistent with sea spray aerosols as a source of INPs during the sampling period. Related, Si et al. (2019) observed statistically significant negative correlations between the INPs at -25°C and sea spray aerosol tracers (Na^+ and Cl^-) at Alert in the spring.

4.3.5 Results from particle dispersion modelling

To provide additional information on the source regions of the INPs in our study, we calculated footprint potential emission sensitivity (PES) plots for each sample using FLEXPART run in the backward mode. The footprint PES plots show the residence time per 100000 particles in the layer from 0 to 100 m in altitude during the previous 7 days for each sample in the simulation. Fig. 6 shows the average footprint PES plot for all the 30 samples (Fig. 4.9a), the average footprint PES plot for the October samples (Fig. 4.9b), and the average footprint PES plot for the November samples (Fig. 4.9c). Based on the Fig. 4.9a-c, the collected aerosol particles in the layer from 0 to 100 m in altitude were constrained almost exclusively to latitudes $> 50^{\circ}\text{N}$ in the 7 days prior to sampling. In addition, the footprint PES plots for October are similar to those for November, although the footprint PES plots for October tend to have higher residence time over Northern Canada compared to those for November.

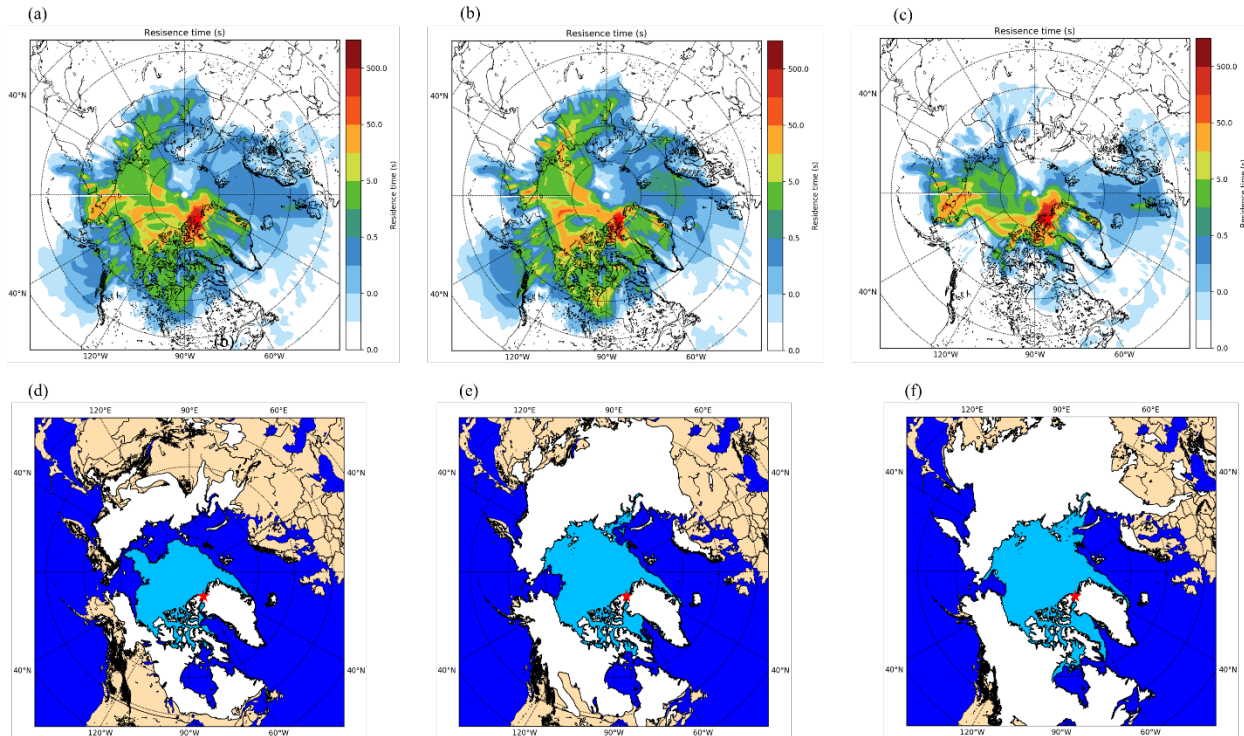


Figure 4.9: Panel (a): The average footprint PES plots for all the 30 samples collected in October and November. Panel (b): The average footprint PES plots for the samples collected in October. Panel (c): The average footprint PES plots for the samples collected in November. Panel (d): The map showing the surface coverage types on the first day of sampling (Oct-19). Panel (e): The map showing the surface coverage types at the midway point of sampling (Nov-03). Panel (f): The map showing the surface coverage types on the last day of sampling (Nov-17). In each panel, the sampling site is indicated by a red star. The surface coverage data was obtained from National Snow and Ice Data Center.

Shown in Fig. 4.9d – Fig. 4.9f are maps of the surface coverage types for October 19th, November 3rd, and November 17th, which correspond to the start, midway point, and end of the sampling period, respectively. Fig. 4.9d – Fig. 4.9f show that the snow coverage and sea-ice coverage largely increased during the field measurements, while the bare land and open ocean significantly decreases for latitudes $> 50^{\circ}\text{N}$. The footprint PES plots for each sample were combined with the maps of surface coverage types to determine the total residence time that each air mass sampled spent in the footprint layer over a specific surface type (Appendix D, Table D.2).

Shown in Table 4.2 are the correlations between these total residence times and INP concentrations at freezing temperatures of -22 °C and -16 °C. At freezing temperatures of -22 °C and -16 °C, statistically significant positive correlations ($R = 0.53$ and 0.49 , respectively) were observed between the INP concentrations and the residence time in the footprint layer over bare land. On the other hand, at the same freezing temperatures, statistically significant negative correlations ($R = -0.42$ and -0.39 , respectively) were observed between the INP concentrations and the residence time in the footprint layer over sea ice. In addition, no statistically significant correlations were observed between the INP concentrations and the residence time in the footprint layer over open ocean and land snow. These results, together with the results from the ammonium sulfate assay and the results from the correlation analysis between the concentrations of INPs and Al, Na^+ and Cl^- , strongly suggest that the INPs were most likely from bare land compared to the open ocean, sea ice, and land snow. Consistent with these results, Si et al. (2019) suggested that the INPs at -25 °C sampled at Alert in the spring were likely from terrestrial sources based on correlations between the concentrations of INPs and Al, Na^+ and Cl^- and particle dispersion modelling with FLEXPART. By contrast, Wex et al. (2019) suggested that the INPs at warm temperatures (> -15 °C) in the samples collected at Alert in the summer could come from both open land and open ocean based on the results of back trajectories calculated with the Hybrid Single-Particle Lagrangian Integrated Trajectory (HYSPLIT) model. The difference between our results and Wex et al. (2019) could be due to the different sampling times and differences in freezing temperatures of the INPs studied.

Table 4.2: The correlation coefficients and p-values between the concentration of INPs at -16 °C and -22 °C and the residence time of the air mass over different surface types within 0 – 100 m above the surface in the previous 7 days prior to sampling. Correlations that are statistically significant ($p < 0.05$) are bolded in red.

Correlations between INPs and residence time over different surface types (n=30)				
Surface coverage type	INPs at -16 °C		INPs at -22°C	
	R	p	R	p
Land	0.49	0.003	0.53	0.0011
Sea	0.038	0.42	-0.08	0.33
Sea ice	-0.39	0.016	-0.42	0.01
Snow	0.1	0.3	-0.1	0.3

4.4 Summary and Conclusions

In this study, we measured daily INP concentrations at Alert, a ground site in the Canadian high Arctic during October and November of 2018. The average INP concentrations were consistent with values from previous ground-based and ship-based INP measurements in the Arctic. Compared to the concentration range reported by Petters and Wright (2015), the average INP concentrations fell within this range at a warmer temperature (-16 °C) but were lower than this range at lower temperature (-22 °C), suggesting that the INPs in the Arctic could be lower than those in mid-latitude continents at -22 °C and lower temperatures.

We used an ammonium sulfate assay and a heat assay to evaluate the importance of mineral dust INPs and biological INPs in the Arctic. The results from the ammonium sulfate assay suggest that mineral dust was an important component of the INP population for the October samples and November samples at $T < -21$ °C and $T < -20$ °C, respectively. The results from the heat assay suggest that a large fraction of the INPs were likely biological for the October samples and November samples at $T \geq -21$ °C and $T \geq -16.5$ °C.

We also measured the concentrations of Al, Na⁺, and Cl⁻ for the same sampling period as the INP samples. At the freezing temperatures of -16 °C and -22 °C, we found statistically significant correlations between the concentrations of INPs and Al but not Na⁺ and Cl⁻, consistent with mineral dust as an important component of the INP population while sea spray aerosols were not likely a source of the INPs.

Finally, to help constrain the source regions of INPs, FLEXPART was used to generate footprint PES plots showing the residence time per 100000 particles in the footprint layer in 7 days prior to sampling. The results suggest that the collected aerosol particles were most likely associated with latitudes > 50 °N. Using these PES plots and surface coverage data, we also calculated the residence time the airmasses spent over each surface type. At the freezing temperatures of -16 °C and -22 °C, statistically significant positive correlations were found between the INP concentrations and the residence time the airmass spent over bare land, while statistically negative correlations were found between the INP concentrations and the residence time the airmass spent over sea ice. These results, together with the results from the ammonium sulfate assay and the correlation analysis between INPs and Al, Na⁺, and Cl⁻, strongly suggest that the INPs were likely from open land at latitudes > 50 °N rather than oceanic sources.

Due to global warming, the coverage of sea ice, land snow, and permafrost at high latitudes is decreasing and lasting for shorter periods of the year. As a result, the fluxes of INPs to the Arctic atmosphere are likely experiencing a significant change and need more investigation. Our results here provide additional information on the concentrations, composition, and sources of Arctic INPs. However, our measurements only spanned for 30 days from October to November. More measurements at the same site are needed to evaluate the influences of change of surface coverage

type on the Arctic INPs. More modelling studies are needed to understand how the change will affect the climate in the Arctic.

Chapter 5 Conclusions and Future Work

5.1 The effect of solutes on the immersion freezing of mineral dust

During atmospheric transport, mineral dust particles can be coated with water-soluble coatings, which can alter the ice nucleating ability of mineral dust particles. Motivated by this, Chapter 2 and Chapter 3 investigate the effect of alkali salts, inorganic acids, carboxylic acids, and polyols on the immersion freezing of K-rich feldspar using the droplet freezing technique. K-rich feldspar was selected as a proxy for atmospheric dust because it has a better ice nucleating ability compared to other minerals and has been used in models to predict atmospheric INP concentrations (Atkinson et al., 2013; Vergara-Temprado et al., 2017).

Chapter 2 focuses on the effect of a series of alkali nitrates at concentrations of 5×10^{-5} M to 5×10^{-3} M, thus isolating the effect of alkali cations. The results show that only K^+ increased the median freezing temperatures of the droplets, while the other alkali cations either had no effect or decreased the median freezing temperatures of the droplets. The changes in the median freezing temperatures caused by the alkali cations followed the order $K^+ \geq Li^+ \geq Na^+ \geq Rb^+ \geq Cs^+$. Using cryo-XPS, the surface composition of K-rich feldspar in the presence of the alkali cations was also determined. The atomic ratio K/Al at the surface of K-rich feldspar was positively correlated with the changes in median freezing temperatures due to the alkali cations except for Cs^+ . A possible explanation for this correlation is that the atomic ratio K/Al is an indicator of the abundance of certain types of K-bearing microcline surfaces that drive the immersion freezing of K-rich feldspar, while Cs^+ likely influences the immersion freezing of K-rich feldspar by an additional mechanism, possibly blocking ice nucleating active sites by adsorption. In addition, Chapter 2 shows that the

cation charge density of alkali cations cannot explain their effect on the ice nucleation properties of K-rich feldspar.

Chapter 3 studies the effect of two inorganic acids (HCl and HNO₃), two polyols (levoglucosan and glycerol), and several carboxylic acids at concentrations of 5×10^{-5} M to 5×10^{-3} M using similar experimental methods as in Chapter 2. The results show that the inorganic acids and carboxylic acids decreased the median freezing temperatures of the droplets by up to 7 °C, while the polyols had no significant effect on the median freezing temperatures. The change in median freezing temperatures by the inorganic acids and carboxylic acids was a strong function of the pH of the droplets, with the median freezing temperatures decreasing as the pH decreased. The decrease in the ice nucleating ability of K-rich feldspar due to the carboxylic acids was only related to the pH of the droplets rather than the type of carboxylic acid and possible complex formation between the K-rich feldspar and the carboxylic acids. Based on the determined surface composition of K-rich feldspar exposed to different pH, we showed that the decrease in the ice nucleating ability of K-rich feldspar by inorganic acids and carboxylic acids was likely due to H₃O⁺ and parent K⁺ ion exchange and the incongruent dissolution of Al with respect to Si at the K-rich feldspar surface.

5.2 Investigation on atmospheric INPs in the Arctic

In addition to laboratory studies of INPs, in Chapter 4 we investigate the concentrations, composition, and sources of INPs in the Arctic.

The field campaign was conducted at Alert, Nunavut, Canada in October and November of 2018. Daily concentrations of INPs and tracer species Al, Na⁺, and Cl⁻ were monitored during the sampling period. The results show that the average INP concentrations in October were

statistically higher than those in November, which is consistent with findings from other studies (Fountain and Ohtake, 1985; Wex et al., 2019) that the INP concentrations in the Arctic decreased from the summer to the winter. An ammonium sulfate assay and a heat assay were used to identify mineral dust and biological INPs. The results from these two assays show that mineral dust was likely an important component of the INPs at $T < -21$ °C and $T < -20$ °C for the October samples and November samples, respectively. A large fraction of the INPs was likely biological at $T > -21$ °C and $T > -16$ °C for the October samples and November samples, respectively. In addition, we observed a statistically significant correlation between INPs and Al but not Na^+ and Cl^- , consisting with the INPs containing mineral dust. To investigate the source regions of the INPs, we used FLEXPART to calculate time the airmasses spent over different regions in the 7 days prior to sampling. The results show that the airmasses were constrained to latitudes $> 50^\circ\text{N}$. Moreover, we observed a positive correlation between the INPs and the time the airmasses spent over bare land and a negative correlation between the INPs and the time the airmasses spent over sea ice. These results, together with the correlation analysis, indicate that the INPs were likely from bare land at latitudes $> 50^\circ\text{N}$.

5.3 Outlook

Chapter 2 and Chapter 3 discuss one type of mineral dust, K-rich feldspar, exposed to different solutes. However, atmospheric mineral dust is typically composed of a complex mixture of feldspars, clays, quartz, calcite, and metal oxides/hydroxides. Studies on the effect of solutes on more types of mineral dusts in the future can help constrain the ice nucleation properties of mineral dust in the atmosphere and improve our understanding of the mechanisms for the effect of solutes on the ice nucleating ability of mineral dust.

In addition, we studied individual solutes on the immersion freezing of K-rich feldspar. However, different types of solutes including inorganics and organics can be present in cloud droplets containing mineral dust simultaneously. The effect of mixtures of different solutes may be non-additive and different from the effect of individual solutes. Studies focusing on the effect of solute mixtures on the ice nucleating ability of mineral dust are needed in the future.

There have also been other studies (Burkert-Kohn et al., 2017; Kumar et al., 2018; Whale et al., 2018; Perkins et al., 2020) investigating the effect of sodium salts, potassium salts, and inorganic acids on the ice nucleating ability of K-rich feldspar. As discussed in Chapter 2 and Chapter 3, the differences between our results and other studies could be due to different freezing temperatures probed, different exposure times, and different sources of K-rich feldspar. More experiments investigating the effect of solutes on the ice nucleating ability of different K-rich feldspar samples with a longer exposure time and lower freezing temperatures are needed in the future.

In Chapter 4 we report daily INP concentrations at Alert, Nunavut, Canada for 30 days from October to November in 2018 and show that the INPs were likely from terrestrial sources at high latitudes. Studies have shown that warming in the Arctic will lead to less land snow and more exposed land, thus possibly providing additional sources of INPs in the Arctic. In the future, long-term INP measurements at the same site in the same season will improve our understanding of how the change in land snow affects the fluxes of INPs in the Arctic. Related to this, more modelling studies are needed to understand how the change of INPs in the Arctic will affect the climate of the region.

In addition, in Chapter 4 we use an ammonium sulfate assay to distinguish mineral dust INPs from other components in the samples. This is the first time that this assay has been used to

identify mineral dust INPs in fields samples. Nevertheless, additional experiments are needed to fully validate the ammonium sulfate assay, and additional field studies using the ammonium sulfate assay would be interesting.

References

Abdelmonem, A. et al. (2017) ‘Surface-charge-induced orientation of interfacial water suppresses heterogeneous ice nucleation on α -alumina (0001)’, *Atmospheric Chemistry and Physics*, 17(12), pp. 7827–7837. doi: 10.5194/acp-17-7827-2017.

Alpert, P. A., Aller, J. Y. and Knopf, D. A. (2011) ‘Ice nucleation from aqueous NaCl droplets with and without marine diatoms’, *Atmospheric Chemistry and Physics*, 11(3), pp. 8291–8336. doi: 10.5194/acpd-11-8291-2011.

Alpert, Peter A., Aller, J. Y. and Knopf, D. A. (2011) ‘Initiation of the ice phase by marine biogenic surfaces in supersaturated gas and supercooled aqueous phases’, *Physical Chemistry Chemical Physics*, 13(44), pp. 19882–19894. doi: 10.1039/c1cp21844a.

Ansmann, A. et al. (2009) ‘Evolution of the ice phase in tropical altocumulus: SAMUM lidar observations over Cape Verde’, *Journal of Geophysical Research Atmospheres*, 114(17), pp. 1–20. doi: 10.1029/2008JD011659.

Atkins, P. and Paula, J. De (2009) *Physical Chemistry, 9th Edition*. W.H. Freeman.

Atkinson, J. D. et al. (2013) ‘The importance of feldspar for ice nucleation by mineral dust in mixed-phase clouds’, *Nature.*, 498(7454), pp. 355–358. doi: 10.1038/nature12278.

Augustin-Bauditz, S. et al. (2014) ‘The immersion mode ice nucleation behavior of mineral dusts: A comparison of different pure and surface modified dusts’, *Geophysical Research Letters*, 41(20), pp. 7375–7382. doi: 10.1002/2014GL061317.

Axe, K. and Persson, P. (2001) ‘Time-dependent surface speciation of oxalate at the water-

boehmite (γ -AlOOH) interface: Implications for dissolution', *Geochimica et Cosmochimica Acta*, 65(24), pp. 4481–4492. doi: 10.1016/S0016-7037(01)00750-5.

Bailey, S. W. (1969) 'Refinement of an intermediate microcline structure', *American Mineralogist*, 54(11–12), pp. 1540–1545.

Balasubramanian, R. et al. (2003) 'Comprehensive characterization of PM_{2.5} aerosols in Singapore', *Journal of Geophysical Research D: Atmospheres.*, 108(D16), pp. 1-17

Barrie, L. A. (1985) 'Five Years of Air Chemistry Observations In The Canadian Arctic', *Atmospheric Environment*, 19(12), pp. 1995–2010.

Barrie, L. A. and Barrie, M. J. (1990) 'Chemical components of lower tropospheric aerosols in the high arctic: Six years of observations', *Journal of Atmospheric Chemistry*, 11(3), pp. 211–226. doi: 10.1007/BF00118349.

Bigg, E. K. (1996) 'Ice forming nuclei in the high Arctic', *Tellus B: Chemical and Physical Meteorology*, 48(2) pp. 223–233.

Bigg, E. K. and Leck, C. (2001) 'Cloud-active particles over the central Arctic Ocean', *Journal of Geophysical Research Atmospheres*, 106(D23), pp. 32155–32166. doi: 10.1029/1999JD901152.

Bond, T. C. et al. (2013) 'Bounding the role of black carbon in the climate system: A scientific assessment', *Journal of Geophysical Research Atmospheres*, 118(11), pp. 5380–5552. doi: 10.1002/jgrd.50171.

Boose, Y., Welti, A., et al. (2016) 'Heterogeneous ice nucleation on dust particles sourced from nine deserts worldwide - Part 1: Immersion freezing', *Atmospheric Chemistry and Physics*, 16(23), pp. 15075–15095. doi: 10.5194/acp-16-15075-2016.

Boose, Y., Sierau, B., et al. (2016) ‘Ice nucleating particles in the Saharan Air Layer’, *Atmospheric Chemistry and Physics*, 16(14), pp. 9067–9087. doi: 10.5194/acp-16-9067-2016.

Bowers, R. M. et al. (2009) ‘Characterization of airborne microbial communities at a high-elevation site and their potential to act as atmospheric ice nuclei’, *Applied and Environmental Microbiology*, 75(15), pp. 5121–5130. doi: 10.1128/AEM.00447-09.

Burkert-Kohn, M. et al. (2017) ‘Leipzig Ice Nucleation chamber Comparison (LINC): Intercomparison of four online ice nucleation counters’, *Atmospheric Chemistry and Physics*, 17(18), pp. 11683–11705. doi: 10.5194/acp-17-11683-2017.

Chardon, E. S., Livens, F. R. and Vaughan, D. J. (2006) ‘Reactions of feldspar surfaces with aqueous solutions’, *Earth-Science Reviews*, 78(1–2), pp. 1–26. doi: 10.1016/j.earscirev.2006.03.002.

Chen, T., Rossow, W. B. and Zhang, Y. (2000) ‘Radiative effects of cloud-type variations’, *Journal of Climate*, 13(1), pp. 264–286. doi: 10.1175/1520-0442(2000)013<0264:REOCTV>2.0.CO;2.

Christner, B. C. et al. (2008) ‘Geographic, seasonal, and precipitation chemistry influence on the abundance and activity of biological ice nucleators in rain and snow’, *Proceedings of the National Academy of Sciences.*, 108(48), pp. 18854–18859, doi: 10.1073/pnas.0809816105.

Clegg, S. L., Seinfeld, J. H. and Brimblecombe, P. (2001) ‘Thermodynamic modelling of aqueous aerosols containing electrolytes and dissolved organic compounds’, *Journal of Aerosol Science*, 32(6), pp. 713–738. doi: 10.1016/S0021-8502(00)00105-1.

Cohen, J. et al. (2014) ‘Recent Arctic amplification and extreme mid-latitude weather’, *Nature*

Geoscience., 7, pp. 627-637, doi: 10.1038/ngeo2234.

Collins, K. D. (1997) 'Charge density-dependent strength of hydration and biological structure', *Biophysical Journal*. 72(1), pp. 65–76. doi: 10.1016/S0006-3495(97)78647-8.

Conen, F. et al. (2011) 'Biological residues define the ice nucleation properties of soil dust', *Atmospheric Chemistry and Physics.*, 11(18), pp. 9643-9648, doi: 10.5194/acp-11-9643-2011.

Conen, F., Stopelli, E. and Zimmermann, L. (2016) 'Clues that decaying leaves enrich Arctic air with ice nucleating particles', *Atmospheric Environment.*, 129, pp. 91–94. doi: 10.1016/j.atmosenv.2016.01.027.

Constantinidou, H. A. et al. (1990) 'Atmospheric Dispersal of Ice Nucleation-Active Bacteria: The Role of Rain', *Phytopathology*, 80, pp. 934–937.

Cook, R. D. et al. (2017) 'Biogenic, urban, and wildfire influences on the molecular composition of dissolved organic compounds in cloud water', *Atmospheric Chemistry and Physics*, 17(24), pp. 15167–15180. doi: 10.5194/acp-17-15167-2017.

Creamean, J. M. et al. (2018) 'Marine and terrestrial influences on ice nucleating particles during continuous springtime measurements in an Arctic oilfield location', *Atmospheric Chemistry and Physics*, 18(24), pp. 18023–18042. doi: 10.5194/acp-18-18023-2018.

Creamean, J. M. et al. (2019) 'Ice Nucleating Particles Carried From Below a Phytoplankton Bloom to the Arctic Atmosphere', *Geophysical Research Letters*, 46(14), pp. 8572–8581. doi: 10.1029/2019GL083039.

Cziczo, D. J. et al. (2004) 'Single particle measurements of the chemical composition of cirrus ice residue during CRYSTAL-FACE', *Journal of Geophysical Research: Atmospheres*, 109(4), pp.

1–13. doi: 10.1029/2003jd004032.

Cziczo, D. J. et al. (2009) ‘Deactivation of ice nuclei due to atmospherically relevant surface coatings’, *Environmental Research Letters*, 4(4), pp. 1–9. doi: 10.1088/1748-9326/4/4/044013.

Cziczo, D. J. et al. (2013) ‘Clarifying the dominant sources and mechanisms of cirrus cloud formation’, *Science*, 340(6138), pp. 1320–1324. doi: 10.1126/science.1234145.

David, R. O. et al. (2019) ‘Pore condensation and freezing is responsible for ice formation below water saturation for porous particles’, *Proceedings of the National Academy of Sciences*, 116(17), pp. 8184–8189. doi: 10.1073/pnas.1813647116.

Decesari, S. et al. (2000) ‘Characterization of water-soluble organic compounds in atmospheric aerosol: A new approach’, *Journal of Geophysical Research Atmospheres*, 105(D1), pp. 1481–1489. doi: 10.1029/1999JD900950.

DeMott, P. J. et al. (2003) ‘Measurements of the concentration and composition of nuclei for cirrus formation’, *Proceedings of the National Academy of Sciences*, 100(25), pp. 14655–14660. doi: 10.1073/pnas.2532677100.

DeMott, P. J. et al. (2010) ‘Predicting global atmospheric ice nuclei distributions and their impacts on climate’, *Proceedings of the National Academy of Sciences*, 107(25), pp. 11217–11222. doi: 10.1073/pnas.0910818107.

DeMott, P. J. et al. (2017) ‘Comparative measurements of ambient atmospheric concentrations of ice nucleating particles using multiple immersion freezing methods and a continuous flow diffusion chamber’, *Atmospheric Chemistry and Physics*, 17(18), pp. 11227–11245. doi: 10.5194/acp-17-11227-2017.

Derksen, C. and Brown, R. (2012) ‘Spring snow cover extent reductions in the 2008-2012 period exceeding climate model projections’, *Geophysical Research Letters*, 39(19), pp. 1–6. doi: 10.1029/2012GL053387.

Després, V. R. et al. (2012) ‘Primary biological aerosol particles in the atmosphere: A review’, *Tellus, Series B: Chemical and Physical Meteorology*, 64(1). doi: 10.3402/tellusb.v64i0.15598.

Diehl, K. et al. (2002) ‘The ice nucleating ability of pollen: Part II. Laboratory studies in immersion and contact freezing modes’, *Atmospheric Research*, 61(2), pp. 125–133. doi: 10.1016/S0169-8095(01)00132-6.

Diehl, K., Simmel, M. and Wurzler, S. (2006) ‘Numerical sensitivity studies on the impact of aerosol properties and drop freezing modes on the glaciation, microphysics and dynamics of clouds’, *Journal of Geophysical Research Atmospheres*, 111(7), pp. 1–15. doi: 10.1029/2005JD005884.

Diehl, K. and Wurzler, S. (2010) ‘Air parcel model simulations of a convective cloud: Bacteria acting as immersion ice nuclei’, *Atmospheric Environment*, 44(36), pp. 4622–4628. doi: 10.1016/j.atmosenv.2010.08.003.

van der Does, M. et al. (2018) ‘The mysterious long-range transport of giant mineral dust particles’, *Science Advances*, 4(12), pp. 1–9. doi: 10.1126/sciadv.aau2768.

Duce, R. A. et al. (1980) ‘Long-range atmospheric transport of soil dust from Asia to the tropical North Pacific: Temporal variability’, *Science*, 209(4464), pp. 1522–1524. doi: 10.1126/science.209.4464.1522.

Eastwood, M. L. et al. (2008) ‘Ice nucleation on mineral dust particles: Onset conditions,

nucleation rates and contact angles’, *Journal of Geophysical Research Atmospheres*, 113(22), pp. 1–9. doi: 10.1029/2008JD010639.

Eldering, A. M. et al. (1991) ‘Hydrochloric acid: A regional perspective on concentrations and formation in the atmosphere of Southern California’, *Atmospheric Environment Part A, General Topics*, 25(10), pp. 2091–2102. doi: 10.1016/0960-1686(91)90086-M.

Falkovich, A. H. (2004) ‘Adsorption of organic compounds pertinent to urban environments onto mineral dust particles’, *Journal of Geophysical Research*, 109(D2), pp. 1–19. doi: 10.1029/2003jd003919.

Field, P. R. et al. (2006) ‘Some ice nucleation characteristics of Asian and Saharan desert dust’, *Atmospheric Chemistry and Physics*, 6(10), pp. 2991–3006. doi: 10.5194/acp-6-2991-2006.

Finlayson-Pitts, B. and Pitts, J. J. (1999) *Chemistry of the Upper and Lower Atmosphere, Theory, Experiments, and Applications*. San Diego: Academic Press.

Fountain, A. G. and Ohtake, T. (1985) ‘Concentrations and Source Areas of Ice Nuclei in the Alaskan Atmosphere’, *Journal of Climate and Applied Meteorology*, pp. 377–382. doi: 10.1175/1520-0450(1985)024<0377:casaoi>2.0.co;2.

Fröhlich-Nowoisky, J. et al. (2015) ‘Ice nucleation activity in the widespread soil fungus *Mortierella alpina*’, *Biogeosciences*, 12(4), pp. 1057–1071. doi: 10.5194/bg-12-1057-2015.

Fuzzi, S. et al. (2001) ‘A simplified model of the water soluble organic component of atmospheric aerosols’, *Geophysical Research Letters*, 28(21), pp. 4079–4082.

Garcia, E. et al. (2012) ‘Biogenic ice nuclei in boundary layer air over two U.S. high plains agricultural regions’, *Journal of Geophysical Research Atmospheres*, 117(17), pp. 1–12. doi:

10.1029/2012JD018343.

Gautier, J. M., Oelkers, E. H. and Schott, J. (1994) 'Experimental study of K-feldspar dissolution rates as a function of chemical affinity at 150°C and pH 9', *Geochimica et Cosmochimica Acta*, 58(21), pp. 4549–4560. doi: 10.1016/0016-7037(94)90190-2.

Gieré, R. and Querol, X. (2010) 'Solid particulate matter in the atmosphere', *Elements*, 6(4), pp. 215–222. doi: 10.2113/gselements.6.4.215.

Gioda, A. et al. (2011) 'Speciation of water-soluble inorganic, organic, and total nitrogen in a background marine environment: Cloud water, rainwater, and aerosol particles', *Journal of Geophysical Research Atmospheres*, 116(D5), pp. 1–17. doi: 10.1029/2010JD015010.

Goldstein, H. and Healy, M. J. R. (2009) 'The Graphical Presentation of a Collection of Means', *Royal Statistical Society*, 158(1), pp. 175–177. doi: 10.2307/2983411.

Graham, B. et al. (2002) 'Water-soluble organic compounds in biomass burning aerosols over Amazonia 1. Characterization by NMR and GC-MS', *Journal of Geophysical Research Atmospheres*, 107(D20), p. LBA 14-1-LBA 14-16. doi: 10.1029/2001JD000336.

Grützun, V., Knoth, O. and Simmel, M. (2008) 'Simulation of the influence of aerosol particle characteristics on clouds and precipitation with LM-SPECS: Model description and first results', *Atmospheric Research*. 90(2–4), pp. 233–242. doi: 10.1016/j.atmosres.2008.03.002.

Gülgönül, İ. et al. (2012) 'Interaction of sodium ions with feldspar surfaces and its effect on the selective separation of Na- and K-feldspars', *Mineral Processing and Extractive Metallurgy Review*, 33(4), pp. 233–245. doi: 10.1080/08827508.2011.562952.

Harrison, A. D. et al. (2016) 'Not all feldspars are equal: A survey of ice nucleating properties

across the feldspar group of minerals’, *Atmospheric Chemistry and Physics*, 16(17), pp. 10927–10940. doi: 10.5194/acp-16-10927-2016.

Hartmann, D. L., Ockert-Bell, M. E. and Michelsen, M. L. (1992) ‘The Effect of Cloud Type on Earth’s Energy Balance: Global Analysis’, *Journal of Climate*, 5(11), pp. 1281–1304. doi: [https://doi.org/10.1175/1520-0442\(1992\)005<1281:TEOCTO>2.0.CO;2](https://doi.org/10.1175/1520-0442(1992)005<1281:TEOCTO>2.0.CO;2).

Hartmann, M., Gong, X., et al. (2020) ‘Terrestrial or marine? – Indications towards the origin of Ice Nucleating Particles during melt season in the European Arctic up to 83.7° N’, *Atmospheric Chemistry and Physics Discussions*. pp. 1–35. doi: 10.5194/acp-2020-1211.

Hartmann, M., Adachi, K., et al. (2020) ‘Wintertime Airborne Measurements of Ice Nucleating Particles in the High Arctic: A Hint to a Marine, Biogenic Source for Ice Nucleating Particles’, *Geophysical Research Letters*, 47(13). doi: 10.1029/2020GL087770.

Hawkins, L. N. et al. (2010) ‘Carboxylic acids, sulfates, and organosulfates in processed continental organic aerosol over the southeast Pacific Ocean during VOCALS-REx 2008’, *Journal of Geophysical Research Atmospheres*, 115(13), pp. 1–16. doi: 10.1029/2009JD013276.

Haynes, W. M., Lide, D. R. and Bruno, T. J. (2014) *CRC Handbook of Chemistry and Physics, CRC Handbook of Chemistry and Physics, 95th Edition*. doi: 10.1201/b17118.

He, H. et al. (2014) ‘Mineral dust and NO_x promote the conversion of SO₂ to sulfate in heavy pollution days’, *Scientific Reports*, 4(2), pp. 1–6. doi: 10.1038/srep04172.

Hellmann, R. et al. (2012) ‘Unifying natural and laboratory chemical weathering with interfacial dissolution-precipitation: A study based on the nanometer-scale chemistry of fluid-silicate interfaces’, *Chemical Geology*. 294–295, pp. 203–216. doi: 10.1016/j.chemgeo.2011.12.002.

- Hendricks, J., Krcher, B. and Lohmann, U. (2011) ‘Effects of ice nuclei on cirrus clouds in a global climate model’, *Journal of Geophysical Research Atmospheres*, 116(18), pp. 1–24. doi: 10.1029/2010JD015302.
- Hill, T. C. J. et al. (2016) ‘Sources of organic ice nucleating particles in soils’, *Atmospheric Chemistry and Physics*, 16(11), pp. 7195–7211. doi: 10.5194/acp-16-7195-2016.
- Hinz, K. P. et al. (2005) ‘Aerosol single particle composition at the Jungfraujoch’, *Journal of Aerosol Science*, 36(1), pp. 123–145. doi: 10.1016/j.jaerosci.2004.08.001.
- Hiranuma, N. et al. (2015) ‘A comprehensive laboratory study on the immersion freezing behavior of illite NX particles: A comparison of 17 ice nucleation measurement techniques’, *Atmospheric Chemistry and Physics*, 15(5), pp. 2489–2518. doi: 10.5194/acp-15-2489-2015.
- Hoose, Corinna et al. (2010) ‘A classical-theory-based parameterization of heterogeneous ice nucleation by mineral dust, soot, and biological particles in a global climate model’, *Journal of the Atmospheric Sciences*, 67(8), pp. 2483–2503. doi: 10.1175/2010JAS3425.1.
- Hoose, C., Kristjánsson, J. E. and Burrows, S. M. (2010) ‘How important is biological ice nucleation in clouds on a global scale?’, *Environmental Research Letters*, 5(2). doi: 10.1088/1748-9326/5/2/024009.
- Hoose, C. and Möhler, O. (2012) *Heterogeneous ice nucleation on atmospheric aerosols: A review of results from laboratory experiments*, *Atmospheric Chemistry and Physics*. 12(20), pp. 9817–9854 doi: 10.5194/acp-12-9817-2012.
- Hummel, M. et al. (2018) ‘Simulating the influence of primary biological aerosol particles on clouds by heterogeneous ice nucleation’, *Atmospheric Chemistry and Physics*, 18(20), pp. 15437–

15450. doi: 10.5194/acp-18-15437-2018.

IPCC (2013) ‘Summary for Policymakers. In: Climate Change 2013: The Physical Science Basis. Contribution of Working Group I to the Fifth Assessment Report of the Intergovernmental Panel on Climate Change’, *CEUR Workshop Proceedings*. doi: 10.1017/CBO9781107415324.004.

Irish, V. E. et al. (2017) ‘Ice-nucleating particles in Canadian Arctic sea-surface microlayer and bulk seawater’, *Atmospheric Chemistry and Physics*, 17(17), pp. 10583–10595. doi: 10.5194/acp-17-10583-2017.

Irish, V. E., Hanna, S. J., Willis, M. D., et al. (2019) ‘Ice nucleating particles in the marine boundary layer in the Canadian Arctic during summer 2014’, *Atmospheric Chemistry and Physics*, 19(2), pp. 1027–1039. doi: 10.5194/acp-19-1027-2019.

Irish, V. E., Hanna, S. J., Xi, Y., et al. (2019) ‘Revisiting properties and concentrations of ice-nucleating particles in the sea surface microlayer and bulk seawater in the Canadian Arctic during summer’, *Atmospheric Chemistry and Physics*, 19(11), pp. 7775–7787. doi: 10.5194/acp-19-7775-2019.

Jung, J. and Kawamura, K. (2011) ‘Enhanced concentrations of citric acid in spring aerosols collected at the Gosan background site in East Asia’, *Atmospheric Environment*, 45(30), pp. 5266–5272. doi: 10.1016/j.atmosenv.2011.06.065.

Kanji, Z. A. et al. (2017) ‘Overview of Ice Nucleating Particles’, *Meteorological Monographs*, 58, pp. 1.1-1.33. doi: 10.1175/amsmonographs-d-16-0006.1.

Kanji, Z. A. et al. (2019) ‘Heterogeneous ice nucleation properties of natural desert dust particles coated with a surrogate of secondary organic aerosol’, *Atmospheric Chemistry and Physics*, 19(7),

pp. 5091–5110. doi: 10.5194/acp-19-5091-2019.

Kanji, Z. A. and Abbatt, J. P. D. (2010) ‘Ice nucleation onto arizona test dust at cirrus temperatures: Effect of temperature and aerosol size on onset relative humidity’, *Journal of Physical Chemistry A*, 114(2), pp. 935–941. doi: 10.1021/jp908661m.

Kärcher, B. and Lohmann, U. (2002) ‘A Parameterization of cirrus cloud formation: Homogeneous freezing including effects of aerosol size’, *Journal of Geophysical Research Atmospheres*, 107(23), p. AAC 9-1-AAC 9-10. doi: 10.1029/2001JD001429.

Kärcher, B. and Lohmann, U. (2003) ‘A parameterization of cirrus cloud formation: Heterogeneous freezing’, *Journal of Geophysical Research: Atmospheres*, 108(14). pp. 1-15. doi: 10.1029/2002jd003220.

Kashchiev, D. (2000) *Nucleation: basic theory with applications*. Oxford: Butterworth-Heinemann.

Kaufmann, L. et al. (2016) ‘Ice nucleation efficiency of natural dust samples in the immersion mode’, *Atmospheric Chemistry and Physics*, 16(17), pp. 11177–11206. doi: 10.5194/acp-16-11177-2016.

Kerisit, S., Liu, C. and Ilton, E. S. (2008) ‘Molecular dynamics simulations of the orthoclase (001)- and (010)-water interfaces’, *Geochimica et Cosmochimica Acta*, 72(6), pp. 1481–1497. doi: 10.1016/j.gca.2007.12.014.

Kieft, T. L. (1988) ‘Ice Nucleation Activity in Lichens’, *Applied and Environmental Microbiology*, 54(7), pp. 1678–1681. doi: 10.1128/aem.54.7.1678-1681.1988.

Kieft, T. L. and Ruscetti, T. (1990) ‘Characterization of biological ice nuclei from a lichen’,

Journal of Bacteriology, 172(6), pp. 3519–3523. doi: 10.1128/jb.172.6.3519-3523.1990.

Kiselev, A. et al. (2017) ‘Active sites in heterogeneous ice nucleation—the example of K-rich feldspars’, *Science*, 355(6323), pp. 367–371. doi: 10.1126/science.aai8034.

Knopf, D. A. et al. (2011) ‘Stimulation of ice nucleation by marine diatoms’, *Nature Geoscience*. 4(2), pp. 88–90. doi: 10.1038/ngeo1037.

Knopf, D. A. and Alpert, P. A. (2013) ‘A water activity based model of heterogeneous ice nucleation kinetics for freezing of water and aqueous solution droplets’, *Faraday Discussions*, 165, pp. 513–534. doi: 10.1039/c3fd00035d.

Knopf, D. A., Alpert, P. A. and Wang, B. (2018) ‘The Role of Organic Aerosol in Atmospheric Ice Nucleation: A Review’, *ACS Earth and Space Chemistry*, 2(3), pp. 168–202. doi: 10.1021/acsearthspacechem.7b00120.

Knopf, D. A. and Koop, T. (2006) ‘Heterogeneous nucleation of ice on surrogates of mineral dust’, *Journal of Geophysical Research Atmospheres*, 111(12), pp. 1–10. doi: 10.1029/2005JD006894.

Kobayashi, M. et al. (2001) ‘Acid Dissolution of Olivines, Feldspars and Dunite’, *Water, Air, and Soil Pollution*, 130(1–4), pp. 757–762.

Koop, T. et al. (1997) ‘Freezing of HNO₃/H₂SO₄/H₂O Solutions at Stratospheric Temperatures: Nucleation Statistics and Experiments’, *The Journal of Physical Chemistry A*, 101(6), pp. 1117–1133. doi: 10.1021/jp9626531.

Koop, T. et al. (2000) ‘Water activity as the determinant for homogeneous ice nucleation in aqueous solutions’, *Nature*, 406(6796), pp. 611–614. doi: 10.1038/35020537.

Koop, T. et al. (2011) ‘Glass transition and phase state of organic compounds: dependency on

molecular properties and implications for secondary organic aerosols in the atmosphere’, *Physical Chemistry Chemical Physics*, 13(43), p. 19238. doi: 10.1039/c1cp22617g.

Koop, T. and Zobrist, B. (2009) ‘Parameterizations for ice nucleation in biological and atmospheric systems’, *Physical Chemistry Chemical Physics*, 11(46), pp. 10741–11064. doi: 10.1039/b914289d.

Kosmulski, M. (2009) *Surface Charging and Points of Zero Charge*. CRC Press Taylor and Francis Group.

Kozin, P. A., Shchukarev, A. and Boily, J. F. (2013) ‘Electrolyte ion binding at iron oxyhydroxide mineral surfaces’, *Langmuir*, 29(39), pp. 12129–12137. doi: 10.1021/la401318t.

Kudzotsa, I., Phillips, T. J. V. and Dobbie, S. (2018) ‘Effects of solid aerosols on partially glaciated clouds’, *Quarterly Journal of the Royal Meteorological Society*, 144(717), pp. 2634–2649. doi: 10.1002/qj.3376.

Kumai, M. and Francis, K. E. (1962) ‘Nuclei in Snow and Ice Crystals on the Greenland Ice Cap under Natural and Artificially Stimulated Conditions’, *Journal of the Atmospheric Sciences*, 19, pp. 474–481.

Kumar, A. et al. (2018) ‘Ice nucleation activity of silicates and aluminosilicates in pure water and aqueous solutions - Part 1: The K-feldspar microcline’, *Atmospheric Chemistry and Physics*, 18(10), pp. 7057–7079. doi: 10.5194/acp-18-7057-2018.

Kumar, A., Marcolli, C. and Peter, T. (2019a) ‘Ice nucleation activity of silicates and aluminosilicates in pure water and aqueous solutions-Part 2: Quartz and amorphous silica’, *Atmospheric Chemistry and Physics*, 19(9), pp. 6035–6058. doi: 10.5194/acp-19-6035-2019.

Kumar, A., Marcolli, C. and Peter, T. (2019b) ‘Ice nucleation activity of silicates and aluminosilicates in pure water and aqueous solutions-Part 3: Aluminosilicates’, *Atmospheric Chemistry and Physics*, 19(9), pp. 6059–6084. doi: 10.5194/acp-19-6059-2019.

Lee, M. R. et al. (2008) ‘The composition and crystallinity of the near-surface regions of weathered alkali feldspars’, *Geochimica et Cosmochimica Acta*, 72(20), pp. 4962–4975. doi: 10.1016/j.gca.2008.08.001.

Lee, M. R. and Parsons, I. (1995) ‘Microtextural controls of weathering of perthitic alkali feldspars’, *Geochimica et Cosmochimica Acta*, 59(21), pp. 4465–4488. doi: 10.1016/0016-7037(95)00255-X.

Lei, T. et al. (2014) ‘Hygroscopicity of organic compounds from biomass burning and their influence on the water uptake of mixed organic ammonium sulfate aerosols’, *Atmospheric Chemistry and Physics*, 14(20), pp. 11165–11183. doi: 10.5194/acp-14-11165-2014.

Lindemann, J. et al. (1982) ‘Plants as sources of airborne bacteria, including ice nucleation-active bacteria’, *Applied and Environmental Microbiology*, 44(5), pp. 1059–1063. doi: 10.1128/aem.44.5.1059-1063.1982.

Link, N. et al. (2020) ‘Dust-Catalyzed Oxidative Polymerization of Catechol and Its Impacts on Ice Nucleation Efficiency and Optical Properties’, *ACS Earth and Space Chemistry*, 4(7), pp. 1127–1139. doi: 10.1021/acsearthspacechem.0c00107.

Lohmann, U. (2002) ‘A glaciation indirect aerosol effect caused by soot aerosols’, *Geophysical Research Letters*, 29(4), pp. 1–44. doi: 10.1029/2001GL014357.

Lohmann, U. and Feichter, J. (2005) ‘Global indirect aerosol effects: a review’, *Atmospheric*

Chemistry and Physics, 5(3), pp. 715–737. doi: 10.5194/acp-5-715-2005.

Lohmann, U. and Hoose, C. (2009) ‘Sensitivity studies of different aerosol indirect effects in mixed-phase clouds’, *Atmospheric Chemistry and Physics*, 9(22), pp. 8917–8934. doi: 10.5194/acp-9-8917-2009.

Lohmann, U., Lüönd, F. and Mahrt, F. (2016) *An Introduction to Clouds: From the Microscale to Climate*. Cambridge University Press. doi: <https://doi.org/10.1017/CBO9781139087513>.

Lynch, D. K. et al. (2002) *Cirrus*. New York: Oxford University Press.

Ma, Q. et al. (2012) ‘A case study of Asian dust storm particles: Chemical composition, reactivity to SO₂ and hygroscopic properties’, *Journal of Environmental Sciences*, 24(1), pp. 62–71. doi: 10.1016/S1001-0742(11)60729-8.

Malm, W. C. et al. (1994) ‘Spatial and seasonal trends in particle concentration and optical extinction in the United States’, *Journal of Geophysical Research*. doi: 10.1029/93JD02916.

Marcilli, C. (2014) ‘Deposition nucleation viewed as homogeneous or immersion freezing in pores and cavities’, *Atmospheric Chemistry and Physics*, 14(4), pp. 2071–2104. doi: 10.5194/acp-14-2071-2014.

Marcilli, C., Luo, B. and Peter, T. (2004) ‘Mixing of the Organic Aerosol Fractions: Liquids as the Thermodynamically Stable Phases’, *Journal of Physical Chemistry A*, 108(12), pp. 2216–2224. doi: 10.1021/jp036080l.

Marcus, Y. (1988) ‘Ionic Radii in Aqueous Solutions’, *Chemical Reviews*, 88(8), pp. 1475–1498. doi: 10.1021/cr00090a003.

Marcus, Y. (2012) ‘Volumes of aqueous hydrogen and hydroxide ions at 0 to 200 °C’, *Journal of*

Chemical Physics, 137(15), pp. 0–5. doi: 10.1063/1.4758071.

Mason, R. H. et al. (2016) ‘Size-resolved measurements of ice-nucleating particles at six locations in North America and one in Europe’, *Atmospheric Chemistry and Physics*, 16(3), pp. 1637–1651. doi: 10.5194/acp-16-1637-2016.

McNaughton, C. S. et al. (2009) ‘Observations of heterogeneous reactions between Asian pollution and mineral dust over the Eastern North Pacific during INTEX-B’, *Atmospheric Chemistry and Physics*, 9(21), pp. 8283–8308. doi: 10.5194/acp-9-8283-2009.

Merrill, J. T., Uematsu, M. and Bleck, R. (1989) ‘Meteorological analysis of long range transport of mineral aerosols over the North Pacific’, *Journal of Geophysical Research*, 94(D6), pp. 8584–8598. doi: 10.1029/JD094iD06p08584.

Möhler, O. et al. (2008) ‘Heterogeneous ice nucleation activity of bacteria: New laboratory experiments at simulated cloud conditions’, *Biogeosciences*, 5(5), pp. 1425–1435. doi: 10.5194/bg-5-1425-2008.

Morris, C. E. et al. (2008) ‘The life history of the plant pathogen *Pseudomonas syringae* is linked to the water cycle’, *ISME Journal*, 2(3), pp. 321–334. doi: 10.1038/ismej.2007.113.

Morrison, H. et al. (2012) ‘Resilience of persistent Arctic mixed-phase clouds’, *Nature Geoscience*. doi: 10.1038/ngeo1332.

Mullin J., W. (2001) *Crystallisation*. 4th Ed. Oxford: Butterworth-Heinemann.

Murray, B. J. et al. (2010) ‘Kinetics of the homogeneous freezing of water’, *Physical Chemistry Chemical Physics*, 12(35), p. 10380. doi: 10.1039/c003297b.

Murray, B. J. et al. (2011) ‘Heterogeneous freezing of water droplets containing kaolinite particles’,

Atmospheric Chemistry and Physics, 11(9), pp. 4191–4207. doi: 10.5194/acp-11-4191-2011.

Murray, B. J. et al. (2012) ‘Ice nucleation by particles immersed in supercooled cloud droplets’, *Chemical Society Reviews*, 41(19), pp. 6519–6554. doi: 10.1039/c2cs35200a.

Nash, V. E. and Marshall, C. E. (1957) ‘Cationic Reactions of Feldspar Surfaces’, *Soil Science Society of America Journal*, 21(2), pp. 149–153. doi: 10.2136/sssaj1957.03615995002100020005x.

Nesbitt, H. W., Macrae, N. D. and Shotyk, W. (1991) ‘Congruent and incongruent dissolution of labradorite in dilute, acidic, salt solutions’, *Journal of Geology*, 99(3), pp. 429–442. doi: 10.1086/629504.

Nightingale, E. R. (1959) ‘Phenomenological theory of ion solvation. Effective radii of hydrated ions’, *Journal of Physical Chemistry*, 63(9), pp. 1381–1387. doi: 10.1021/j150579a011.

O’Sullivan, D. et al. (2014) ‘Ice nucleation by fertile soil dusts: Relative importance of mineral and biogenic components’, *Atmospheric Chemistry and Physics*, 14(4), pp. 1853–1867. doi: 10.5194/acp-14-1853-2014.

O’Sullivan, D. et al. (2015) ‘The relevance of nanoscale biological fragments for ice nucleation in clouds’, *Scientific Reports*, 5, pp. 1–7. doi: 10.1038/srep08082.

O’Sullivan, D. et al. (2016) ‘The adsorption of fungal ice-nucleating proteins on mineral dusts: A terrestrial reservoir of atmospheric ice-nucleating particles’, *Atmospheric Chemistry and Physics*, 16(12), pp. 7879–7887. doi: 10.5194/acp-16-7879-2016.

O’Sullivan, D. et al. (2018) ‘Contributions of biogenic material to the atmospheric ice-nucleating particle population in North Western Europe’, *Scientific Reports*, 8(1), pp. 1–9. doi:

10.1038/s41598-018-31981-7.

Oelkers, E. H. and Schott, J. (1998) ‘Does organic adsorption affect alkali-feldspar dissolution rates?’, *Chemical Geology*, 151(1–4), pp. 235–245. doi: 10.1016/S0009-2541(98)00082-5.

Peckhaus, A. et al. (2016) ‘A comparative study of K-rich and Na/Ca-rich feldspar ice-nucleating particles in a nanoliter droplet freezing assay’, *Atmospheric Chemistry and Physics*, 16(18), pp. 11477–11496. doi: 10.5194/acp-16-11477-2016.

Perkins, R. J. et al. (2020) ‘The Labile Nature of Ice Nucleation by Arizona Test Dust’, *ACS Earth and Space Chemistry*. American Chemical Society, 4(1), pp. 133–141. doi: 10.1021/acsearthspacechem.9b00304.

Petters, M. D. and Wright, T. P. (2015) ‘Revisiting ice nucleation from precipitation samples’, *Geophysical Research Letters*, 42(20), pp. 8758–8766. doi: 10.1002/2015GL065733.

Pfaff, J. D. (1993) *Methods 300.0: Determination of Inorganic Anions By Ion Chromatography*, Office of Research and Development, USEPA. Cincinnati, Ohio. doi: 10.1016/b978-0-8155-1398-8.50022-7.

Phillips, V. T. J. et al. (2009) ‘Potential impacts from biological aerosols on ensembles of continental clouds simulated numerically’, *Biogeosciences*, 6(6), pp. 987–1014. doi: 10.5194/bg-6-987-2009.

Van Pinxteren, D. et al. (2016) ‘Cloud water composition during HCCT-2010: Scavenging efficiencies, solute concentrations, and droplet size dependence of inorganic ions and dissolved organic carbon’, *Atmospheric Chemistry and Physics*, 16(5), pp. 3185–3205. doi: 10.5194/acp-16-3185-2016.

- Pouleur, S. et al. (1992) 'Ice Nucleation Activity in *Fusarium acuminatum* and *Fusarium avenaceum*', *Applied and Environmental Microbiology*, 58(9), pp. 2960–2964.
- Pratt, K. A. et al. (2009) 'In situ detection of biological particles in cloud ice-crystals', *Nature Geoscience*. 2(6), pp. 398–401. doi: 10.1038/ngeo521.
- Prezzi, A. J., Demott, P. J., et al. (2009) 'Ice nuclei characteristics from M-PACE and their relation to ice formation in clouds', *Tellus B: Chemical and Physical Meteorology*, 61 B(2), pp. 436–448. doi: 10.1111/j.1600-0889.2009.00415.x.
- Prezzi, A. J., Petters, M. D., et al. (2009) 'Relative roles of biogenic emissions and saharan dust as ice nuclei in the amazon basin', *Nature Geoscience*. 2(6), pp. 402–405. doi: 10.1038/ngeo517.
- Prewitt, C. T., Sueno, S. and Papike, J. J. (1976) 'The crystal structures of high albite and monalbite at high temperatures', *American Mineralogist*, 61(11–12), pp. 1213–1225.
- Primm, K. M. et al. (2017) 'Depositional ice nucleation on NX illite and mixtures of NX illite with organic acids', *Journal of Atmospheric Chemistry*. *Journal of Atmospheric Chemistry*, 74(1), pp. 55–69. doi: 10.1007/s10874-016-9340-x.
- Prospero, J. M. (1999) 'Long-range transport of mineral dust in the global atmosphere: Impact of African dust on the environment of the southeastern United States', *Proceedings of the National Academy of Sciences*, 96(7), pp. 3396–3403. doi: 10.1073/pnas.96.7.3396.
- Prospero, J. M. et al. (2002) 'Environmental characterization of global sources of atmospheric soil dust identified with the Nimbus 7 Total Ozone Mapping Spectrometer (TOMS) absorbing aerosol product', *Reviews of Geophysics*, 40(1), pp. 2-1-2–31. doi: 10.1029/2000RG000095.
- Pruppacher, H. R. and Klett, J. D. (1997) *Microphysics of Clouds and Precipitation*. 2nd Edition.

Springer, Dordrecht. doi: <https://doi.org/10.1007/978-0-306-48100-0>.

Pummer, B. G. et al. (2012) ‘Suspendable macromolecules are responsible for ice nucleation activity of birch and conifer pollen’, *Atmospheric Chemistry and Physics*, 12(5), pp. 2541–2550. doi: 10.5194/acp-12-2541-2012.

Pummer, B. G. et al. (2015) ‘Ice nucleation by water-soluble macromolecules’, *Atmospheric Chemistry and Physics*, 15(8), pp. 4077–4091. doi: 10.5194/acp-15-4077-2015.

Pye, H. O. T. et al. (2020) *The acidity of atmospheric particles and clouds*, *Atmospheric Chemistry and Physics*. 20(8), pp. 4809–4888. doi: 10.5194/acp-20-4809-2020.

Quinn, P. K. et al. (2002) ‘A 3-year record of simultaneously measured aerosol chemical and optical properties at Barrow, Alaska’, *Journal of Geophysical Research: Atmospheres*, 107(11). doi: 10.1029/2001jd001248.

Quinn, P. K. et al. (2004) ‘Aerosol optical properties measured on board the Ronald H. Brown during ACE-Asia as a function of aerosol chemical composition and source region’, *Journal of Geophysical Research D: Atmospheres*, 109(19), pp. 1–28. doi: 10.1029/2003JD004010.

Radke, L. F., Hobbs, P. V. and Pinnons, J. E. (1976) ‘Observations of Cloud Condensation Nuclei, Sodium-Containing Particles, Ice Nuclei and the Light-Scattering Coefficient Near Barrow, Alaska’, *Journal of Applied Meteorology*, pp. 982–995. doi: 10.1175/1520-0450(1976)015<0982:oocns>2.0.co;2.

Reischel, M. T. and Vali, G. (1975) ‘Freezing Nucleation in Aqueous Electrolytes’, *Tellus*, 27(4), pp. 414–427. doi: 10.1111/j.2153-3490.1975.tb01692.x.

Ren, Y., Bertram, A. K. and Patey, G. N. (2020) ‘Effects of Inorganic Ions on Ice Nucleation by

the Al Surface of Kaolinite Immersed in Water’, *Journal of Physical Chemistry B*, 124(22), pp. 4605–4618. doi: 10.1021/acs.jpcc.0c01695.

Richard, C., Martin, J. G. and Pouleur, S. (1996) ‘Ice nucleation activity identified in some phytopathogenic *Fusarium* species’, *Phytoprotection*, 77(2), pp. 83–92. doi: 10.7202/706104ar.

Rietveld, H. M. (1969) ‘A profile refinement method for nuclear and magnetic structures’, *Journal of Applied Crystallography*. International Union of Crystallography, 2(2), pp. 65–71. doi: 10.1107/S0021889869006558.

Rigg, Y. J., Alpert, P. A. and Knopf, D. A. (2013) ‘Immersion freezing of water and aqueous ammonium sulfate droplets initiated by humic-like substances as a function of water activity’, *Atmospheric Chemistry and Physics*, 13(13), pp. 6603–6622. doi: 10.5194/acp-13-6603-2013.

Rogers, D. C. et al. (1998) ‘Measurements of ice nucleating aerosols during SUCCESS’, *Geophysical Research Letters*, 25(9), pp. 1383–1386. doi: 10.1029/97GL03478.

Rogers, D. C., Demott, P. J. and Kreidenweis, S. M. (2001) ‘Airborne measurements of tropospheric ice-nucleating aerosol particles in the Arctic spring’, *Journal of Geophysical Research*, 106(D14), pp. 15053–15063.

Ruiz-Agudo, E., Putnis, C. V. and Putnis, A. (2014) ‘Coupled dissolution and precipitation at mineral-fluid interfaces’, *Chemical Geology*, 383, pp. 132–146. doi: 10.1016/j.chemgeo.2014.06.007.

Sahyoun, M. et al. (2017) ‘Impact of bacterial ice nucleating particles on weather predicted by a numerical weather prediction model’, *Atmospheric Environment*, 170, pp. 33–44. doi: 10.1016/j.atmosenv.2017.09.029.

Šantl-Temkiv, T. et al. (2019) ‘Biogenic Sources of Ice Nucleating Particles at the High Arctic Site Villum Research Station’, *Environmental Science & Technology*, 53(18) pp. 10580-10590 doi: 10.1021/acs.est.9b00991.

Saxena, P. and Hildemann, L. M. (1996) ‘Water-soluble organics in atmospheric particles: A critical review of the literature and application of thermodynamics to identify candidate compounds’, *Journal of Atmospheric Chemistry*, 24, pp. 57–109. doi: 10.1007/BF00053823.

Schütz, L. (1980) ‘Long Range Transport of Desert Dust With Special Emphasis on the Sahara’, *Annals of the New York Academy of Sciences*, 338(1), pp. 515–532. doi: 10.1111/j.1749-6632.1980.tb17144.x.

Schütz, L. and Rahn, K. A. (1982) ‘Trace-element concentrations in erodible soils’, *Atmospheric Environment (1967)*, 16(1), pp. 171–176. doi: 10.1016/0004-6981(82)90324-9.

Seinfeld, J. . and Pandis, S. . (2006) *Atmospheric Chemistry and Physics: From Air Pollution to Climate Change*. 2nd Edition. Wiley-interscience.

Serreze, M. C. and Francis, J. A. (2006) ‘The arctic amplification debate’, *Climatic Change*. 76, pp. 241-264. doi: 10.1007/s10584-005-9017-y.

Sesartic, A., Lohmann, U. and Storelvmo, T. (2012) ‘Bacteria in the ECHAM5-HAM global climate model’, *Atmospheric Chemistry and Physics*, 12(18), pp. 8645–8661. doi: 10.5194/acp-12-8645-2012.

Sesartic, A., Lohmann, U. and Storelvmo, T. (2013) ‘Modelling the impact of fungal spore ice nuclei on clouds and precipitation’, *Environmental Research Letters*, 8(1), pp. 1-8. doi: 10.1088/1748-9326/8/1/014029.

- Shchukarev, A. and Ramstedt, M. (2017) ‘Cryo-XPS: probing intact interfaces in nature and life’, *Surface and Interface Analysis*, 49(4), pp. 349–356. doi: 10.1002/sia.6025.
- Shilling, J. E., Fortin, T. J. and Tolbert, M. A. (2006) ‘Depositional ice nucleation on crystalline organic and inorganic solids’, *Journal of Geophysical Research Atmospheres*, 111(12), pp. 1–9. doi: 10.1029/2005JD006664.
- Shimizu, K. et al. (2013) ‘X-ray photoelectron spectroscopy of fast-frozen hematite colloids in aqueous solutions. 5. Halide ion (F-, Cl-, Br-, I-) adsorption’, *Langmuir*, 29(8), pp. 2623–2630. doi: 10.1021/la3039973.
- Shupe, M. D. (2011) ‘Clouds at arctic atmospheric observatories. Part II: Thermodynamic phase characteristics’, *Journal of Applied Meteorology and Climatology*, 50(3), pp. 645–661. doi: 10.1175/2010JAMC2468.1.
- Si, M. et al. (2019) ‘Concentrations, composition, and sources of ice-nucleating particles in the Canadian High Arctic during spring 2016’, *Atmospheric Chemistry and Physics*, 19(5), pp. 3007–3024. doi: 10.5194/acp-2018-950.
- Spurny, K. R. and Lodge, J. J. P. (1972) *Collection Efficiency Tables for Membrane Filters Used in the Sampling and Analysis of Aerosols and Hydrosols*, NCAR TECHNICAL NOTE. doi: 10.5065/D6F769JJ.
- Stohl, A. (2006) ‘Characteristics of atmospheric transport into the Arctic troposphere’, *Journal of Geophysical Research Atmospheres*, 111(11), pp. 1–17. doi: 10.1029/2005JD006888.
- Storelvmo, T. (2017) ‘Aerosol Effects on Climate via Mixed-Phase and Ice Clouds’, *Annual Review of Earth and Planetary Sciences*, 45, pp. 199–222. doi: 10.1146/annurev-earth-060115-

012240.

Stumm, W. and Morgan, J. J. (1981) *Aquatic chemistry: An introduction emphasizing chemical equilibria in natural waters*. 2nd Edition. Wiley .

Sullivan, R. C., Miñambres, L., et al. (2010) ‘Chemical processing does not always impair heterogeneous ice nucleation of mineral dust particles’, *Geophysical Research Letters*, 37(24), pp. 1–5. doi: 10.1029/2010GL045540.

Sullivan, R. C., Petters, M. D., et al. (2010) ‘Irreversible loss of ice nucleation active sites in mineral dust particles caused by sulphuric acid condensation’, *Atmospheric Chemistry and Physics*, 10(23), pp. 11471–11487. doi: 10.5194/acp-10-11471-2010.

Takeishi, A. and Storelvmo, T. (2018) ‘A Study of Enhanced Heterogeneous Ice Nucleation in Simulated Deep Convective Clouds Observed’, *Journal of Geophysical Research: Atmospheres*, 123(23), pp. 13396–13420. doi: 10.1029/2018JD028889.

Tang, M., Cziczo, D. J. and Grassian, V. H. (2016) ‘Interactions of Water with Mineral Dust Aerosol: Water Adsorption, Hygroscopicity, Cloud Condensation, and Ice Nucleation’, *Chemical Reviews*, 116(7), pp. 4205–4259. doi: 10.1021/acs.chemrev.5b00529.

Tinsley, B., Rohrbaugh, R. and Hei, M. (2000) ‘Effects of Image Charges on the Scavenging of Aerosol Particles by Cloud Droplets and on Droplet Charging and Possible Ice Nucleation Processes’, *Journal of the Atmospheric Sciences*, 57(1975), pp. 2118–2134. doi: 10.1175/1520-0469(2000)057<2118:EOICOT>2.0.CO;2.

Tobo, Y. et al. (2012) ‘Impacts of chemical reactivity on ice nucleation of kaolinite particles: A case study of levoglucosan and sulfuric acid’, *Geophysical Research Letters*, 39(19), pp. 1–5. doi:

10.1029/2012GL053007.

Tobo, Y. et al. (2019) ‘Glacially sourced dust as a potentially significant source of ice nucleating particles’, *Nature Geoscience*, 12(4), pp. 253–258. doi: 10.1038/s41561-019-0314-x.

USEPA (1986) *Method 300.7: Dissolved Sodium, Ammonium, Potassium, Magnesium, and Calcium in Wet Deposition by Chemical Suppressed Ion Chromatography-United State*. Cincinnati, Ohio.

Usher, C. R., Michel, A. E. and Grassian, V. H. (2003) ‘Reactions on Mineral Dust’, *Chemical Reviews*, 103, pp. 4883–4939. doi: 10.1021/cr020657y.

Vali, G. (1971) ‘Quantitative Evaluation of Experimental Results on the Heterogeneous Freezing Nucleation of Supercooled Liquids’, *Journal of the Atmospheric Sciences*, 28(3), pp. 402–409. doi: 10.1175/1520-0469(1971)028<0402:qeoera>2.0.co;2.

Vali, G. (1994) ‘Freezing Rate Due to Heterogeneous Nucleation’, *Journal of the Atmospheric Sciences*, 51(13), pp. 1843–1856.

Vali, G. (2008) ‘Repeatability and randomness in heterogeneous freezing nucleation’, *Atmospheric Chemistry and Physics*, 8(16), pp. 5017–5031. doi: 10.5194/acp-8-5017-2008.

Vali, G. et al. (2015) ‘Technical Note: A proposal for ice nucleation terminology’, *Atmospheric Chemistry and Physics*, 15(18), pp. 10263–10270. doi: 10.5194/acp-15-10263-2015.

Vergara-Temprado, J. et al. (2017) ‘Contribution of feldspar and marine organic aerosols to global ice nucleating particle concentrations’, *Atmospheric Chemistry and Physics*, 17(5), pp. 3637–3658. doi: 10.5194/acp-17-3637-2017.

Wagner, R. et al. (2011) ‘New cloud chamber experiments on the heterogeneous ice nucleation

ability of oxalic acid in the immersion mode’, *Atmospheric Chemistry and Physics*, 11(5), pp. 2083–2110. doi: 10.5194/acp-11-2083-2011.

Wagner, R. and Möhler, O. (2013) ‘Heterogeneous ice nucleation ability of crystalline sodium chloride dihydrate particles’, *Journal of Geophysical Research Atmospheres*, 118(10), pp. 4610–4622. doi: 10.1002/jgrd.50325.

Wang, B. et al. (2012) ‘The deposition ice nucleation and immersion freezing potential of amorphous secondary organic aerosol: Pathways for ice and mixed-phase cloud formation’, *Journal of Geophysical Research Atmospheres*, 117(16), pp. 1–12. doi: 10.1029/2012JD018063.

Wang, B. and Knopf, D. A. (2011) ‘Heterogeneous ice nucleation on particles composed of humic-like substances impacted by O₃’, *Journal of Geophysical Research Atmospheres*, 116(3), pp. 1–14. doi: 10.1029/2010JD014964.

Welch, S. A. and Ullman, W. J. (1996) ‘Feldspar dissolution in acidic and organic solutions: Compositional and pH dependence of dissolution rate’, *Geochimica et Cosmochimica Acta*, 60(16), pp. 2939–2948. doi: 10.1016/0016-7037(96)00134-2.

Westbrook, C. D. and Illingworth, A. J. (2011) ‘Evidence that ice forms primarily in supercooled liquid clouds at temperatures $>-27^{\circ}\text{C}$ ’, *Geophysical Research Letters*, 38(14), pp. 1–4. doi: 10.1029/2011GL048021.

Wex, H. et al. (2014) ‘Kaolinite particles as ice nuclei: Learning from the use of different kaolinite samples and different coatings’, *Atmospheric Chemistry and Physics*, 14(11), pp. 5529–5546. doi: 10.5194/acp-14-5529-2014.

Wex, H. et al. (2019) ‘Annual variability of ice-nucleating particle concentrations at different

Arctic locations’, *Atmospheric Chemistry and Physics*, 19(7), pp. 5293–5311. doi: 10.5194/acp-19-5293-2019.

Whale, T. . et al. (2018) ‘The enhancement and suppression of immersion mode heterogeneous ice-nucleation by solutes’, *Chemical Science*. Royal Society of Chemistry, 9, pp. 4142–4151. doi: 10.1039/C7SC05421A.

Whale, T. F. et al. (2015) ‘A technique for quantifying heterogeneous ice nucleation in microlitre supercooled water droplets’, *Atmospheric Measurement Techniques*, 8(6), pp. 2437–2447. doi: 10.5194/amt-8-2437-2015.

Whale, T. F. et al. (2017) ‘The role of phase separation and related topography in the exceptional ice-nucleating ability of alkali feldspars’, *Physical Chemistry Chemical Physics*. Royal Society of Chemistry, 19(46), pp. 31186–31193. doi: 10.1039/c7cp04898j.

Worringen, A. et al. (2015) ‘Single-particle characterization of ice-nucleating particles and ice particle residuals sampled by three different techniques’, *Atmospheric Chemistry and Physics*, 15(8), pp. 4161–4178. doi: 10.5194/acp-15-4161-2015.

Worthy, S. E. et al. (2021) ‘The effect of $(\text{NH}_4)_2\text{SO}_4$ on the freezing properties of non-mineral dust ice nucleating substances of atmospheric relevance’, (March), pp. 1–30.

Wurzler, S., Reisin, T. G. and Levin, Z. (2000) ‘Modification of mineral dust particles by cloud processing and subsequent effects on drop size distributions’, *Journal of Geophysical Research Atmospheres*, 105(D4), pp. 4501–4512. doi: 10.1029/1999JD900980.

Xi, Y. et al. (2021) ‘Concentrations and Properties of the Ice Nucleating Substances in Exudates from Antarctic Sea-Ice Diatoms’, *Environmental Science Processes & Impacts*, 23(2), pp. 323-

334. doi: 10.1039/D0EM00398K.

Yang, Y. et al. (2014) 'Effects of Al/Si ordering on feldspar dissolution: Part I. Crystallographic control on the stoichiometry of dissolution reaction', *Geochimica et Cosmochimica Acta*, 126, pp. 574–594. doi: 10.1016/j.gca.2013.10.047.

Yuan, G. et al. (2019) 'A review of feldspar alteration and its geological significance in sedimentary basins: From shallow aquifers to deep hydrocarbon reservoirs', *Earth-Science Reviews*. 191, pp. 114–140. doi: 10.1016/j.earscirev.2019.02.004.

Yun, J. et al. (2020) 'Surface Composition Dependence on the Ice Nucleating Ability of Potassium-Rich Feldspar', *ACS Earth and Space Chemistry*, 4(6), pp. 873–881. doi: 10.1021/acsearthspacechem.0c00077.

Zhao, H. (2006) 'Are ionic liquids kosmotropic or chaotropic? An evaluation of available thermodynamic parameters for quantifying the ion kosmotropicity of ionic liquids', *Journal of Chemical Technology and Biotechnology*, 81(6), pp. 877–891. doi: 10.1002/jctb.1449.

Zobrist, B. et al. (2006) 'Oxalic acid as a heterogeneous ice nucleus in the upper troposphere and its indirect aerosol effect', *Atmospheric Chemistry and Physics*, 6(10), pp. 3115–3129. doi: 10.5194/acp-6-3115-2006.

Zobrist, B. et al. (2008) 'Heterogeneous ice nucleation in aqueous solutions: The role of water activity', *Journal of Physical Chemistry A*, 112(17), pp. 3965–3975. doi: 10.1021/jp7112208.

Zolles, T. et al. (2015) 'Identification of ice nucleation active sites on feldspar dust particles', *Journal of Physical Chemistry A*, 119(11), pp. 2692–2700. doi: 10.1021/jp509839x.

Zuberi, B. et al. (2001) 'Heterogeneous freezing of aqueous particles induced by crystallized

(NH₄)₂SO₄, ice, and letovicite', *Journal of Physical Chemistry A*, 105(26), pp. 6458–6464. doi:
10.1021/jp010094e.

Appendices

Appendix A Classical nucleation theory for ice nucleation

Nucleation is the first step for the formation of a new thermodynamic phase from the metastable parent phase. Classical nucleation theory (CNT) is a simple and common model used to describe the process of nucleation (Kashchiev, 2000; Mullin J., 2001). Here we briefly describe homogeneous freezing and heterogeneous freezing from the view of classical nucleation theory.

A1 Homogeneous freezing

Based on classical nucleation theory, the change of Gibbs free energy (ΔG) for the formation of an ice embryo by homogeneous nucleation is defined as:

$$\Delta G = \frac{4}{3}\pi r^3 \Delta g + 4\pi r^2 \sigma \quad (\text{A.1}),$$

where r is the radius of the ice embryo, Δg is the difference of free energy per unit volume of the new phase (ice) and old phase (liquid water or water vapor), and σ is the interfacial tension between the new phase and the old phase. ΔG is composed of 2 terms, one due to the change in bulk free energy, $\frac{4}{3}\pi r^3 \Delta g$, which is negative here, and the other one due to the formation of new interface, $4\pi r^2 \sigma$, which is positive. The magnitude of these two terms is plotted as a function of the ice embryo radius, r , in Fig. A.1. For small r , the interface energy term, $4\pi r^2 \sigma$, dominates and hence ΔG is positive. As r increases, the bulk energy term, $\frac{4}{3}\pi r^3 \Delta g$, increases and eventually dominates. For the growth of a new cluster to occur spontaneously, the change in ΔG should decrease as the radius increases (i.e. $\frac{d\Delta G}{dr} < 0$). There is a critical value of r which, once exceeded, the cluster can grow spontaneously. The critical radius, r^* , occurs when $\frac{d\Delta G}{dr} = 0$. Associated with the critical

radius, there is a critical value of free energy change, ΔG^* , which can be considered as the energy barrier for homogeneous freezing. Based on Eq. A.1, $r^* = \frac{-2\sigma}{\Delta g}$ and $\Delta G_{hom}^* = \frac{16\pi\sigma^3}{3\Delta^2 g}$. Therefore, the rate coefficient of homogeneous freezing (J_{hom}) is defined as the following equation similar to the Arrhenius equation:

$$J_{hom} = A_{hom} \exp\left(-\frac{\Delta G_{hom}^*}{kT}\right) = A_{hom} \exp\left(-\frac{16\pi\sigma^3}{3\Delta^2 gkT}\right) \quad (A.2),$$

where A_{hom} is the Arrhenius pre-exponential factor for homogeneous nucleation.

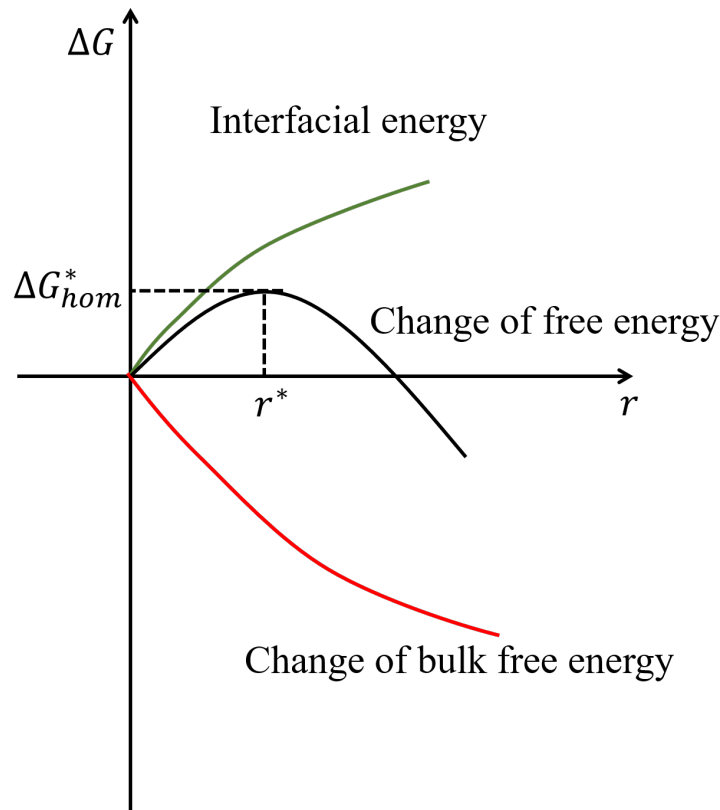


Figure A.1: Change of free energy during homogeneous freezing a function of the cluster radius, r .

A2 Heterogeneous freezing

The description of heterogeneous freezing by CNT builds on the description of homogeneous freezing. In short, CNT assumes that INPs act as catalysts and lower the energy barrier for homogeneous freezing, as shown in Fig. A.2. The energy barrier for heterogeneous

freezing (ΔG_{het}^*) can be calculated by applying a factor, $f(\theta)$, to the energy barrier for homogeneous freezing (ΔG_{hom}^*):

$$\Delta G_{het}^* = \Delta G_{hom}^* \times f(\theta) = \Delta G_{hom}^* \times \frac{(2+\cos\theta)(1-\cos\theta)^2}{4} \quad (\text{A.3}),$$

where θ is the contact angle between the ice embryo and the surface of an INP. Accordingly, the rate coefficient of heterogeneous freezing (J_{het}) can also be calculated similar to the Arrhenius equation:

$$J_{het} = A_{het} \exp\left(-\frac{\Delta G_{het}^*}{kT}\right) \quad (\text{A.4}),$$

where A_{het} is the Arrhenius pre-exponential factor for heterogeneous freezing.

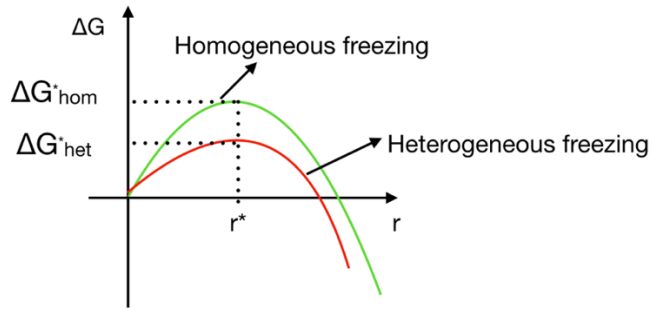


Figure A.2: Free energy change during homogeneous freezing and heterogeneous freezing as a function of cluster radius, r .

Appendix B

B1 Mixing time of solutes in water droplets

The mixing time (τ_{mix}) of a solute in water droplets was calculated with the following equation (Seinfeld and Pandis, 2006):

$$\tau_{mix} = \frac{d^2}{4\pi^2 D} \quad (\text{B.1})$$

where d is the diameter of the water droplets and D is the diffusion coefficient of the solute. The diffusion coefficient (D) of the solute was calculated with the Stokes-Einstein equation (Koop et al., 2011):

$$D = \frac{kT}{6\pi\eta R_H} \quad (\text{B.2})$$

where k is the Boltzmann constant, T is the temperature, η is the dynamic viscosity of water, and R_H is the hydrodynamic radius of the solute. Listed in Table. B.1 are calculated mixing times of cations studied in this work using Eq. B.1 and B.2. For these calculations we assumed a water droplet diameter of 1.5 mm (consistent with our experiments), a dynamic viscosity of water at 0°C of 0.0018 Pa·s (Haynes et al., 2014), and a hydrodynamic radius of the hydrated cations taken from Nightingale (1959), The calculated mixing times were < 4 minutes at 0 °C. For the freezing experiments, the temperature of the cold plate was kept above 0 °C for around 4~5 minutes after the droplets were generated, which is longer than the mixing times.

Table B.1: Calculated mixing time (τ_{mix}) of alkali metal cations.

Cations	$\tau_{\text{mix}}(\text{s})$
Li ⁺	196
Na ⁺	184
K ⁺	170
Rb ⁺	169
Cs ⁺	169

Table B.2: Information on the crystal structure of microcline and albite. The information for microcline is obtained from Bailey (1969) and the information for albite is obtained from Prewitt et al. (1976).

	Microcline	Albite
a (Å)	8.56	8.15
b (Å)	12.97	12.87
c (Å)	7.22	7.11
α (°)	90.65	93.52
β (°)	115.93	116.46
γ (°)	87.78	90.26
Space group	$C\bar{1}$	$C\bar{1}$

B2 Calculations of the depth of ion exchange between H_3O^+ and parent K^+ of K-rich feldspar immersed in water using literature data.

Peckhaus et al. (2016) and Gülgönül et al. (2012) quantified the release of parent K^+ from K-rich feldspar particles as a function of time when exposed to pure water (pH 6 - 7). From their measurements, we calculated the depth of full exchange of K^+ in K-rich feldspar. Details are included in Table B.3.

Table B.3: Calculations of the depth of full exchange of K^+ in K-rich feldspar.

	Units	Peckhaus et al. (2016)	Gülgönül et al. (2012)
Duration of exposure to pure water	h	12	4
Mass of K-rich feldspar: m	g	0.1	5
Volume of pure water: V	mL	10	95
Concentration of Released K^+ : c	M	5×10^{-5}	1.06×10^{-4}
BET surface area: s_0	m ² /g	1.79	1.43
Avogadro constant: N_A	mol ⁻¹	6.02×10^{23}	6.02×10^{23}
Percentage of microcline in K-rich feldspar: ff		76 %	88 %
Dimension of unit cell of microcline	nm	$a = 0.856; b = 1.297; c = 0.722$	$a = 0.856; b = 1.297; c = 0.722$
Surface area of K-rich feldspar: $(S_{K-feldspar}) = m \times s_0$	m ²	0.179	7.15
Surface area of microcline in K-rich feldspar: $(S_{microcline}) = S_{K-feldspar} \times ff$	m ²	0.136	6.292
Number of released K^+ : $(N_{released}) = c \times V \times N_A$		3.01×10^{17}	6.04×10^{18}
Average area of a plane of a microcline unit cell: $\sigma = \frac{ab+ac+bc}{3}$	m ²	8.911×10^{-19}	8.911×10^{-19}
$N_{theoretical}$ (theoretical number of parent K^+ in one-unit cell depth of a sample): $N_{theoretical} = S_{microcline} \times \frac{4}{\sigma}$		6.1×10^{17}	2.82×10^{19}
% depth of top unit cell contributing to ion exchange of K^+ : (τ) $= \frac{N_{released}}{N_{theoretical}}$		49 %	21 %

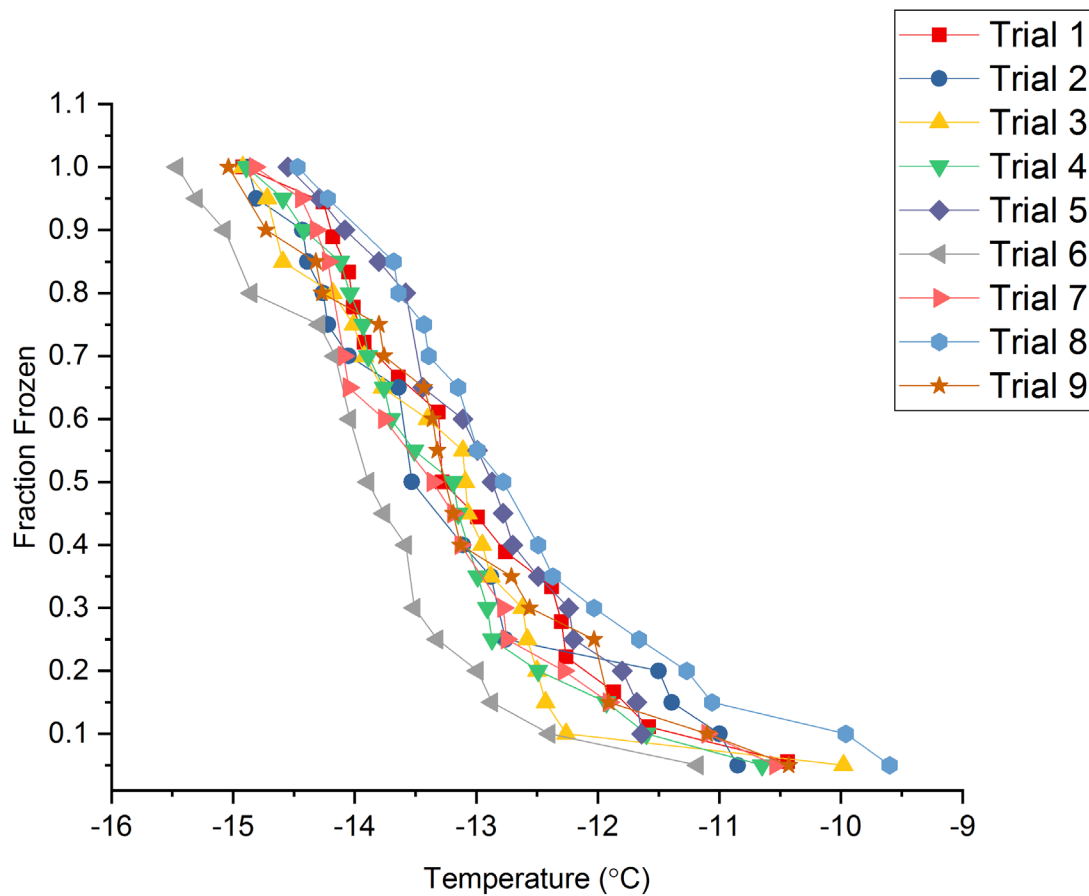
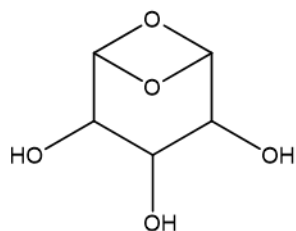


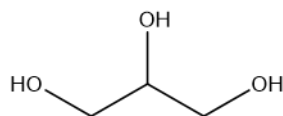
Figure B.1: Fraction of droplets containing K-feldspar (0.05 wt %) frozen as a function of temperature for 9 different experiments from the same K-feldspar suspension. Each experiment corresponds to the freezing of 20 droplets.

Appendix C

Table C.1: Structures of the polyols used in the experiments.

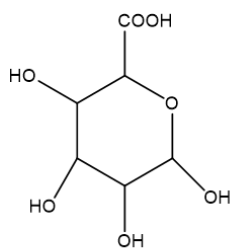


Levoglucosan

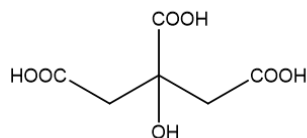


Glycerol

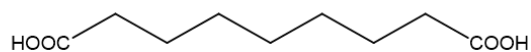
Table C.2: Structures of the carboxylic acids used in the experiments.



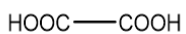
Glucuronic acid



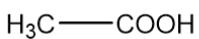
Citric acid



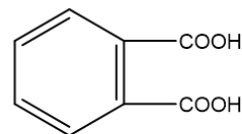
Azeleic acid



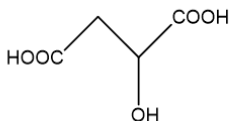
Oxalic acid



Acetic acid



Phthalic acid



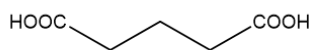
Malic acid



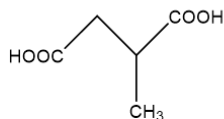
Malonic acid



Maleic acid



Glutaric acid



Methylsuccinic acid

C1 The mixing time of solutes in water droplets

Here we calculate the mixing time (τ_{mix}) of the organic and inorganic solutes in 2 μL water droplets at 0 °C. Calculations were carried out with the following equation (Seinfeld and Pandis, 2006):

$$\tau_{mix} = \frac{d^2}{4\pi^2 D} \quad (\text{C.1}),$$

where d is the diameter of water droplets and D is the diffusion coefficient of the solute in water. The diameter of 2 μL droplets was 1.5 mm assuming that water droplets are spherical. The diffusion coefficient (D) of the solute was calculated with the Stokes-Einstein equation (Koop et al., 2011):

$$D = \frac{kT}{6\pi\eta R_H} \quad (\text{C.2}),$$

where k is the Boltzmann constant, T is the temperature (0 °C), η is the dynamic viscosity of water at 0 °C (0.0018 Pa·s (Haynes et al., 2014)), and R_H is the hydrodynamic radius of the solute. The hydrodynamic radius of organic molecules was estimated with the following equation assuming that the molecules were spherical:

$$R_H = \sqrt[3]{\frac{3M}{4\pi\rho N_A}} \quad (\text{C.3}),$$

where M is the molecular weight of the organic molecules, ρ is the density of organic molecules, and N_A is the Avogadro constant. The inorganic acids, HNO_3 and HCl , were dissociated into H^+

and NO_3^- or Cl^- . The hydrodynamic radius of these ions was obtained from (Marcus, 1988, 2012) As shown in Table. C.3, the calculated mixing times at 0 °C for all solutes used in our studies were less than 4 minutes. In the freezing experiments, the temperature of the cold plate was kept above 0 °C for around 4~5 minutes after the droplets were generated, hence we conclude that the solutes used in our studies were well mixed in the water droplets.

Table C.3: The calculated mixing times (τ_{mix}) of organics and inorganic acids.

Solutes	Molecular weight of the solute (g/mol)	Density of the solute (g/cm^{-3})	Hydrodynamic radius of solutes (nm)	τ_{mix} (s)
Levogluconan	162	1.69	0.34	174
Glycerol	92	1.26	0.31	159
Glucuronic acid	194	1.99	0.34	174
Citric acid	192	1.66	0.36	185
Azelaic acid	188	1.44	0.37	190
Oxalic acid	90	1.9	0.26	133
Acetic acid	60	1.05	0.28	144
Phthalic acid	166	1.59	0.34	174
Malic acid	134	1.61	0.32	164
Malonic acid	104	1.62	0.29	149
Maleic acid	116	1.59	0.31	159
Glutaric acid	132	1.43	0.33	169
Methylsuccinic acid	132	1.41	0.33	169
H^+			0.1	51
NO_3^-			0.177	91
Cl^-			0.180	92

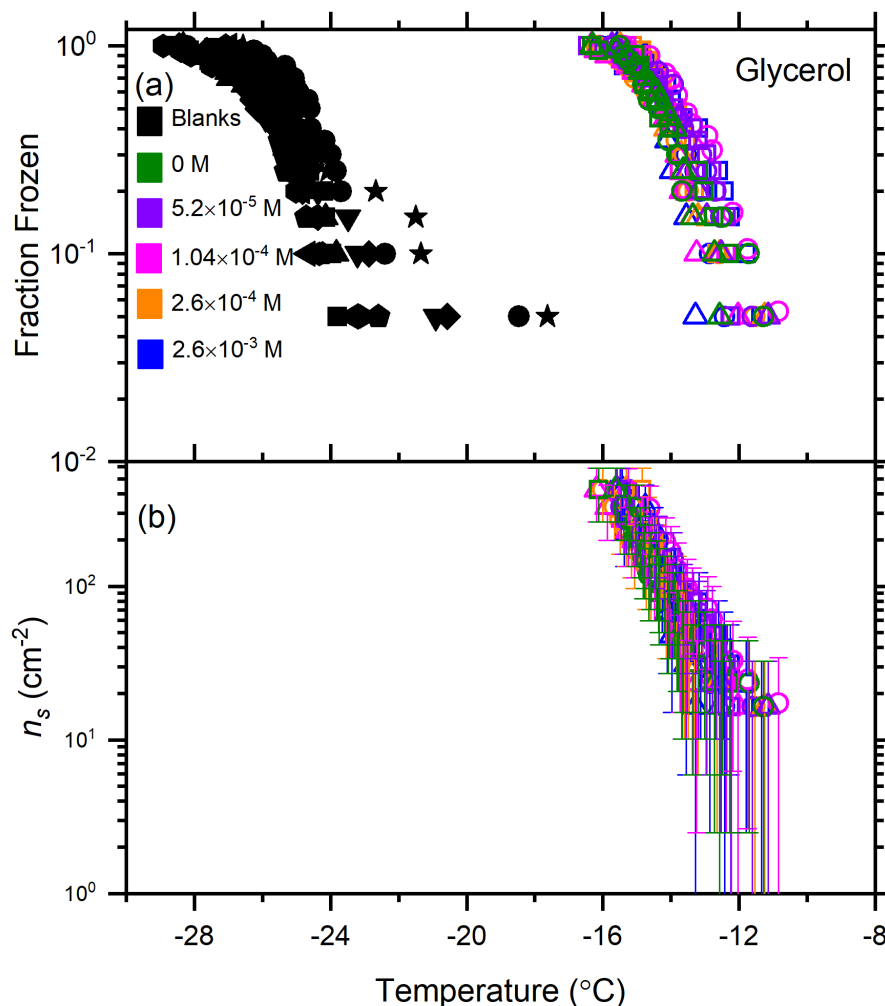


Figure C.1: Freezing data for the effect of glycerol on the ice nucleating ability of K-rich feldspar. (a) The fraction frozen of droplets containing K-rich feldspar as a function of glycerol concentration (0 M, olive; 5.2×10^{-5} M, violet; 1.04×10^{-4} M, magenta; 2.6×10^{-4} M, orange; 2.6×10^{-3} M, blue). Also included are the fraction frozen of pure water droplets (i.e., blanks) from multiple trials. Different symbols with the same color correspond to different trials. (b) Ice nucleating active site density (n_s) as a function of temperature calculated with the freezing data from panel (a). The error bars for n_s correspond to the 95% confidence intervals calculated with the nucleation statistics from Koop et al. (1997).

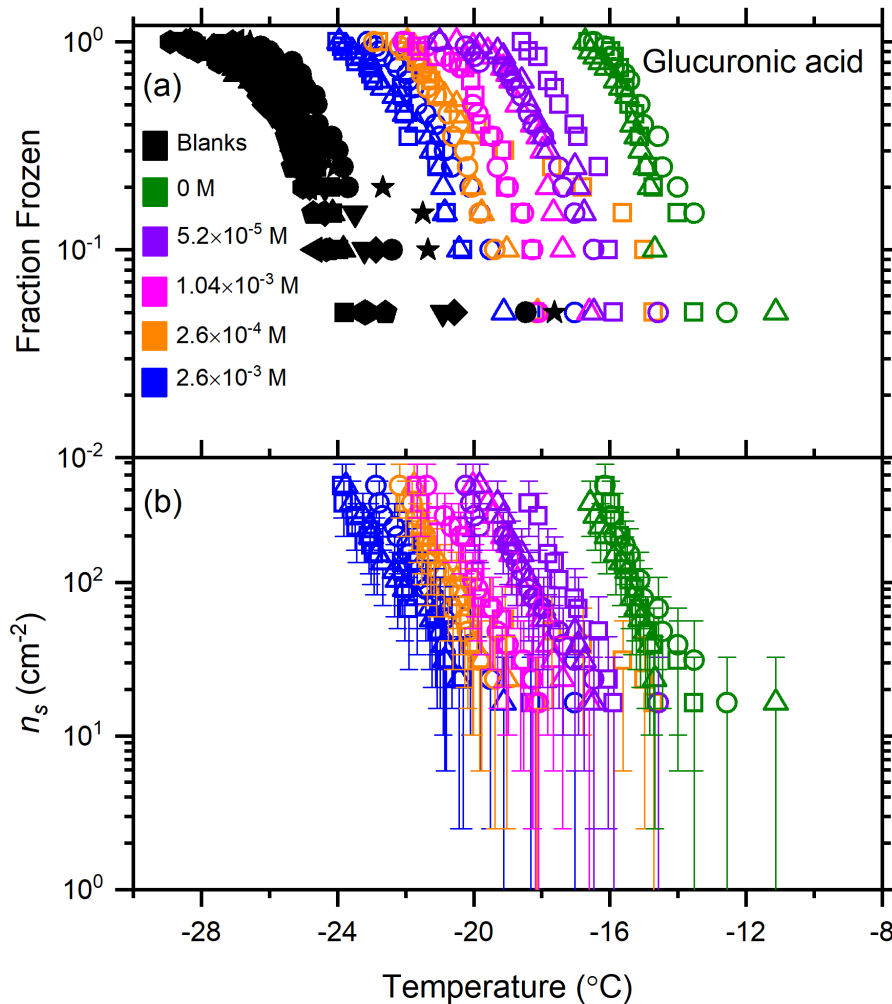


Figure C.2: Freezing data for the effect of glucuronic acid on the ice nucleating ability of K-rich feldspar. (a) The fraction frozen of droplets containing K-rich feldspar as a function of glucuronic acid concentration (0 M, olive; 5.2×10^{-5} M, violet; 1.04×10^{-3} M, magenta; 2.6×10^{-4} M, orange; 2.6×10^{-3} M, blue). Also included are the fraction frozen of pure water droplets (i.e., blanks) from multiple trials. Different symbols with the same color correspond to different trials. (b) Ice nucleating active site density (n_s) as a function of temperature calculated with the freezing data from panel (a). The error bars for n_s correspond to the 95% confidence intervals calculated with the nucleation statistics from Koop et al. (1997).

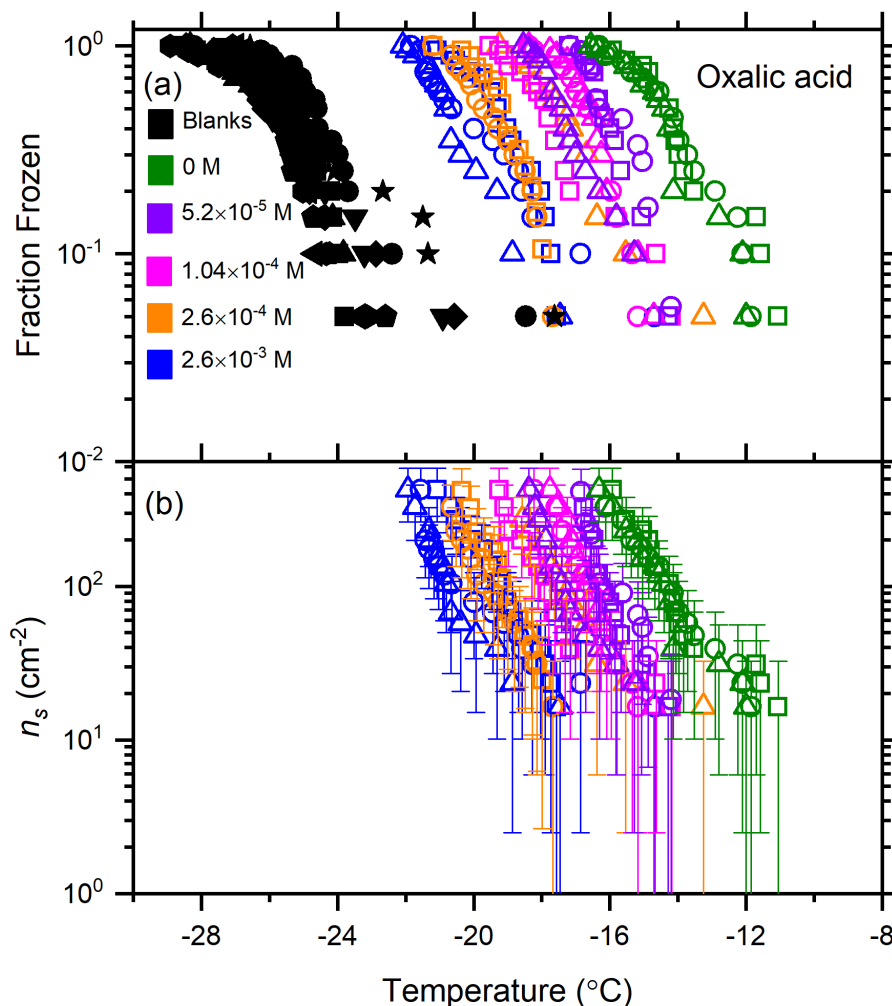


Figure C.3: Freezing data for the effect of oxalic acid on the ice nucleating ability of K-rich feldspar. (a) The fraction frozen of droplets containing K-rich feldspar as a function of oxalic acid concentration (0 M, olive; 5.2×10^{-5} M, violet; 1.04×10^{-4} M, magenta; 2.6×10^{-4} M, orange; 2.6×10^{-3} M, blue). Also included are the fraction frozen of pure water droplets (i.e., blanks) from multiple trials. Different symbols with the same color correspond to different trials. (b) Ice nucleating active site density (n_s) as a function of temperature calculated with the freezing data from panel (a). The error bars for n_s correspond to the 95% confidence intervals calculated with the nucleation statistics from Koop et al. (1997).

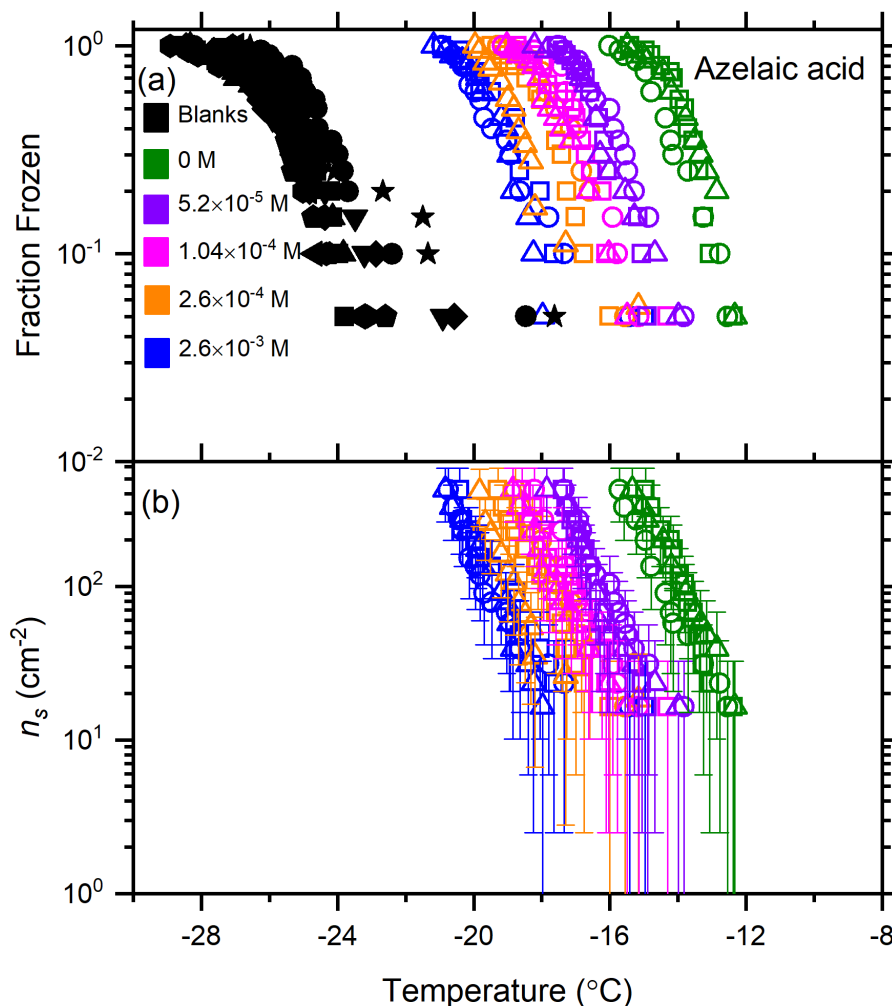


Figure C.4: Freezing data for the effect of azelaic acid on the ice nucleating ability of K-rich feldspar. (a) The fraction frozen of droplets containing K-rich feldspar as a function of azelaic acid concentration (0 M, olive; 5.2×10^{-5} M, violet; 1.04×10^{-4} M, magenta; 2.6×10^{-4} M, orange; 2.6×10^{-3} M, blue). Also included are the fraction frozen of pure water droplets (i.e., blanks) from multiple trials. Different symbols with the same color correspond to different trials. (b) Ice nucleating active site density (n_s) as a function of temperature calculated with the freezing data from panel (a). The error bars for n_s correspond to the 95% confidence intervals calculated with the nucleation statistics from Koop et al. (1997).

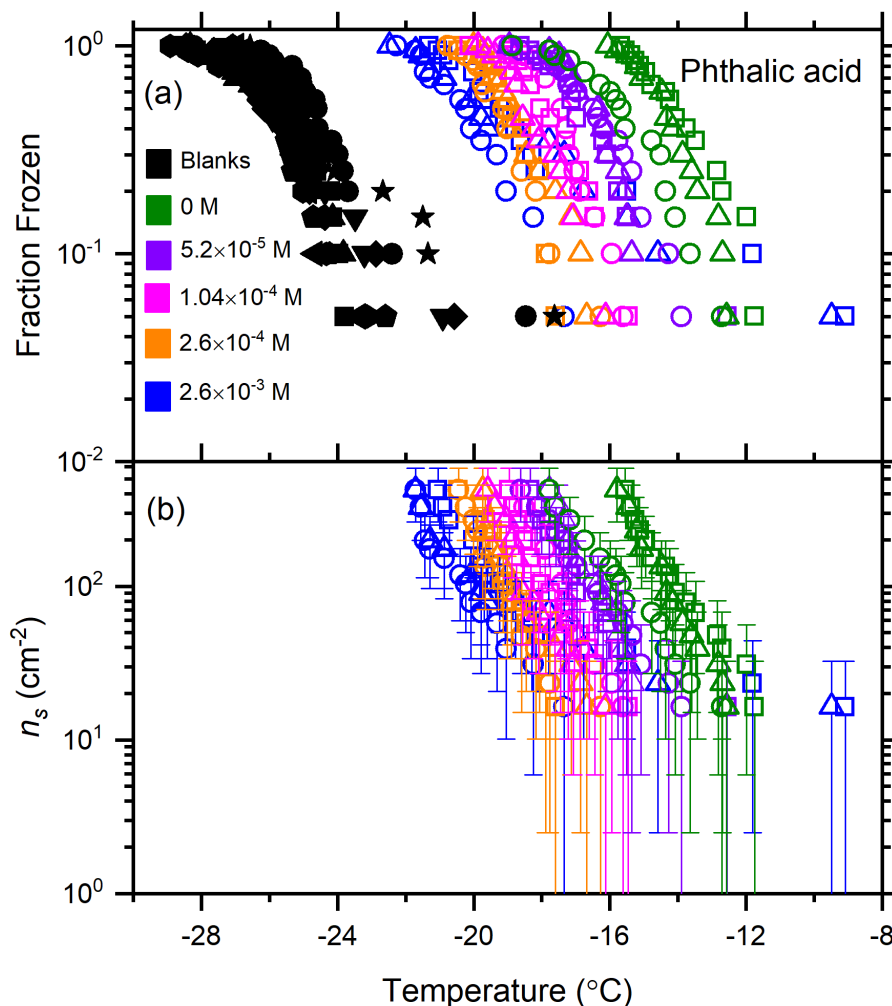


Figure C.5: Freezing data for the effect of phthalic acid on the ice nucleating ability of K-rich feldspar. (a) The fraction frozen of droplets containing K-rich feldspar as a function of phthalic acid concentration (0 M, olive; 5.2×10^{-5} M, violet; 1.04×10^{-4} M, magenta; 2.6×10^{-4} M, orange; 2.6×10^{-3} M, blue). Also included are the fraction frozen of pure water droplets (i.e., blanks) from multiple trials. Different symbols with the same color correspond to different trials. (b) Ice nucleating active site density (n_s) as a function of temperature calculated with the freezing data from panel (a). The error bars for n_s correspond to the 95% confidence intervals calculated with the nucleation statistics from Koop et al. (1997).

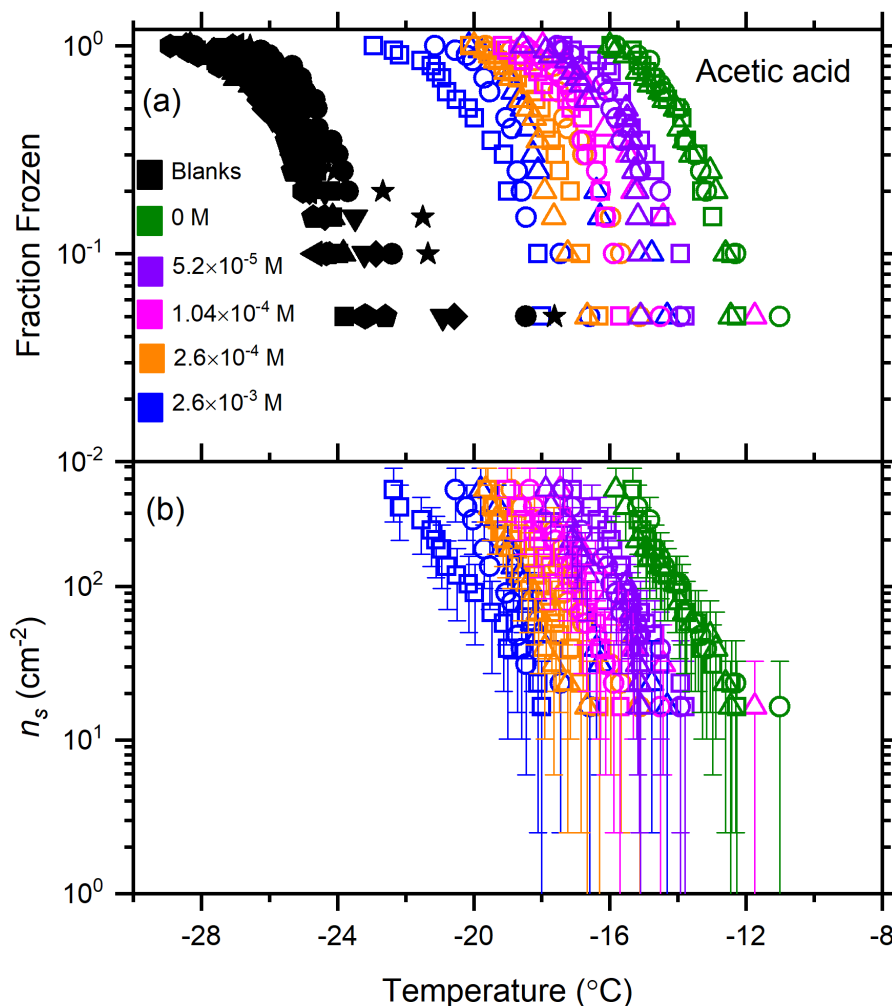


Figure C.6: Freezing data for the effect of acetic acid on the ice nucleating ability of K-rich feldspar. (a) The fraction frozen of droplets containing K-rich feldspar as a function of acetic acid concentration (0 M, olive; 5.2×10^{-5} M, violet; 1.04×10^{-4} M, magenta; 2.6×10^{-4} M, orange; 2.6×10^{-3} M, blue). Also included are the fraction frozen of pure water droplets (i.e., blanks) from multiple trials. Different symbols with the same color correspond to different trials. (b) Ice nucleating active site density (n_s) as a function of temperature calculated with the freezing data from panel (a). The error bars for n_s correspond to the 95% confidence intervals calculated with the nucleation statistics from Koop et al. (1997).

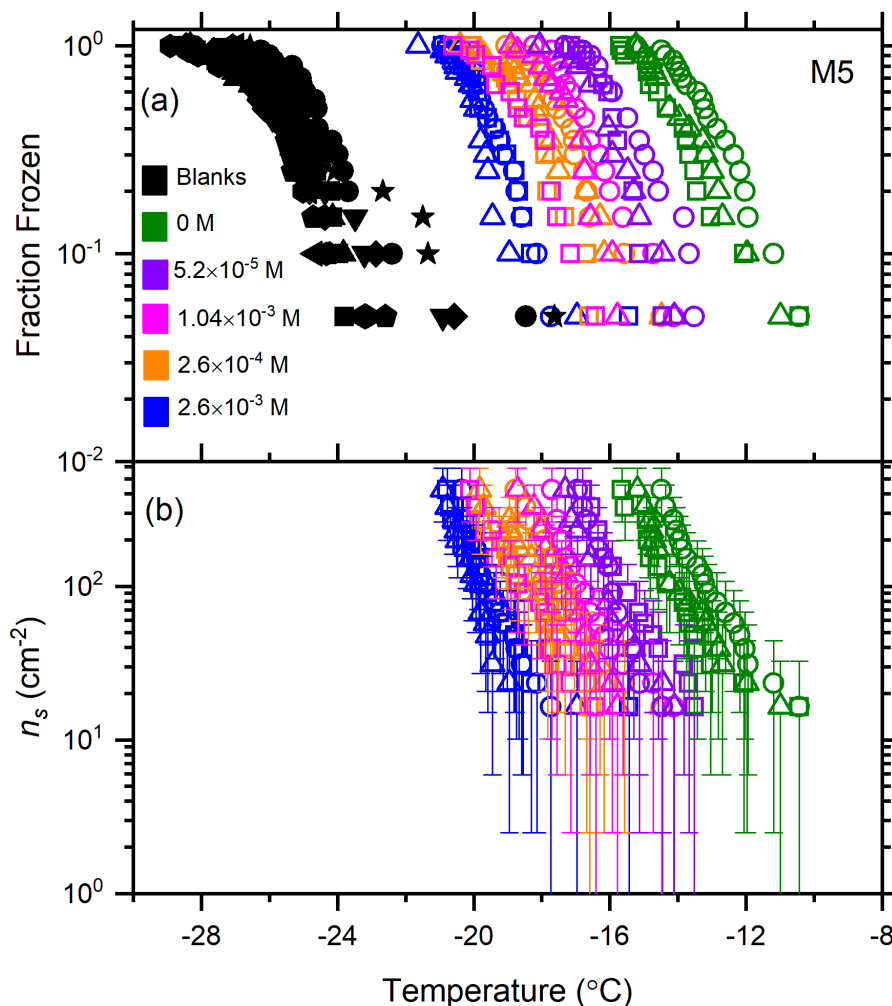


Figure C.7: Freezing data for the effect of M5 on the ice nucleating ability of K-rich feldspar. (a) The fraction frozen of droplets containing K-rich feldspar as a function of M5 concentration (0 M, olive; 5.2×10^{-5} M, violet; 1.04×10^{-3} M, magenta; 2.6×10^{-4} M, orange; 2.6×10^{-3} M, blue). Also included are the fraction frozen of pure water droplets (i.e., blanks) from multiple trials. Different symbols with the same color correspond to different trials. (b) Ice nucleating active site density (n_s) as a function of temperature calculated with the freezing data from panel (a). The error bars for n_s correspond to the 95% confidence intervals calculated with the nucleation statistics from Koop et al. (1997).

Appendix D

Table D.1: Relevant information on the previous measurements of INP concentrations in the Arctic from ground-based or ship-based platforms shown in Fig. 4.4.

Study	Platform	Location	Sampling time
Radke et al. (1976)	Ground	Utqiaġvik, Alaska, USA	March, 1970
Fountain et al. (1985)	Ground	Utqiaġvik, Alaska, USA	August, 1978 – April, 1979
Bigg (1996)	Ship	Arctic Ocean	August – October, 1991
Bigg et al. (2001)	Ship	Arctic Ocean	July – September, 1996
Conen et al. (2016)	Ground	Finnmark, Norway	July, 2015
Mason et al. (2016)	Ground	Alert, Nunavut, Canada	March – July, 2014
Creaman et al. (2018)	Ground	Oliktok Point, Alaska, USA	March – May, 2017
Si et al. (2018)	Ground	Alert, Nunavut, Canada	March, 2016
Irish et al. (2019)	Ship	Arctic Ocean	July – August, 2014
Santl-Temkiv et al. (2019)	Ground	Villum, Greenland	August, 2016
Wex et al. (2019)	Ground	Alert, Nunavut, Canada	April, 2015 – April, 2016
Wex et al. (2019)	Ground	Utqiaġvik, Alaska, USA	June, 2012 – June, 2013
Wex et al. (2019)	Ground	Villum, Greenland	January, 2015 – November, 2015
Wex et al. (2019)	Ground	Ny-Ålesund, Norway	March, 2012, - September, 2012
Creamean et al. (2019)	Ship	Bering Strait, Arctic Ocean	August – September, 2017
Welti et al. (2020)	Ship	Arctic Ocean	July – August, 2001
Hartmann, Gong, et al. (2020)	Ship	Arctic Ocean	May – July, 2017

Table D.2: The residence time that each air mass spent in the 7 days prior to sampling in the footprint layer over a specific surface type (land, sea ice, sea, and snow) for each sample.

Collection date of the samples	Residence over land (s)	Residence over sea ice (s)	Residence over Sea (s)	Snow (s)
October 19 th	513.33	15078.3	7204.04	14894.8
October 20 th	1133.96	46781.1	4055.8	24232.5
October 21 st	154.79	76579.4	5886.24	29009.1
October 22 nd	326.99	40152.7	7783.69	16190.6
October 23 rd	31.59	77622.3	4748.68	8489.87
October 24 th	20.55	24062.2	2390.79	11421.8
October 25 th	65.59	21270.2	3353.69	35879
October 26 th	71.94	36990.9	2438.77	32094.6
October 27 th	16.85	30637.1	600.07	39952.4
October 28 th	3.05	15228.9	385.48	37134.8
October 29 th	726.07	22659	577.20	61923.9
October 30 th	1065.72	27905.5	2208.78	69060.7
October 31 st	645.80	43054.8	6167.5	46937.3
November 1 st	193.51	23231.4	16735.1	20140.4
November 2 nd	374.33	49282.1	12775.7	13058.1
November 3 rd	628.16	16966	12181.8	29180.7
November 4 th	155.14	31995.4	2944.26	19794.5
November 5 th	8.88	73468.8	1865.23	37721
November 6 th	0.0087	120622	27.62	58710.9
November 7 th	0.3243052	94172.4	107.14	28177.2
November 8 th	0.005026	128938	6.39	95118.9
November 9 th	0	154951	1.27	97707.6
November 10 th	5.72×10^{-5}	122226	1.16	145639
November 11 st	7.57×10^{-5}	60350.2	133.21	37868.3
November 12 nd	0.018	75497.6	58.15	10154.7
November 13 rd	8.8×10^{-5}	54308.4	1.73	31823.2
November 14 th	8.7×10^{-5}	19470.1	3.41	58576.7
November 15 th	0.0015	47464.7	11.77	63784.9
November 16 th	0.28	71579.1	10.07	41065.1
November 17 th	4.11	99929.7	247.25	21651